MECHANICS AND DYNAMICS OF LINE BORING OPERATION WITH PROCESS DAMPING EFFECT

by

ADEM AYGÜN

B.Sc. Middle East Technical University, Turkey, 2007

A THESIS SUBMITTED IN PARTIAL FULFILLMENT OF
THE REQUIREMENTS FOR THE DEGREE OF

MASTER OF APPLIED SCIENCE

in

THE FACULTY OF GRADUATE STUDIES
(Mechanical Engineering)

THE UNIVERSITY OF BRITISH COLUMBIA
(Vancouver)

October 2010

Abstract

Rotating shafts are used in the power train components of aircraft and automotive engines. The shafts are turned on the lathes. Engine cylinders and bearing housings are finish machined using boring bars with single or multiple inserts. The cutting forces excite the structural dynamics of the turned shafts or boring bars during machining, leading to a poor surface finish and possible damage to the machined parts. This thesis presents mathematical models of single and multiple point turning/boring operations with the aim of predicting their outcome ahead of costly physical trials on the shop floor.

Turning and boring operations are conducted at low angular speeds where the system dynamics is dominated by the process damping mechanism. The dynamic forces are modeled proportional to the static and regenerative chip thickness, direction of chip flow, tool geometry, and velocities of the vibration and cutting process. The process damping coefficients, which are dependent on the material, tool geometry, cutting speed and vibrations, are identified from chatter tests conducted at the critical speeds and depths. The cutting forces are modeled for boring tools with a single insert, inserts distributed around the circular cross section as well as along the axis of the boring bar. The structural dynamics of the long boring bars are modeled using the Timoshenko Beam elements in a Finite Element model. The structural dynamic model allows parametric placement of the boundary conditions, such as the bearing supports along the boring bar. The dynamics of the interaction between the cutting process and the structure are modeled. The stability of the operations is solved in the frequency domain, analytically when the velocity and vibration dependent process damping is neglected. When the process damping is included, but the periodicity of the dynamic forces is neglected, the stability of the process is solved using the Nyquist criterion. When the periodicity and process damping are considered, the dynamic system is represented by a set of differential equations with periodic, time delayed forces. The stability of such systems, which are found in the line boring of crank and cam shaft housings, is solved in the time domain using an analytical but semi-discrete method.

The thesis presents a complete set of solutions in predicting the static and dynamic forces, as well as the critical depths of cuts and speeds to avoid chatter vibrations in single point, multi-point and line boring operations.

Table of Contents

List of Tables

List of Figures

List of Symbols

Symbols

η	: Chip flow angle
$\bar{\eta}$	: Average chip flow angle
K_{rc}, K_{tc}, K_{ac}	: Radial, tangential and axial cutting force coefficient
K_{re}, K_{te}, K_{ea}	: Radial, tangential and axial edge force coefficient
τ_s	: Shear yield stress
β_n	: Normal friction angle
γ_n	: Normal rake angle
γ_{eff}	: Effective rake angle
λ_s	: Inclination (helix) angle
ϕ_n	: Normal shear angle
α_{eff}	: Effective clearance angle
c	: Feed rate
b	: Width of cut
A	: Chip area
$h,\ h_{cusp}$	: Chip thickness and height of cusp region
r_ε	: Nose radius
κ_r	: Approach angle
w	: Projection of chord length in feed direction
l	: Projection of chord length in width of cut direction
θ	: Chord angle
L	: Approximate chord length
L_w	: Flank wear length
F_x, F_y, F_z	: Forces in x,y and z directions
F_r, F_t, F_a	: Forces in r,t and a directions
$\left\{\mathbf{F}_{xyz}\right\}$	: Matrix form of forces in x-y-z directions

$\{\mathbf{F}_{rta}\}$	: Matrix form of forces in r-t-a directions
x, y, z	: Machine coordinate system
C_i	: Process damping coefficient
V_c	: Cutting surface speed
μ	: Friction coefficient
$\mathbf{T}_1, \mathbf{T}_2, \mathbf{T}_3, \mathbf{T}_4$	: Transformation matrices
$\mathbf{A}_i, \mathbf{A}_{0i}$	: Time variant and averaged directional coefficient matrix for i^{th} bore
$[\mathbf{DCM}]$	: Directional coefficient matrix for whole line boring structure
Λ_R, Λ_I	: Real and imaginary part of eigenvalue
n	: Spindle speed
N, M	: Number of radially and axially spaced inserts
$\mathbf{J}, \mathbf{J}_\tau, \mathbf{J}_v$	: Direct, delayed and process damping gain matrices
$\mathbf{\Phi}$	: Transfer function of whole line boring structure
$\mathbf{U}$	: Mass normalized modal matrix
$\mathbf{p}, \mathbf{q}$	: Displacement vectors in machine and modal coordinates
M, C, K	: Mass, damping and stiffness matrices
L, R, S	: Time dependent state matrices
$\mathbf{N}_{i,1}, \mathbf{N}_{i,2}, \mathbf{N}_{i,3}$	: Coefficients of recursive solution of ODE
$\mathbf{\Theta}_\tau, \tilde{\mathbf{\Theta}}_\tau$	: Complete and reduced transition matrices
FFT	: Fast Fourier Transform
FEM	: Finite Element Method
FRF	: Frequency Response Function
SD	: Semi Discretization
EOM	: Equation of Motion
DDE	: Delayed Differential Equation
ODE	: Ordinary Differential Equation
ZOS	: Zero Order Solution
NSM	: Nyquist Stability Method

Acknowledgements

I would like to thank my supervisor, Prof. Yusuf Altintas, for his guidance, support and patience during my studies at The University of British Columbia.

It was a great privilege for me to become a member of Manufacturing Automation Laboratory (MAL). The theoretical and experimental discussions that I had with my exceptional colleagues contributed a lot to my studies. The multicultural environment at MAL was a great opportunity for me to build strong friendships and I enjoyed every moment that I spent with my friends at MAL. I would also like to thank my friend Mark Haring from The Netherlands for his assistance during the time we worked together.

Finally, many thanks to my dear mother Leyla, my father Ilhan and my brother Gurcan for their support and patience during my stay in Canada.

Chapter 1

Introduction

The machining operations such as turning, boring and milling are commonly used in the industry. The wide range of applications consists of automotive engine parts such as the engine block and aircraft components such as the engine turbine, as well as biomedical parts. The limitations affecting the quality of the part and cost of the production originate from the thermo-mechanical properties of work material, torque and power capacity of the machine tool and vibrations due to flexible tool-workpiece interaction. Relative motion between tool and workpiece results in excessive vibrations called chatter which scraps the workpiece unless avoided. Knowing the limitations that are inherent in the workpiece and machine tool, a process planner can optimize the process by considering the dynamics and mechanics of the cutting operation and eventually maximize the material removal rate.

Dynamic cutting operations are usually represented by delayed differential equations where the delay component arises from the previous passage of the tool which contributes to the vibrations and forces being generated at the current state. It also includes the material properties, structural dynamics of the flexible components, and the process specific cutting model which may also bring in time dependency to the system. Under some operating conditions, the damping capacity of the structure is insufficient to damp out the energy generated at the tool-workpiece engagement and, consequently, vibrations increase drastically. This creates an instability problem and the prediction of critically stable cutting conditions is of the utmost importance and studied by many researchers in the past.

The characteristics of high speed machining is very well studied and analyzed by researchers. However the classical stability prediction methods underestimate the experimentally obtained critical stability border at low speeds. This is attributed to the process induced damping term which is inversely proportional to the cutting speed and dominates the dynamic system at low cutting speeds. Significant research efforts have been spent in modeling the process damping effect. Earlier attempts include defining the complex cutting coefficients, the interaction between tool flank face and finished surface, and the interaction between tool rake face and chip. In all of the previous studies, material dependency is introduced to the model with the process damping coefficient which must be identified for each material or extracted from other material properties like Young's modulus. Basically, three different identification methods appear in literature thus far: oscillation tests, indentation tests, and extraction from chatter tests. In this thesis, a simple identification method for the process damping coefficient is presented.

In an automotive engine, the rotating parts are connected to the stationary body through holes. As the crankshaft and camshaft are very long components, there are several bores on the engine block and cylinder head, respectively, to provide a smooth connection. A special line boring machine is used in order to machine the crankshaft and camshaft bores. The tool has a long bar on which there are as many axially spaced inserts as the number of bores to be machined. All of the bores are machined simultaneously with this tool. The slender structure of the bar brings low dynamic stiffness and makes the process prone to excessive vibrations. Various supporting methods are used to increase the dynamic stiffness of the bar. In this thesis, a generalized dynamic line boring model to predict the stability, vibrations, and forces is presented considering various support conditions.

The thesis is organized as follows: In Chapter 2, a review of the existing research on the dynamics of single point cutting, the modeling of process damping and mechanics, and the dynamics of line boring process is presented. Several process damping identification methods are discussed in detail.

Chapter 3 is dedicated to the identification technique for the process damping coefficient. An approximate chip model is used which can accommodate the influence of the operating conditions and tool geometry. The regeneration of the chip is assumed to be in chip flow direction which is a function of feedrate, width of cut, nose radius and approach angle. Identification is based on chatter tests where transition from an unstable state to a stable state is captured, and the critical velocity is recorded. The characteristic equation of dynamic plunge turning is used to estimate the unknown damping coefficients. Stability prediction is carried out by using Nyquist stability criterion in frequency domain. Finally, experiments are conducted for verification purposes.

In Chapter 4, the stability of the line boring operation is investigated including the process damping effect. Finite element beam theories are applied to represent the line boring structure and to estimate the transfer function between tool and workpiece. Zero order solution and Nyquist stability criterion are proposed for stability solution in frequency domain. Semi-discretization is used to investigate the influence of the time varying directional coefficients arising from the rotation of the line boring bar. The vibrations and the dynamic cutting forces are simulated in time domain. A detailed comparison of stability charts under various insert, support and angular orientations is also presented.

The thesis is concluded with a brief summary of contributions and possible future works. The details of some mathematical derivations are given in the Appendices.

Chapter 2

Literature Review

2.1 Overview

Single point cutting operations, such as turning and boring, are widely used in manufacturing. Investigation of the mechanics and dynamics of those processes are important in terms of productivity and quality of the final product. However, a comprehensive model requires the modeling of nonlinearities that stem from the geometry and the force coefficients. Research related to the modeling of single point cutting operations is surveyed in section 2.2.

The aim of manufacturing is to maximize the productivity of machining operations while keeping the surface quality within specified tolerances. However, the maximum surface speed is limited for some materials such as titanium and nickel alloys. The dynamics of the cutting process is mainly dominated by the *process damping* at low speed, which is surveyed and discussed in section 2.3.

A special purpose operation called *line boring* is of interest in this thesis. It is mainly used to machine axially spaced crankshaft or camshaft bores of engine blocks. As it has many inserts along the bar cutting at the same time, the dynamic analysis is different from many machining operations, and related research is discussed in section 2.4.

2.2 Dynamics of Single Point Cutting

Turning and boring are the most common single point cutting operations used in the industry. Turning is used to remove the material from the outer surface of an axisymmetric workpiece. In general, the rotating workpiece is clamped on the spindle chuck, whereas the tool is stationary. Boring is used to enlarge the existing holes. Similar to turning, the workpiece is rotationary and the boring bar is attached to the tailstock of the lathe. The static forces generated are time invariant in both of the processes because the cutting edge of the tool is fixed. Moreover, static forces are identical when the same cutting conditions are applied in both processes. However, if the dynamic properties are compared, they are dissimilar due to different flexibilities of the structures.

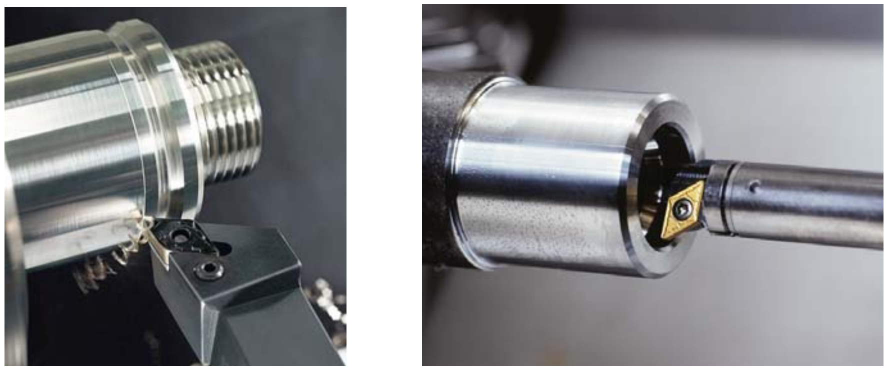

(a) **(b)**

Figure 2-1 : Single point cutting processes (a) Turning (b) Boring

The dynamics of turning have been studied widely in the literature where the biggest problem mentioned is the regenerative chatter vibrations. The chatter vibrations occur due to the phase shift between successive vibration waves when the structural modes of the system are excited, see Figure 2-2a. In literature, the regeneration of the chip thickness phenomenon first appeared in the 1950s in Tobias's [1] and Tlusty's [2] research. Tlusty calculated the absolute limit for the depth of cut by considering the flexibilities of the structure as:

$$a_{\text{lim}} = \frac{-1}{2K_f \min\left(\text{Re}\left(\Phi(j\omega)\right)\right)} \tag{2.1}$$

where K_f is the assumed constant cutting force coefficient and $\Phi(j\omega)$ is the frequency response function between the tool and workpiece which relates displacement to cutting forces. Tobias invented the stability lobes where higher stable depth values than the one calculated by Eq.(2.1) can be selected at various spindle speed ranges, see Figure 2-2b. Merritt [3] explained the chatter phenomenon as a closed loop system where the vibrations during the previous cut are fed back and cause instability of the system.

More complex tools are used in today's machining centers which consider geometric nonlinearities to the cutting model. One of the most important parameters is the nose radius of the tool which has significant effect on the cutting force directions. Ozdoganlar et al. [4] developed a chip area formulation which can be used with nose-radiused tools under depth and feed direction variations. He compared the error of the method with the exact area calculation with many conditions, and concluded that the error is negligible for practical purposes. In [5], Ozdoganlar et al. presented an analytical chatter stability solution for turning operations which considers the linearized uncut chip area formulations. With this method, the model is capable of accommodating the effect of the cutting conditions (feedrate, depth of cut) and tool geometry (nose radius, approach angle). Reddy et al. [6] applied a similar approach to solve the stability problem of contour turning where the effect of the tool path on stability is observed. Thus, they were able to investigate the stability of more complex part geometries by means of the developed contour turning stability prediction method.

(a)

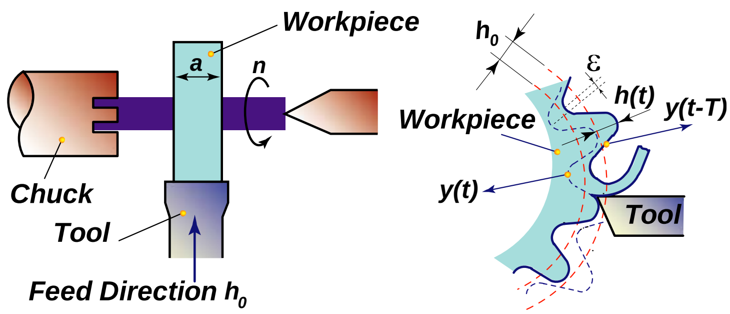

(b)

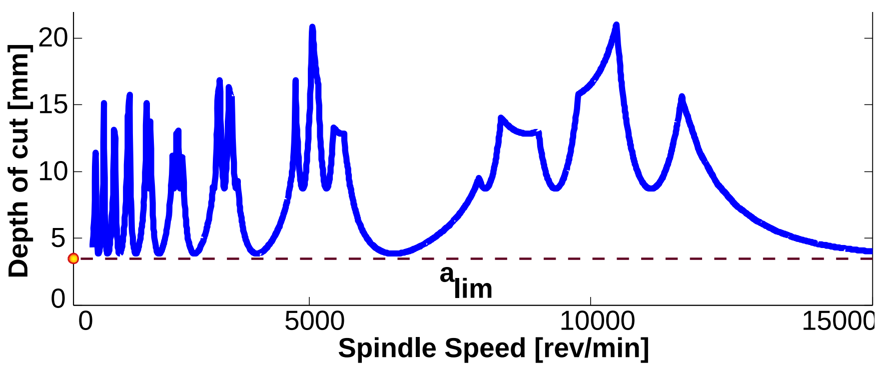

Figure 2-2 : (a) Regeneration of chip thickness in plunge turning operation [7] (b) Stability diagram example

Clancy and Shin [8] proposed a stability method for the face turning operation. In their model, flexibilities in three orthogonal directions and the effect of flank wear on stability are considered. Stability is investigated in frequency domain by solving the eigenvalues of the force model. However, an iterative approach is used because many variables in the force model are dependent on the depth of cut value which is not known initially. Given an initial depth value, the iteration continues until convergence of the depth of cut to some predefined tolerance is reached.

In 2007, Ozlu et al. [9] proposed an analytical model for the stability of turning and boring processes which includes true insert geometry and flexibilities in feed and depth directions. In their study, the major cutting edge is divided into small elements, and the cutting force directions are estimated separately for each element, see Figure 2-3. Stability is solved in frequency domain with the eigenvalue solution method reported by Budak [10].

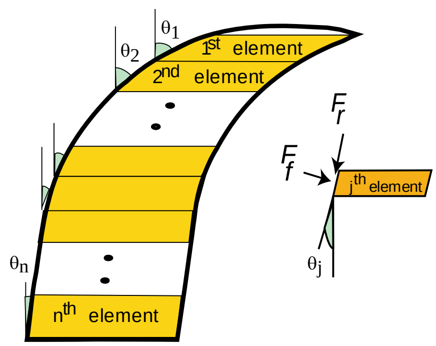

Figure 2-3 : Discretization of chip area [9]

Recently, Eynian et al. [11] proposed a stability method for general turning operations. The process is modeled as it happens along the equivalent chord length connecting the two extreme points of the cutting edge. The penetration of the tool flank face is included as a source of process damping. The stability is checked by using the Nyquist stability criterion at each cutting condition where speed dependent cutting coefficients are utilized. Sensitivity analysis of tool geometry and operating conditions revealed that they have a significant effect on chatter stability predictions.

In literature, there are a handful of studies related to the boring operation as opposed to the turning operation. In those studies, the boring bar is considered the dominant source of flexibility due to its slender structure.

Baker et al. [12] in 2002 studied the stability of boring bars with a focus on tangential cutting forces. Based on Parker's study [13], they focused on the design of the boring bar, especially the effect of asymmetry of the boring bar due to the flattened surfaces to the process dynamics. The Nyquist stability criterion is applied to find the stable cutting conditions. Iyer [14] studied the stability of the boring operation at mid-range spindle speeds for single and twin insert tools. In his model, transverse vibrations which are the most critical for boring dynamics are neglected, and only axial vibrations are considered as the reason for chatter. Stability is solved in frequency domain with a similar approach reported by Budak [10]. Although it was mentioned that the nose radius has big effect when the depth of cut value is comparable, this was also neglected in his study. Friction forces mainly occurring at low speed are not included because the interested speed range was higher than 3000 rpm.

Atabey et al. [15] developed a comprehensive cutting force model for boring operations. The insert-workpiece engagement area is calculated for various depth, nose radius, side and end cutting edge angle cases by dividing the area into 3 main regions. The cutting coefficients are identified as a function of cutting speed and feed rate. The predicted forces are within a 10 % error range which is stated to be tolerable. Later, they used this force model for dynamic analysis of boring in time domain [16]. True engagement of the tool-workpiece is considered and regenerative vibration frequencies were predicted successfully for the given operating conditions only. Their model also predicts the machined workpiece topography.

Recently, Yussefian et al. [17] proposed a cutting force model for boring. Similar to Atabey's study, the cutting forces are proportional to the chip area and cutting edge length, but they suggested using B-spline parametric curves to calculate them for every tool geometry and process parameter. This is the main contribution of their study in literature because with one single approach, they eliminated the area calculation by dividing it into many regions. Later, they extended their study to simulate the dynamics of the boring process in time domain [18]. The boring bar was modeled by the Euler-Bernoulli beam theory. Since this theory does not account for the rotary inertia and shear deformation and assumes a rigid clamping condition, it overestimates the first natural frequency. They compensated for this by correlating the theoretical natural frequency with the measured first resonance frequency.

2.3 Process Damping in Continuous Cutting

At low cutting speeds, high stable depth of cut values can be reached in most of the machining operations. In literature, this is explained with an additional damping term which stems from tool flank – workpiece interaction [19], [20], see Figure 2-4a. In the past, a large number of attempts were performed to model the process damping so that stability diagrams could be predicted accurately.

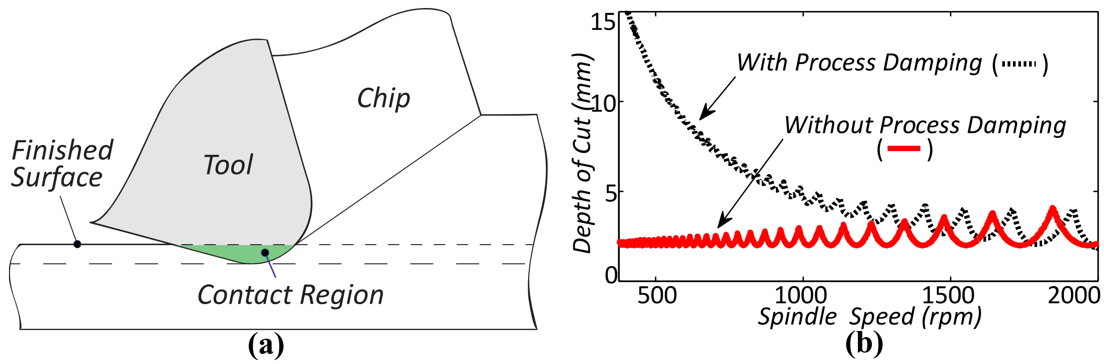

Figure 2-4 : (a) Schematic diagram of the displaced volume underneath the tool (b) Sample stability diagram with and without process damping effect. Increased stability at low speeds due to damping.

Tobias [21] used complex material coefficients in order to introduce the process damping effect into the cutting force model, which also helped others to understand the phase shift between the cutting force and the chip thickness variation. Wu et al. [22], [23] showed that low speed stability is dominated by the ploughing forces on the tool nose region, as opposed to the high speed stability where forces on the rake face are much more effective. Later, Wu [24] presented the ploughing forces to be comprised of two components. The first one is in the chip thickness direction and is proportional to the volume of the material displaced underneath the tool nose region. The second component is generated due to the friction force that the first component causes as:

$$\begin{aligned} f_1 &= f_{sp} V \\ f_2 &= \mu f_1 \end{aligned} \tag{2.2}$$

where V is the volume of displaced material, f_{sp} is the material dependent coefficient and μ is the friction coefficient. Lee et al. [25] simulated the process damping force in time domain using Wu's approach for turning operations.

Chiou and Liang [26] extended Wu's approach and proposed a formula for the volume of displaced volume, making a small amplitude vibration assumption as:

$$V = \frac{-b \cdot l_w^2 \cdot \dot{x}}{2v} \tag{2.3}$$

where b is the depth of cut, v is the surface speed, l_w is the flank wear length and $\dot{x}$ is the velocity of vibrations in the chip thickness direction. Furthermore, the material dependent force coefficient is calculated by a series of static indentation tests. This model was useful in explaining the increased stability when tool wear exists, as observed in the experiments [27]. This model is utilized by several researchers to predict the stability of the turning operation [8], [11] with various flank wear cases.

The identification of the material dependent coefficient in Chiou's study was not satisfactory because it was identified under static conditions. Altintas et al. [27] tried to identify the process damping coefficient under dynamic conditions. They used a piezo-actuator driven fast tool servo for this purpose. This device was able to give displacement to the tool at a specified amplitude and frequency. Thus, the regenerative vibrations are eliminated by keeping the zero phase shift between successive revolutions of the workpiece and only the ploughing forces (process damping force in this case) are measured. Recently, Ahmadi et al. [28] compared both of the methods and concluded by experiments that Chiou's model based on small amplitude vibration underestimates the experimentally determined stability limits and the accuracy of Altintas's identification method depends on the amplitude of excitation in relationship to the feedrate employed in verification tests.

Recently, Budak et al. [29], [30] proposed a new identification method for process damping coefficients where the coefficient is identified directly from chatter tests. In order to obtain a general model, an energy analysis is used in contact force modeling. The effect of the clearance angle and the edge radius (i.e. hone radius) is observed with this method. They stated that as the edge radius gets larger, the effect of process damping can be observed at higher speeds as well. Both Budak and Ahmadi observed that at low speeds, when the depth of cut is increased gradually, the transition region from the stable to unstable region gets larger due to the process damping effect as opposed to the fast transition in the high speed region.

A different process damping idea was presented by Khasawneh et al. [31]. In this approach, the distributed forces acting on the chip-tool interface is considered a short delay regenerative effect which stabilizes the system at low cutting speeds. Although the study was not supported by any experiments, the simulation results show an increased stable region at low speeds. This method highly depends on the force distribution function which is not clearly known (some assumed functions are employed in their study) and the time during which the chip travels on the rake face of the tool. As they suggested, distributed forces can also be used for the flank/workpiece interface. Later, Bachrathy et al. [32] applied this approach to the tool flank/workpiece interface where flank wear exists, and solved the stability using The Semi-Discretization method [33]. In this study, it was shown that if the flank wear is relatively small, the short delay representation can be reduced to the displaced volume of material approximation that Chiou suggested [26]. However, this study is not supported by experiments. Taylor et al. [34] carried out experiments considering both the tool flank/workpiece and chip/tool interactions. They stated that the flank interface stabilizes the cutting process only if the vibration amplitude is high enough. Regardless of the shape of the distributed force, a short regenerative effect on the chip/tool interface was found to be insufficient to match the experimentally obtained stability boundary.

2.4 Mechanics and Dynamics of Line Boring Operation

In literature, the dynamics of a conventional line boring process, shown in Figure 2-5, has never been addressed. There are a few publications, but none of which present a comprehensive model that can be applied to all of the line boring tools. The unique property of the line boring process is that there are multiple inserts located along a very long bar where the structural dynamic characteristics can be quite different. However, since the inserts are located on the same tool, cutting forces at one point might cause vibrations at another cutter location, see Figure 2-5. Unlike the classical chatter theories where the relative transfer function is measured at one point, in the case of line boring, the cross talk between each node becomes very important.

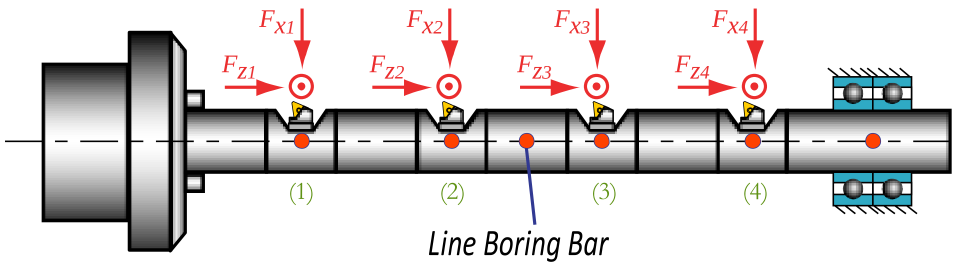

Figure 2-5 : Cutting forces acting on conventional line boring bar

Li et al. [35] proposed a lumped parameter process model in rotating coordinates for rotating boring tools. In their study, the boring bar is assumed to have only one insert at the free end. The guiding pads located at the circumference of the line boring bar are designed in such a way that they support the very long bar by touching the just machined bore. The focus of their study was to see the rotational effects where Coriolis and the centrifugal forces are considered and thus the coupling between radial and tangential dynamics is included which does not exist in the stationary boring bar. They assumed the boring bar as the dominant compliant component which is a reasonable assumption considering the structure of the line boring bar. The nonlinear force model was linearized with respect to the state variables but still, the cutting coefficients were nonlinear functions of the stability limit. In order to solve the stability, an iterative algorithm was adopted in their study. They concluded that averaging the time varying coefficients results in discrepancies at the low speed stability, however, this is not the case for high speed stability which is successfully applied by Altintas and Budak [10].

Some line boring tools have more than one insert at each bore location. Thus, the machining with multiple inserts is of interest in this thesis as well. Atabey et al. [36] studied the mechanics of a multi-insert boring head operation which is commonly used for the machining of engine cylinders. They extended their previous work [15] with single insert boring bars to multiple insert boring heads. The force model includes the effect of tool geometry and process parameters. Furthermore, the process faults such as the misalignment of the boring head axis with respect to the axis of the hole to be machined. This misalignment, as well as radial and axial runouts for each insert, bring about an irregular force profile which was studied extensively in their study. Later Suren [37] studied the dynamics of multiple inserted boring operations. He proposed a stability prediction method in frequency domain using the average directional coefficients without addressing geometric nonlinearities. In case of non-uniform pitch tools, an algorithm to select the optimum pitch angles is presented, which leads to higher stability than uniform pitch angle tools. His study can be used as a starting point for line boring dynamic analysis.

Chapter 3

Identification of Process Damping Coefficient

3.1 Introduction

High material removal rates are mainly prevented by chatter instability in machining. The aim of past and current research has been to foresee under which conditions the cutting operation becomes unstable. High speed operations, specifically, were modeled successfully and experimentally verified [7], which led to improved material removal rates. However, low speed cutting demonstrated different characteristics from high speed cutting which is still not fully understood. At low speeds, higher stable conditions can be observed. Many research studies [20], [21], [38] have explained that an additional process induced damping term, which is inversely proportional to the cutting speed, exists in low speed machining operations. When high speed and low speed cutting are compared in terms of dynamic characteristics, the main difference is the shorter wavelength of vibrations at low speeds. Hence, there are dense vibration marks left on the cut surface at low speeds. These dense vibrations affect the cutting mechanics by changing the rake angle, clearance angle and shear angle. This is illustrated in Figure 3-1.

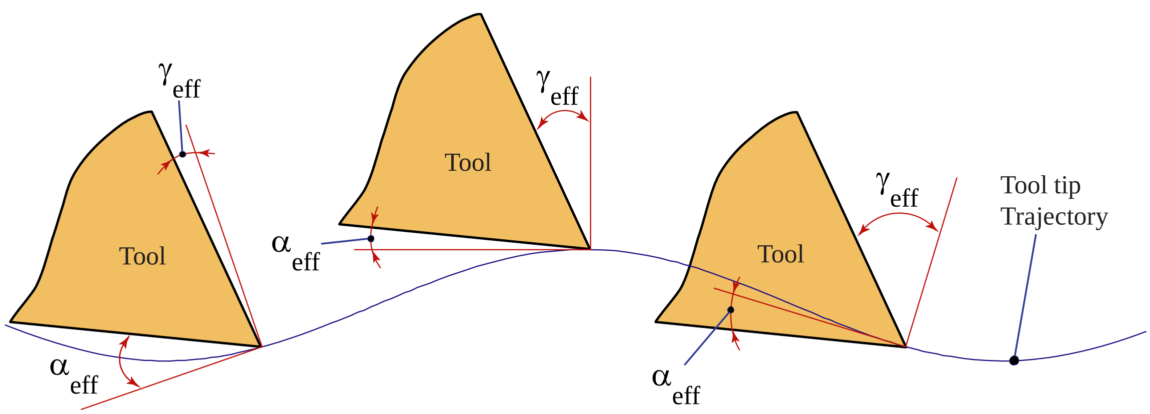

Figure 3-1 : Effective rake and clearance angle change during cutting

Besides dynamically changing geometrical parameters, researchers stated that the clearance face of the tool makes contact with the finished surface of the workpiece, and this brings additional forces to the system as illustrated in Figure 3-2 :

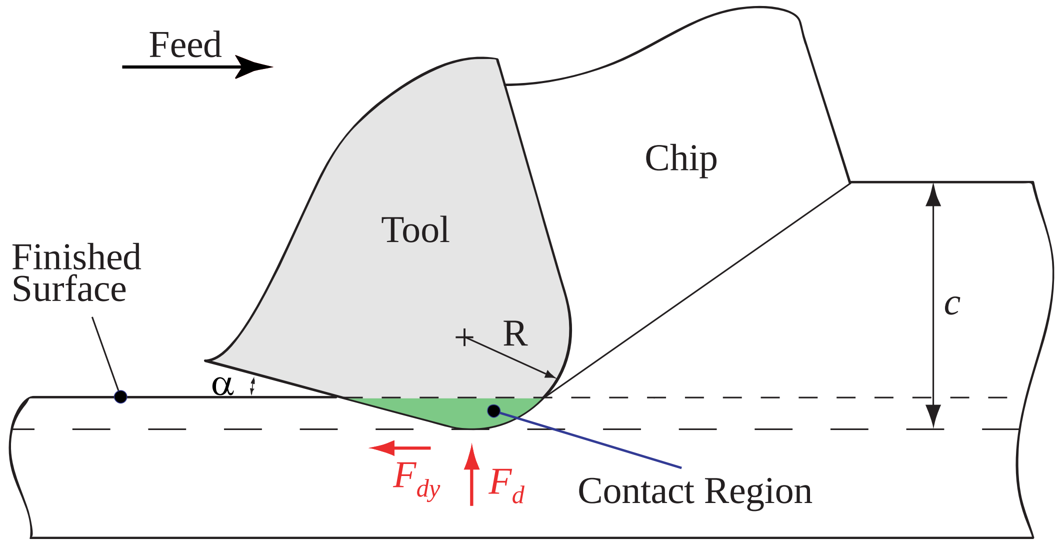

Figure 3-2 : Flank face contact with cut surface and direction of process damping forces

The contact changes dynamically and increases the damping of the system at low speeds. In literature, this phenomenon is named as process damping [39] which is investigated in this chapter.

3.2 Tool Workpiece Interaction

In order to model process damping, researchers focused on the flank face contact. Wallace [40], Wu [24] and later Chiou [26] proposed a method which accounts for the tool-workpiece interaction. Their model assumes that the process damping force is proportional to the volume of material which is displaced underneath the tool. However, this volume of the material changes as the tool and workpiece vibrate simultaneously as seen in Figure 3-3. Following this approach, the indented volume decreases when the tool moves upward; however, it increases when the tool moves toward the workpiece. Therefore, this volume continuously changes and, as a result, the forces change as well.

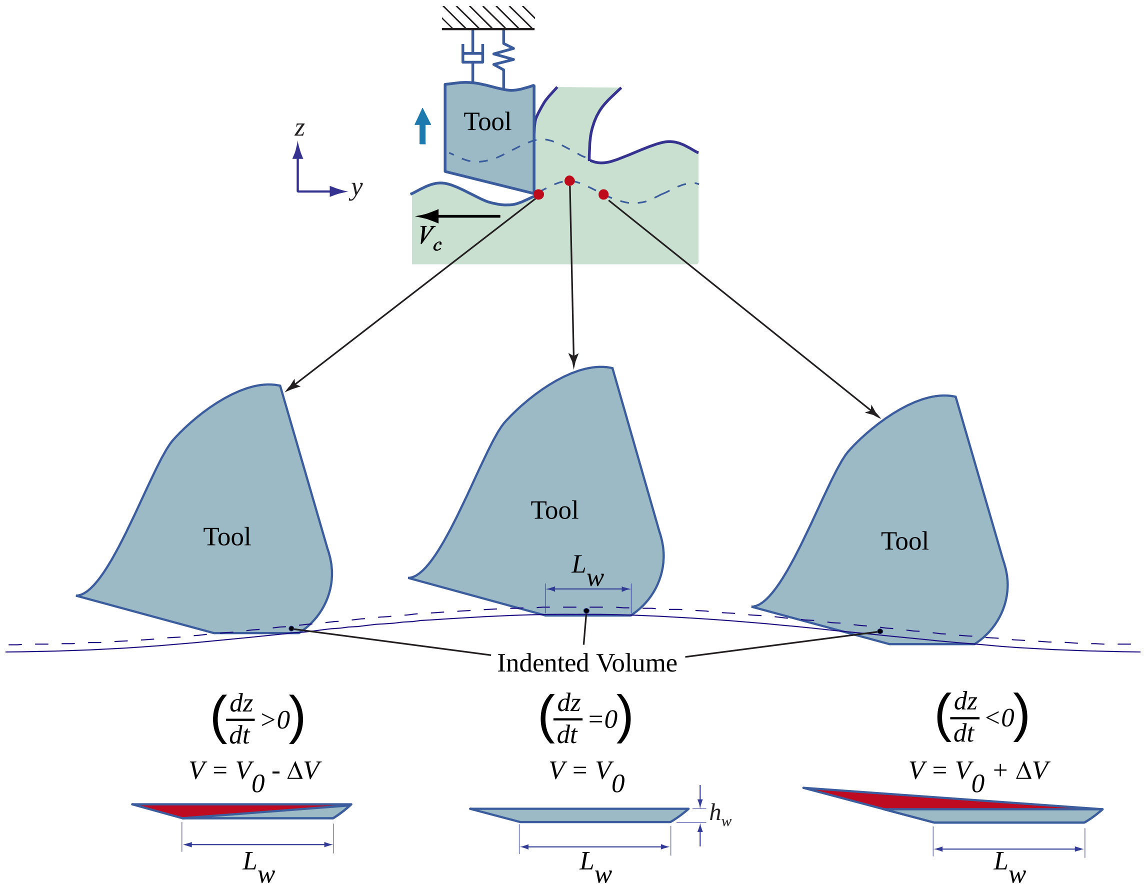

Figure 3-3 : Dynamic variation of indented volume of the tool [40]

In this approach, the penetrated volume of material during stable cutting is constant as:

$$V_0 = L_w h_w \tag{3.1}$$

where L_w is the tool edge wear length and h_w is the height of the material which is deformed under the tool. In the case of vibrations, the volume change is approximated as [26]:

$$\Delta V \cong \begin{cases} -\dfrac{1}{2} b.L_w^2.\dfrac{\dot{z}}{V_c} & \text{if} \quad \dfrac{dz}{dt} < 0 \\ \dfrac{1}{2} b.L_w^2.\dfrac{\dot{z}}{V_c} & \text{if} \quad \dfrac{dz}{dt} > 0 \end{cases} \tag{3.2}$$

where b is the cutting edge length, V_c is the surface speed and $\dot{z}$ is the velocity of the vibrations in the feed direction, see Figure 3-3.

As a result, the total penetrated volume became the same for both the upward ($\dot{z} > 0$) and downward ($\dot{z} < 0$) motion of the tool:

$$V_T = L_w h_w - \frac{1}{2} b L_w^2 \frac{\dot{z}}{V_c} \tag{3.3}$$

The damping force is proportional to the total volume V_T and the process damping coefficient, K_{sp}, which is a material specific property.

$$\begin{aligned} F_d &= K_{sp} V_T \\ &= K_{sp} \left(L_w h_w - \frac{1}{2} b L_w^2 \frac{\dot{z}}{V_c} \right) \\ F_{dy} &= \mu F_d \\ &= \mu K_{sp} \left(L_w h_w - \frac{1}{2} b L_w^2 \frac{\dot{z}}{V_c} \right) \end{aligned} \tag{3.4}$$

The F_d component is pushing the tool out in normal direction to the cut surface. Whereas F_{dy} is the friction component and is perpendicular to F_d, see Figure 3-2 : . In Eq.(3.4), the damping forces consist of a static part and a dynamic part. Since the static part does not contribute to the stability of the cutting operation, it can be disregarded. Thus, the dynamic process damping forces are:

$$\begin{aligned} F_d &= -K_{sp} \frac{1}{2} a L_w^2 \frac{\dot{z}}{V_c} \\ F_{dy} &= -\mu K_{sp} \frac{1}{2} a L_w^2 \frac{\dot{z}}{V_c} \end{aligned} \tag{3.5}$$

The friction coefficient, μ, is a material dependent quantity, but 0.3 is used for a steel workpiece in [24]. The identification of the damping coefficient, K_{sp}, is achieved by a series of indentation tests and by fitting a linear curve between the measured force and the displaced volume [26]. The main idea behind this identification method is that the penetration process during cutting is assumed to be identical to the indentation process with tools in the static case.

An alternate way of expressing the dynamic process damping force is used by Altintas et.al [27]. The damping force is still a function of the vibration velocity and thus changes dynamically during the cutting operation as follows:

$$
\begin{aligned}
F_d &= -C_z a \frac{\dot{z}}{V_c} \\
F_{dy} &= -C_y a \frac{\dot{z}}{V_c}
\end{aligned}
\tag{3.6}
$$

Unlike the previous method [26], the identification of the damping coefficients (C_y, C_z) is achieved by conducting a series of plunge turning tests. In order to eliminate the effect of the regenerative chip thickness, a piezo-actuator driven fast tool servo was used. By moving the tool at a specified frequency and amplitude, the phase difference between the successive revolutions of the workpiece was minimized, and only the process damping effect was measured by a dynamometer. The drawbacks of this method are that first, it requires a specific device designed for this purpose, and second, a series of tests at different excitation frequencies is required. In this thesis, a relatively simple identification method is presented in Section 3.5.

3.3 Prediction of Chip Flow Angle (η)

Single point cutting operations are mostly conducted by using inserted cutters. A summary of insert types along with the applications are presented in Table 3.1. Most of the inserts used in the industry have oblique geometry including the nose radius, r_ε, the cutting edge angle, κ_r, and the inclination angle, λ_s (see Table 3.1). In order to estimate the cutting force directions, several equivalent chip flow models are proposed in literature. Utilizing an equivalent chip model is advantageous in the case of stability analysis because those irregular dimensions bring geometric non-linearity to the mechanics of cutting. A sample chip with the nose radius (r_ε) and the cutting edge angle (κ_r) is introduced in Figure 3-4.

Table 3.1 : Insert Shapes [41]

Insert Type	Geometric Dimensions	3-D View	Application
Triangular	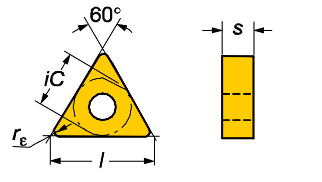	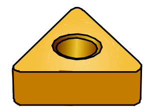	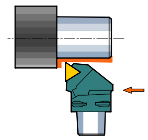
Square	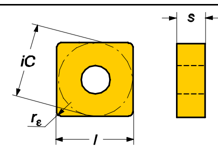	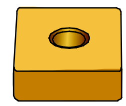	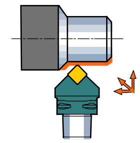
Rhombic (Diamond)	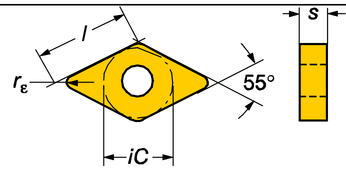	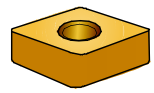	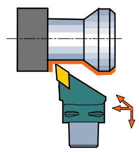
Round	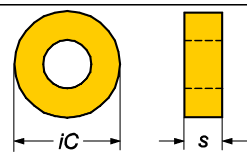	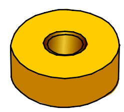	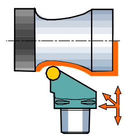
Trigon	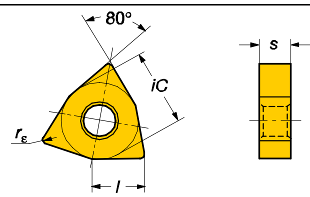	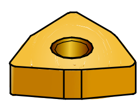	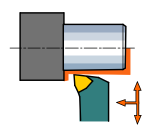

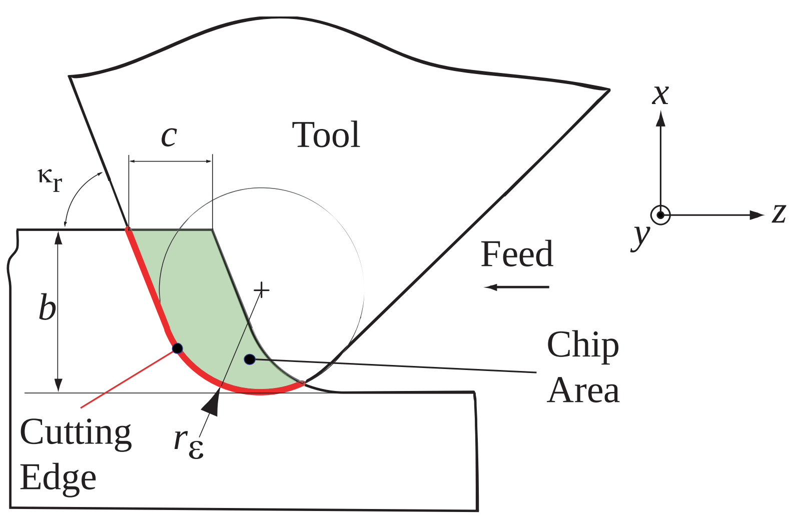

Figure 3-4 : Chip formation with an insert having nose radius, feed rate c, width of cut b.

Stabler [42] proposed that the chip flow angle can be assumed to be the same as the inclination angle of the tool's straight oblique cutting edge. However, this approach is not applicable when the cutting edge is curved, as shown in Figure 3-4. Colwell [43] suggested a geometrical model which simply combines the effect of the nose radius and the cutting edge angle. In his model, a new cutting edge is defined which passes through the two extreme end points of the cutting edge, and the chip flows perpendicular to this equivalent cutting edge. However, obliquity of tool, thus inclination angle and rake angle were not taken into account.

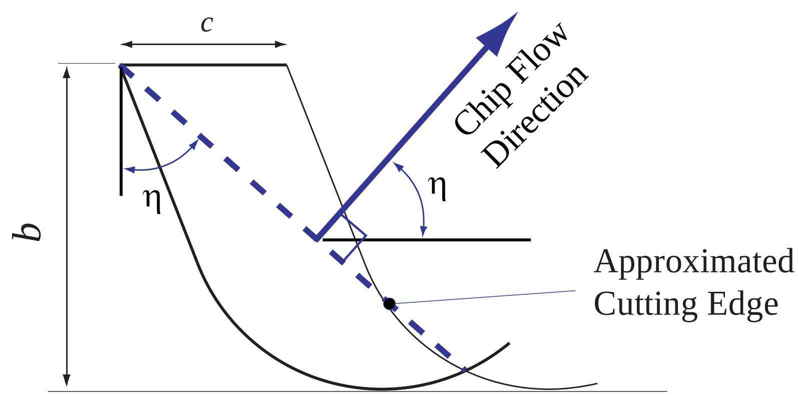

Figure 3-5 : Colwell's approach for chip flow angle estimation

Young et al. [44] proposed a different method for the prediction of the chip flow where the chip is divided into infinitesimal elements, and in each element the chip flow angle is assumed to be in the same direction as the friction force, see Figure 3-6. By summing up the effect of all small area elements in the x and y directions, the average chip flow angle, $\bar{\eta}$, is expressed as:

$$\bar{\eta} = \tan^{-1}\left(\frac{\int \sin(\eta_i)dA}{\int \cos(\eta_i)dA}\right) \tag{3.7}$$

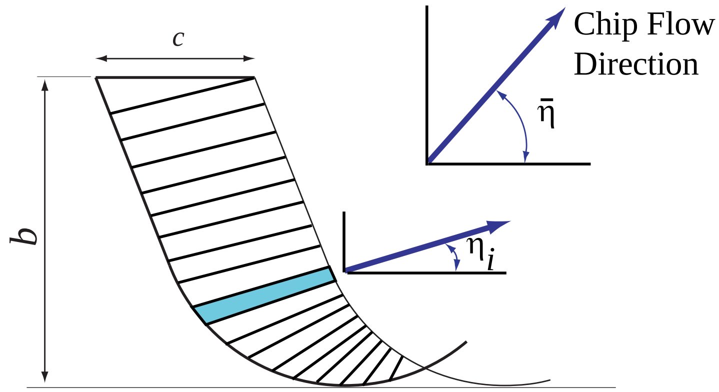

Figure 3-6 : Young's approach for chip flow angle estimation

Wang [45] extended Young's approach by introducing the tool inclination angle and the rake angle of the tool, and derived the necessary formulae for different depth of cut and nose radius combinations.

By implementing the methods summarized above, the chip flow angle for various tool geometries and under different cutting conditions are estimated in this chapter.

3.4 Dynamics of Plunge Turning Operation

Plunge turning is a single point cutting operation. As the cylindrical workpiece rotates, the tool is fed in lateral direction, as given in Figure 3-7. The cutting speed is reduced continuously as the tool is fed into the workpiece which is utilized for process damping identification.

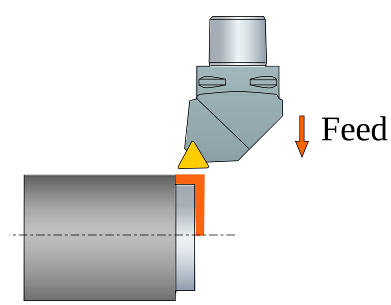

Figure 3-7 : Plunge turning operation

3.4.1 Mechanics of Plunge Turning Operation

The cutting forces in plunge turning can be expressed by adding the contribution of the shearing, ploughing and process damping effects:

$$
\begin{aligned}
F_r &= F_{rc} + F_{re} + F_{pd} = K_{rc}A + K_{re}L - \frac{C_i L}{V_c}\dot{r}(t) \\
F_t &= F_{tc} + F_{te} + F_{pd} = K_{tc}A + K_{te}L - \mu\frac{C_i L}{V_c}\dot{r}(t) \\
F_a &= F_{ac} + F_{ae} \qquad\quad = K_{ac}A + K_{ae}L
\end{aligned}
\tag{3.8}
$$

where r, t and a denote the radial, tangential and axial directions, respectively. The chip area and the length of the cutting edge are denoted by A and L respectively, as shown in Figure 3-8. The cutting forces are written in matrix form as:

$$
\mathbf{F_{rta}} = \mathbf{K_c} \cdot A + \mathbf{K_e} \cdot L - \mathbf{P_d} \cdot \frac{C_i L}{V_c}\dot{r}(t) \tag{3.9}
$$

where $\mathbf{F_{rta}} = \begin{Bmatrix} F_r \\ F_t \\ F_a \end{Bmatrix}$, $\mathbf{K_c} = \begin{Bmatrix} K_{rc} \\ K_{tc} \\ K_{ac} \end{Bmatrix}$, $\mathbf{K_e} = \begin{Bmatrix} K_{re} \\ K_{te} \\ K_{ae} \end{Bmatrix}$, $\mathbf{P_d} = \begin{Bmatrix} 1 \\ \mu \\ 0 \end{Bmatrix}$

The cutting coefficients ($K_{rc}, K_{tc,} K_{ac}$) and the edge coefficients ($K_{re}, K_{te,} K_{ae}$) can be evaluated from an orthogonal cutting database by employing the oblique transformation method explained by Armarego [46]. Using tool geometry and material properties, the cutting coefficients contributed by the shear action correspond to:

$$
\begin{aligned}
K_{rc} &= \frac{\tau_s}{\sin\phi_n \cos i}\frac{\sin(\beta_n - \gamma_n)}{\sqrt{\cos^2(\phi_n + \beta_n - \gamma_n) + \tan^2\eta \sin^2\beta_n}} \\
K_{tc} &= \frac{\tau_s}{\sin\phi_n}\frac{\cos(\beta_n - \gamma_n) + \tan\lambda_s \tan\eta \sin\beta_n}{\sqrt{\cos^2(\phi_n + \beta_n - \gamma_n) + \tan^2\eta \sin^2\beta_n}} \\
K_{ac} &= \frac{\tau_s}{\sin\phi_n}\frac{\cos(\beta_n - \gamma_n)\tan\lambda_s - \tan\eta \sin\beta_n}{\sqrt{\cos^2(\phi_n + \beta_n - \gamma_n) + \tan^2\eta \sin^2\beta_n}}
\end{aligned}
\tag{3.10}
$$

where λ_s is the inclination(helix) angle, ϕ_n is the normal shear angle, γ_n is the normal rake angle, η is the chip flow angle, β_n is the normal friction angle, τ_s is the shear yield stress of the workpiece material during cutting.

The cutting force coefficients can also be estimated by implementing mechanistic modeling. In this approach, for a specific tool and workpiece pair, a series of cutting tests are performed and the cutting/edge coefficients are identified by means of the least square curve fitting to the experimental force data [47].

In Eq.(3.4), the process damping force consists of static and dynamic components. However, in Eq.(3.8), only the dynamic part is included since the edge forces share the same effect with the static part of the process damping force. They are both considered as the "ploughing" or "rubbing" at the flank face. In fact, the dynamically changing part of the damping force tries to damp the vibrations, because the direction of the dynamic damping force changes with the slope of the vibration in the r-direction and affects it in such a way that it pulls the tool to its nominal chip thickness value. The damping force added to the radial direction is proportional to the cutting edge length (L) and the damping coefficient (C_i). In the tangential direction, the frictional part of the dynamic process damping force is applied where μ is the friction coefficient.

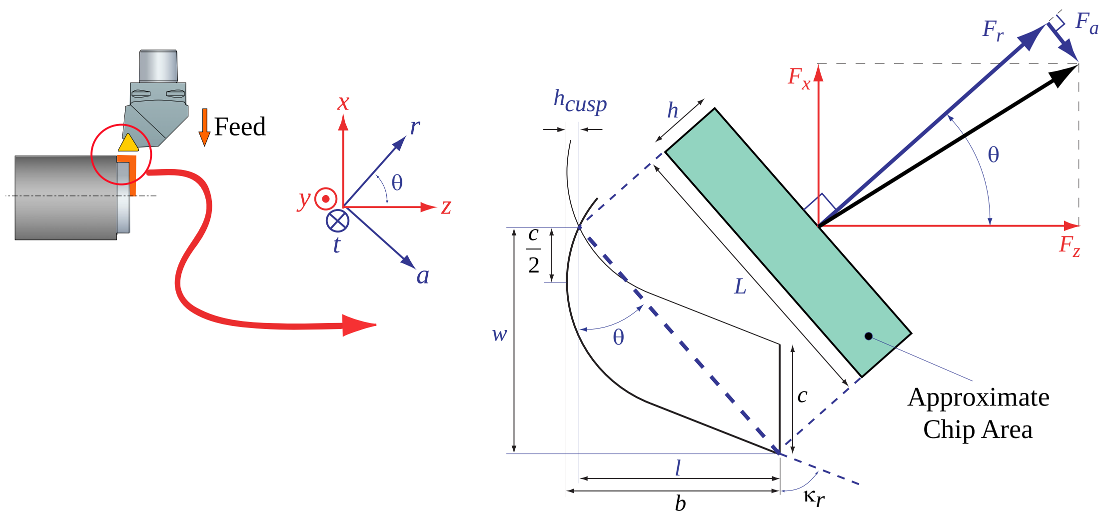

Figure 3-8 : Chip created by actual tool and approximate chip model suggested by Eynian [11]

When an actual tool is taken into consideration, the cutting edge of the insert has a nose radius and an approach angle which make the forces unevenly distributed along the cutting edge of the tool. In this study, an equivalent chip area approach, which is suggested by Eynian [11], [48], is employed by using the chip flow angle theories explained in Section 3.3. Therefore, the directions of the forces are determined according to the new chip flow angle, as illustrated in Figure 3-8. This new chip is a function of the cutting parameters (width of cut, b and feed, c) and the tool geometry (nose radius, r_ε, approach angle, κ_r). The new chip can be defined by introducing the approximate chord length, L, equivalent chip thickness, h, and chord angle, θ, where the angle stands for the orientation of the chip.

The chip parameters are evaluated from Figure 3-8 as follows.

The cusp height is:

$$h_{cusp} = r_\varepsilon - \sqrt{r_\varepsilon^2 - \left(\frac{c}{2}\right)^2} \tag{3.11}$$

The projection of the chord length in the direction of the width of cut is:

$$l = b - h_{cusp} \tag{3.12}$$

The projection of the chord length in the feed direction has three different expressions depending on the width of cut, nose radius and approach angle combination:

If $b \geq r_\varepsilon(1-\cos\kappa_r)$:

$$w = \begin{cases} \dfrac{c}{2} + r_\varepsilon \sin\kappa_r + \dfrac{b - r_\varepsilon(1-\cos\kappa_r)}{\tan\kappa_r} & \text{if } \kappa_r \leq \pi/2 \\ \dfrac{c}{2} + b\cos\kappa_r + r_\varepsilon\left(\sin\kappa_r - \cos\kappa_r + \cos^2\kappa_r\right) & \text{if } \kappa_r > \pi/2 \end{cases} \tag{3.13}$$

If $b < r_\varepsilon(1-\cos\kappa_r)$:

$$w = \frac{c}{2} + \sqrt{r_\varepsilon^2 - (r_\varepsilon - b)^2} \tag{3.14}$$

Three parameters necessary to define the new chip become [11]:

$$\begin{aligned} L &= \sqrt{w^2 + l^2} \\ \theta &= \arctan\left(\frac{l}{w}\right) \\ h &= \frac{A}{L} = \frac{b \cdot c - A_{cusp}}{L} \end{aligned} \tag{3.15}$$

where L, θ and h are the chord length, chord angle and the equivalent chip thickness, respectively.

The cusp area (A_{cusp}) is the region which stays uncut between successive tool passes and it can be calculated as follows:

$$A_{cusp} = c \cdot r_\varepsilon \left[1 - \frac{1}{2}\sqrt{1 - \left(\frac{c}{2r_\varepsilon}\right)^2} \right] - r_\varepsilon^2 \arcsin\left(\frac{c}{2r_\varepsilon}\right) \qquad \text{if} \quad b \geq h_{cusp} \tag{3.16}$$

If the nose radius of the tool and the width of cut are large compared to the feed rate, the cusp area is negligibly small compared to the area spanned by the feed rate and the width of cut. Moreover, a further simplification can be made by neglecting the cusp height when it is very small compared to the width of cut. In that case, chip thickness becomes:

$$h = \frac{b \cdot c - A_{cusp}}{L} \approx \frac{b \cdot c}{L} \approx \frac{l \cdot c}{L} = c.\sin(\theta) \tag{3.17}$$

which replaces Eq.(3.15). The chip area shown in Figure 3-8 is also approximated as:

$$A = L \cdot h \tag{3.18}$$

The forces created during the cutting operation are expressed in the tool coordinate system, i.e. in Figure 3-8 r, t, a coordinates. But the force measurements cannot be conducted in this coordinate frame due to equipment properties; instead, the machine coordinate system is introduced in x, y, z directions. A transformation is required between two frames. The transformation matrix ($\mathbf{C_{mr}}$) is a function of the chord angle (θ):

$$\{x \quad y \quad z\}^{\mathbf{T}} = \mathbf{C_{mr}} \cdot \{r \quad t \quad a\}^{\mathbf{T}} \tag{3.19}$$

where

$$\mathbf{C_{mr}} = \begin{bmatrix} \sin\theta & 0 & -\cos\theta \\ 0 & -1 & 0 \\ \cos\theta & 0 & \sin\theta \end{bmatrix} \tag{3.20}$$

The transformation matrix can be used the other way around as well.

$$\{r \quad t \quad a\}^{\mathbf{T}} = \mathbf{C_{mr}^T} \cdot \{x \quad y \quad z\}^{\mathbf{T}} \tag{3.21}$$

where its inverse is equal to the transpose of it due to orthonormal columns.

$$\mathbf{C}_{\mathbf{mr}}^{\mathbf{T}} = \mathbf{C}_{\mathbf{mr}}^{-1} = \begin{bmatrix} \sin\theta & 0 & \cos\theta \\ 0 & -1 & 0 \\ -\cos\theta & 0 & \sin\theta \end{bmatrix} \tag{3.22}$$

The projections of the cutting forces in feed (x), cutting velocity (y) and width of cut (z) directions (Figure 3-8) are evaluated using $\mathbf{C}_{\mathbf{mr}}$ [49]:

$$\mathbf{F}_{\mathbf{xyz}} = \mathbf{C}_{\mathbf{mr}} \cdot \mathbf{F}_{\mathbf{rta}} \quad \Leftrightarrow \quad \mathbf{F}_{\mathbf{rta}} = \mathbf{C}_{\mathbf{mr}}^{\mathbf{T}} \cdot \mathbf{F}_{\mathbf{xyz}} \tag{3.23}$$

where

$$\mathbf{F}_{\mathbf{xyz}} = \begin{Bmatrix} F_x \\ F_y \\ F_z \end{Bmatrix}, \quad \mathbf{F}_{\mathbf{rta}} = \begin{Bmatrix} F_r \\ F_t \\ F_a \end{Bmatrix} \tag{3.24}$$

Note that forces shown in Figure 3-8 are applied on the insert, and the same forces act in the opposite direction on the workpiece:

$$\mathbf{F}_{\mathbf{xyz}} = \mathbf{F}_{\mathbf{xyz}}^{\mathbf{t}} = -\mathbf{F}_{\mathbf{xyz}}^{\mathbf{w}} \quad \Leftrightarrow \quad \mathbf{F}_{\mathbf{rta}} = \mathbf{F}_{\mathbf{rta}}^{\mathbf{t}} = -\mathbf{F}_{\mathbf{rta}}^{\mathbf{w}} \tag{3.25}$$

where w and t refer to the workpiece and tool, respectively.

3.4.2 Derivation of Characteristic Equation for Plunge Turning

The dynamics of the plunge turning process is derived to analyze its chatter stability [7], [48]. The displacement vector $\{x(s) \quad y(s) \quad z(s)\}^{\mathbf{T}}$ of the structure is expressed as:

$$\begin{Bmatrix} x(s) \\ y(s) \\ z(s) \end{Bmatrix} = \underbrace{\begin{bmatrix} \phi_{xx} & \phi_{xy} & \phi_{xz} \\ \phi_{yx} & \phi_{yy} & \phi_{yz} \\ \phi_{zx} & \phi_{zy} & \phi_{zz} \end{bmatrix}}_{\mathbf{\Phi}(s)} \cdot \begin{Bmatrix} F_x(s) \\ F_y(s) \\ F_z(s) \end{Bmatrix} \tag{3.26}$$

where $\mathbf{\Phi}(s)$ is the transfer function matrix, and $\{F_x(s) \quad F_y(s) \quad F_z(s)\}^{\mathbf{T}}$ is the cutting force vector. Each element of the transfer function matrix $\mathbf{\Phi}(s)$ can be expressed in terms of the modal parameters in Laplace domain:

$$\phi_{pq}(s) = \sum_{i=1}^{n} \frac{\omega_{ni}^2 / k_i}{s^2 + 2\zeta_i \omega_{ni} s + \omega_{ni}^2} \qquad p,q \in (x,y,z) \tag{3.27}$$

where ω_{ni}, ζ_i and k_i are the natural frequency, damping ratio and stiffness of each mode i respectively, and n is the total number of modes considered. The transfer function can be measured in frequency domain by means of modal testing techniques. Modal parameters of each structural mode can be extracted from the measurement data by means of modal analysis.

Note that when the tool and workpiece are both flexible, as shown in Figure 3-9, the cutting forces will lead to vibrations on both the work and tool sides. Since the chip is generated in the workpiece-tool engagement region, one needs to consider the relative movement of the workpiece and tool. The relative displacement of the tool tip with respect to the workpiece is given by:

$$\begin{aligned}
\{x \quad y \quad z\}^{\mathrm{T}} &= \{x^{\mathrm{t}} \quad y^{\mathrm{t}} \quad z^{\mathrm{t}}\}^{\mathrm{T}} - \{x^{\mathrm{w}} \quad y^{\mathrm{w}} \quad z^{\mathrm{w}}\}^{\mathrm{T}} \\
&= \mathbf{\Phi}^{\mathrm{t}}(s)\cdot\mathbf{F}^{\mathrm{t}}_{\mathbf{xyz}} - \mathbf{\Phi}^{\mathrm{w}}(s)\cdot\mathbf{F}^{\mathrm{w}}_{\mathbf{xyz}} \\
&= \mathbf{\Phi}^{\mathrm{t}}(s)\cdot\mathbf{F}^{\mathrm{t}}_{\mathbf{xyz}} - \mathbf{\Phi}^{\mathrm{w}}(s)\cdot\left(-\mathbf{F}^{\mathrm{t}}_{\mathbf{xyz}}\right) \\
&= \underbrace{\left(\mathbf{\Phi}^{\mathrm{t}}(s)+\mathbf{\Phi}^{\mathrm{w}}(s)\right)}_{\mathbf{\Phi}(s)}\cdot\mathbf{F}^{\mathrm{t}}_{\mathbf{xyz}} \\
&= \mathbf{\Phi}(s)\cdot\mathbf{F}_{\mathbf{xyz}}
\end{aligned} \tag{3.28}$$

where $\mathbf{\Phi}^{\mathrm{t}}(s)$, $\mathbf{F}^{\mathrm{t}}_{\mathbf{xyz}}$, $\mathbf{\Phi}^{\mathrm{w}}(s)$, $\mathbf{F}^{\mathrm{w}}_{\mathbf{xyz}}$ and $\mathbf{\Phi}(s)$, $\mathbf{F}_{\mathbf{xyz}}$ are tool, workpiece and relative transfer function and force components, respectively.

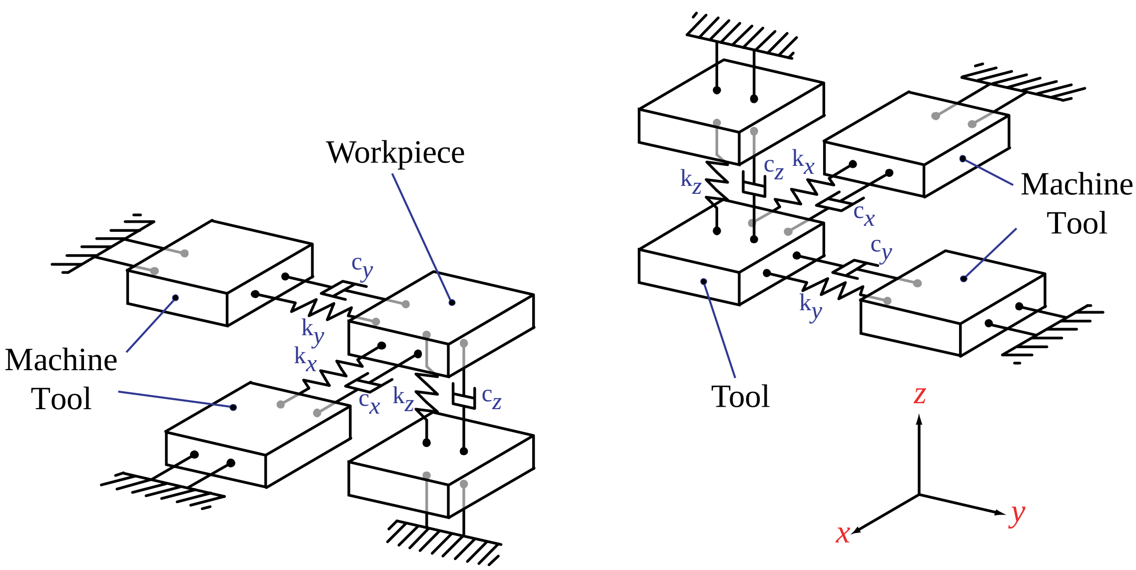

Figure 3-9 : Flexibilities of workpiece and tool side on a machine tool

Due to flexibilities in the structure, the system is prone to vibrations during the cutting operation. The vibrations lead to change in the chip area and thus, the amount of material removal. As a result, it leads the cutting forces to fluctuate as well. Since chip approximation is carried out in the previous section, and the new chip is defined in r,t,a coordinates, the flexibilities in the r,t,a coordinates are expressed as:

$$\begin{aligned}
\{r \quad t \quad a\}^{\mathbf{T}} &= \mathbf{C}_{\mathbf{mr}}^{\mathbf{T}} \cdot \{x \quad y \quad z\}^{\mathbf{T}} \\
&= \mathbf{C}_{\mathbf{mr}}^{\mathbf{T}} \cdot \mathbf{\Phi}(s) \cdot \mathbf{F}_{\mathbf{xyz}} \\
&= \underbrace{\mathbf{C}_{\mathbf{mr}}^{\mathbf{T}} \cdot \mathbf{\Phi}(s) \cdot \mathbf{C}_{\mathbf{mr}}}_{\mathbf{\Phi}_{\mathbf{rta}}(s)} \cdot \mathbf{F}_{\mathbf{rta}} \\
&= \mathbf{\Phi}_{\mathbf{rta}}(s) \cdot \mathbf{F}_{\mathbf{rta}}
\end{aligned} \tag{3.29}$$

where $\mathbf{\Phi}_{\mathbf{rta}}(s)$ denotes the relative transfer function of the tool tip with respect to the workpiece in tool coordinates. Furthermore, $\mathbf{\Phi}_{\mathbf{rta}}(s)$ can be illustrated explicitly as:

$$\mathbf{\Phi}_{\mathbf{rta}}(s) = \begin{bmatrix} \phi_{rr} & \phi_{rt} & \phi_{ra} \\ \phi_{tr} & \phi_{tt} & \phi_{ta} \\ \phi_{ar} & \phi_{at} & \phi_{aa} \end{bmatrix} \tag{3.30}$$

where each element of Eq.(3.30) is:

$$\begin{aligned}
\phi_{rr} &= \cos(\theta)\left(\phi_{zz}\cos(\theta)+\phi_{xz}\sin(\theta)\right)+\sin(\theta)\left(\phi_{zx}\cos(\theta)+\phi_{xx}\sin(\theta)\right) \\
\phi_{rt} &= -\phi_{zy}\cos(\theta)-\phi_{xy}\sin(\theta) \\
\phi_{ra} &= \sin(\theta)\left(\phi_{zz}\cos(\theta)+\phi_{xz}\sin(\theta)\right)-\cos(\theta)\left(\phi_{zx}\cos(\theta)+\phi_{xx}\sin(\theta)\right) \\
\phi_{tr} &= -\phi_{yz}\cos(\theta)-\phi_{yx}\sin(\theta) \\
\phi_{tt} &= \phi_{yy} \\
\phi_{ta} &= \phi_{yx}\cos(\theta)-\phi_{yz}\sin(\theta) \\
\phi_{ar} &= -\cos(\theta)\left(\phi_{xz}\cos(\theta)-\phi_{zz}\sin(\theta)\right)-\sin(\theta)\left(\phi_{xx}\cos(\theta)-\phi_{zx}\sin(\theta)\right) \\
\phi_{at} &= \phi_{xy}\cos(\theta)-\phi_{zy}\sin(\theta) \\
\phi_{aa} &= \cos(\theta)\left(\phi_{xx}\cos(\theta)-\phi_{zx}\sin(\theta)\right)-\sin(\theta)\left(\phi_{xz}\cos(\theta)-\phi_{zz}\sin(\theta)\right)
\end{aligned} \tag{3.31}$$

The chip area can also be described as the region between two successive tool passes which are a spindle period (τ) apart from each other. Any movement during the previous cut and/or the current cut will lead to a change in the chip area. However, the vibrations in the cutting velocity direction (y in Figure 3-10) have a negligible effect on the chip area formation, so only vibrations in the width of cut (z) and feed (x) directions are considered to modulate the chip area in this study. An equivalent chip modulation is considered in an approximated chip as well. The combined effect of the two directions is regarded as vibrations in the chip flow direction in the new model, as illustrated in Figure 3-10. The variation in the relative distance between the successive cuts in the r direction is taken as the main source of the dynamically changing forces. This variation also corresponds to the phase difference (ε) between consecutive vibrations in the r direction. In that sense, the dynamic chip thickness is given as:

$$h_d(t) = h - \left[r(t) - r(t-\tau) \right] \tag{3.32}$$

where $r(t), r(t-\tau)$ and τ refer to the current vibrations, previous vibrations and the spindle period, respectively.

In order to obtain the characteristic equation from Eq.(3.32), a relationship between vibrations in the r direction and the dynamic chip thickness (h_d) is needed.

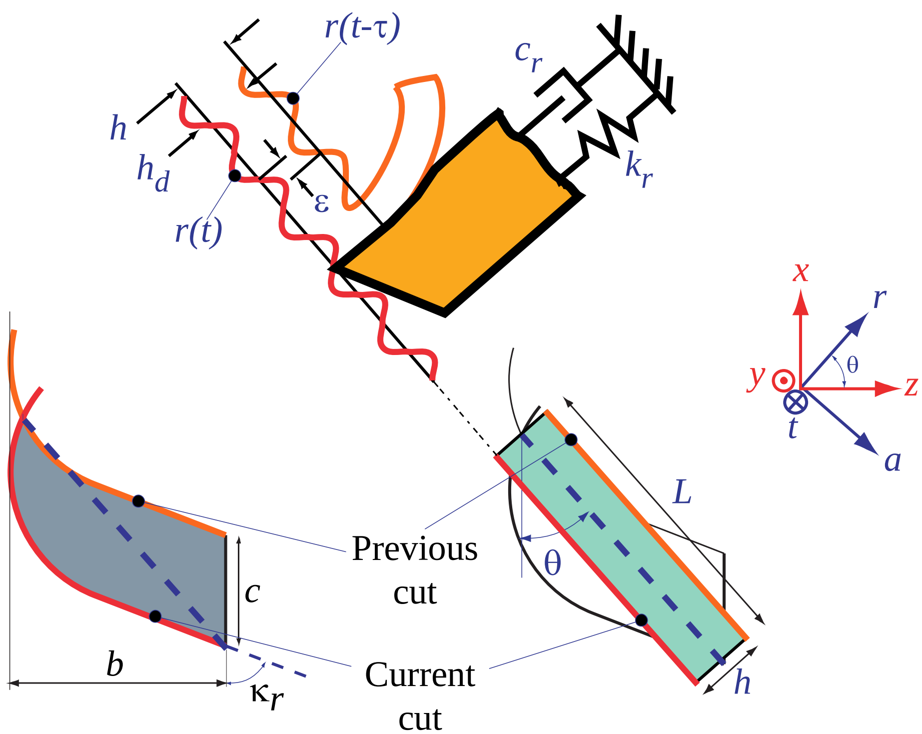

Figure 3-10 : Chip modulation and regeneration effect

From Eq.(3.29) and Eq.(3.30):

$$
\begin{aligned}
r(s) &= \underbrace{\{\phi_{rr} \quad \phi_{rt} \quad \phi_{ra}\}}_{\mathbf{\Phi_{r,rta}}(s)} \cdot \mathbf{F_{rta}}(s) \\
r(s) &= \mathbf{\Phi_{r,rta}}(s) \cdot \mathbf{F_{rta}}(s)
\end{aligned}
\tag{3.33}
$$

where $\mathbf{\Phi_{r,rta}}(s)$ is the transfer function in the r direction only. Substituting force and chip area expressions from Eq.(3.9) and Eq.(3.18) into Eq.(3.33) and converting force into Laplace domain yield to:

$$
\begin{aligned}
r(s) &= \mathbf{\Phi_{r,rta}}(s) \cdot \left(\mathbf{K_c} \cdot L h_d(s) - \mathbf{P_d} \cdot s \frac{C_i L}{V_c} r(s) \right) \\
r(s) &= \frac{L \cdot \mathbf{\Phi_{r,rta}}(s) \cdot \mathbf{K_c}}{1 + s \dfrac{C_i L}{V_c} \cdot \mathbf{\Phi_{r,rta}}(s) \cdot \mathbf{P_d}} \cdot h_d(s)
\end{aligned}
\tag{3.34}
$$

The relation between vibrations in the r-direction and the dynamic chip thickness is obtained in Eq.(3.34). Note that the edge forces are dropped from the total forces because they do not change in time, thus they do not affect the stability of the system.
The dynamic chip thickness in Eq.(3.32) is converted in to Laplace domain as:

$$
h_d(s) = h - \left(1 - e^{-s\tau}\right) r(s) \tag{3.35}
$$

The transfer function between the static chip thickness h and the dynamic chip thickness h_d can easily be obtained from Equations (3.34) and (3.35) as:

$$
\frac{h_d(s)}{h(s)} = \frac{1}{1 + \left(1 - e^{-s\tau}\right) \cdot \dfrac{L \cdot \mathbf{\Phi_{r,rta}}(s) \cdot \mathbf{K_c}}{1 + s \dfrac{C_i L}{V_c} \cdot \mathbf{\Phi_{r,rta}}(s) \cdot \mathbf{P_d}}} \tag{3.36}
$$

which can be rewritten as:

$$
\frac{h_d(s)}{h(s)} = \frac{1 + s \dfrac{C_i L}{V_c} \cdot \mathbf{\Phi_{r,rta}}(s) \cdot \mathbf{P_d}}{1 + s \dfrac{C_i L}{V_c} \cdot \mathbf{\Phi_{r,rta}}(s) \cdot \mathbf{P_d} + \left(1 - e^{-s\tau}\right) \cdot L \cdot \mathbf{\Phi_{r,rta}}(s) \cdot \mathbf{K_c}} \tag{3.37}
$$

The right hand side of Eq.(3.37) is the transfer function of the dynamic system in s domain. The characteristic equation is given by the denominator of the transfer function:

$$1+s\frac{C_i L}{V_c}\cdot\mathbf{\Phi}_{\mathbf{r,rta}}(s)\cdot\mathbf{P_d}+\left(1-e^{-s\tau}\right)\cdot L\cdot\mathbf{\Phi}_{\mathbf{r,rta}}(s)\cdot\mathbf{K_c}=0 \tag{3.38}$$

The dynamics of the cutting system is represented by the block diagram shown in Figure 3-11.

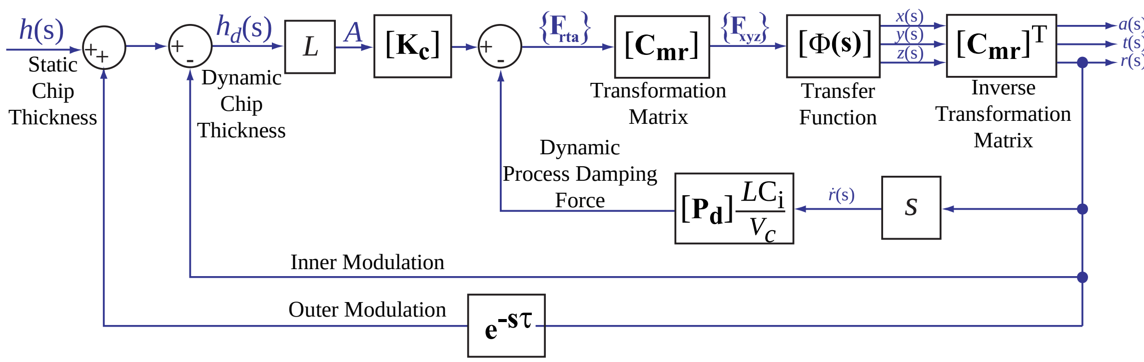

Figure 3-11 : Block diagram of the dynamic plunge turning operation

3.5 Identification of Process Damping Coefficient from Plunge Turning

Kurata et al.[51] first used the plunge turning operation to identify the process damping coefficient. In this study, Eynian's [11] detailed approximate chip model is added and flexibilities in all three orthogonal directions are included in the identification method. The damping coefficient C_i is identified from the characteristic equation of plunge turning. When the cutting process is critically stable, the real part of the characteristic equation becomes zero, i.e. $s = j\omega_c$. The system vibrates with a constant amplitude at chatter frequency ω_c. When the system is critically stable, the characteristic equation can be written in frequency domain by replacing the Laplace operator s with $j\omega_c$ where $j=\sqrt{-1}$ and ω_c is the chatter frequency.

$$1+j\omega_c\frac{C_i L}{V_c}\cdot\mathbf{\Phi}_{\mathbf{r,rta}}(j\omega_c)\cdot\mathbf{P_d}+\left(1-e^{-j\omega_c\tau}\right)\cdot L\cdot\mathbf{\Phi}_{\mathbf{r,rta}}(j\omega_c)\cdot\mathbf{K_c}=0 \tag{3.39}$$

Since Eq.(3.39) has real and imaginary parts, both must be zero in order to satisfy the equilibrium. This suggests that for each chatter frequency, there are two possible damping coefficients (C_i): one for the real part of the equation ($C_{i,1}$) and one for the imaginary part of the equation ($C_{i,2}$). These are expressed in Eq.(3.40) by using Euler's formula ($e^{jx} = \cos(x) + j\sin(x)$):

$$C_{i,1} = \frac{V_{lim}}{\omega_c\left(\phi_{rr,I} + \mu\phi_{rt,I}\right)} \cdot \left(\begin{array}{l} \frac{1}{L} + \\ \left[1 - \cos\left(\omega\tau\right)\right]\left(K_{rc}\phi_{rr,R} + K_{tc}\phi_{rt,R} + K_{ac}\phi_{ra,R}\right) - \\ \sin\left(\omega\tau\right)\left(K_{rc}\phi_{rr,I} + K_{tc}\phi_{rt,I} + K_{ac}\phi_{ra,I}\right) \end{array} \right)$$

$$C_{i,2} = \frac{-V_{lim}}{\omega\left(\phi_{rr,R} + \mu\phi_{rt,R}\right)} \cdot \left(\begin{array}{l} \left[1 - \cos\left(\omega\tau\right)\right]\left(K_{rc}\phi_{rr,I} + K_{tc}\phi_{rt,I} + K_{ac}\phi_{ra,I}\right) + \\ \sin\left(\omega\tau\right)\left(K_{rc}\phi_{rr,R} + K_{tc}\phi_{rt,R} + K_{ac}\phi_{ra,R}\right) \end{array} \right) \tag{3.40}$$

where V_{lim} is the surface speed at the critically stable condition, $\phi_{rr,R}, \phi_{rt,R}, \phi_{ra,R}$ are the real parts and $\phi_{rr,I}, \phi_{rt,I}, \phi_{ra,I}$ are the imaginary parts of the corresponding transfer functions given in Eq.(3.31).

The process damping coefficient is obtained by looking for a value of ω in the neighbourhood of the measured chatter frequency ω_c for which the following condition holds:

$$C_i = C_{i,1} = C_{i,2} > 0 \tag{3.41}$$

The parameters in Eq.(3.40) can be measured and calculated as follows. Cutting coefficients (K_{rc}, K_{tc}, K_{ac}) can be estimated as given in Section 3.4.1. The relative transfer function of the structure ($\phi_{rr}, \phi_{rt}, \phi_{ra}$) can be measured by modal testing. The friction coefficient (μ) is a material property, for instance it is 0.3 for steel [24]. However, the surface speed at the critically stable condition (V_{lim}) is identified from the plunge turning tests. The surface speed V reduces as the tool plunges into the workpiece, i.e. D reduces:

$$V = \frac{n \cdot D}{60} \tag{3.42}$$

where n is the spindle speed in [rpm] and D is the diameter of the cylindrical workpiece in [m]. The critical velocity (V_{lim}) is distinguished when the system experiences a transition from an unstable cutting to a stable cutting, see Figure 3-12. When the speed is low, the effect of the speed dependent process damping increases and, after some point, this leads to a chatter free cutting operation.

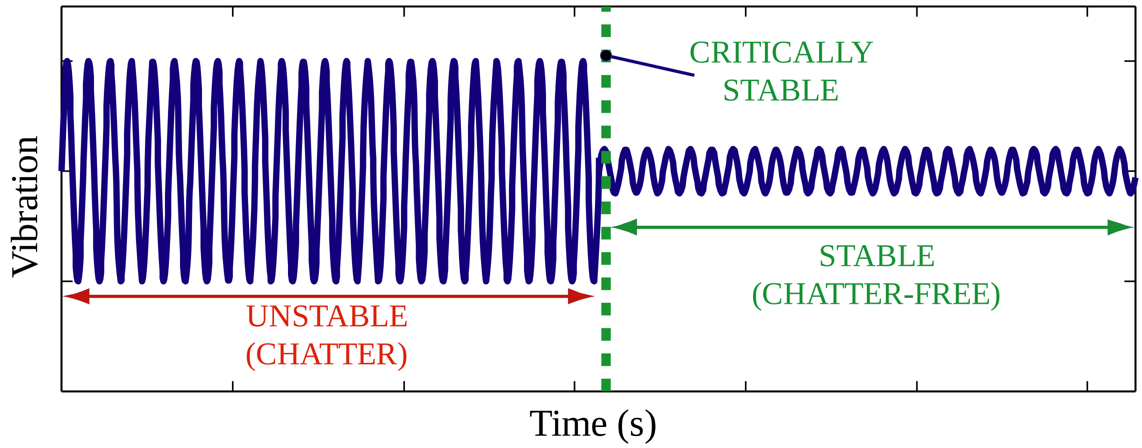

Figure 3-12 : Transition from unstable cutting to stable cutting

The identification method applies the criterion given in Eq.(3.41), which is necessary but not sufficient for the system to be critically stable. Although the criterion is satisfied, the system can still be unstable. The Nyquist stability criterion is applied in order to make sure the dynamic system is critically stable with the identified process damping coefficient. A flowchart which summarizes the identification method is illustrated in Figure 3-13.

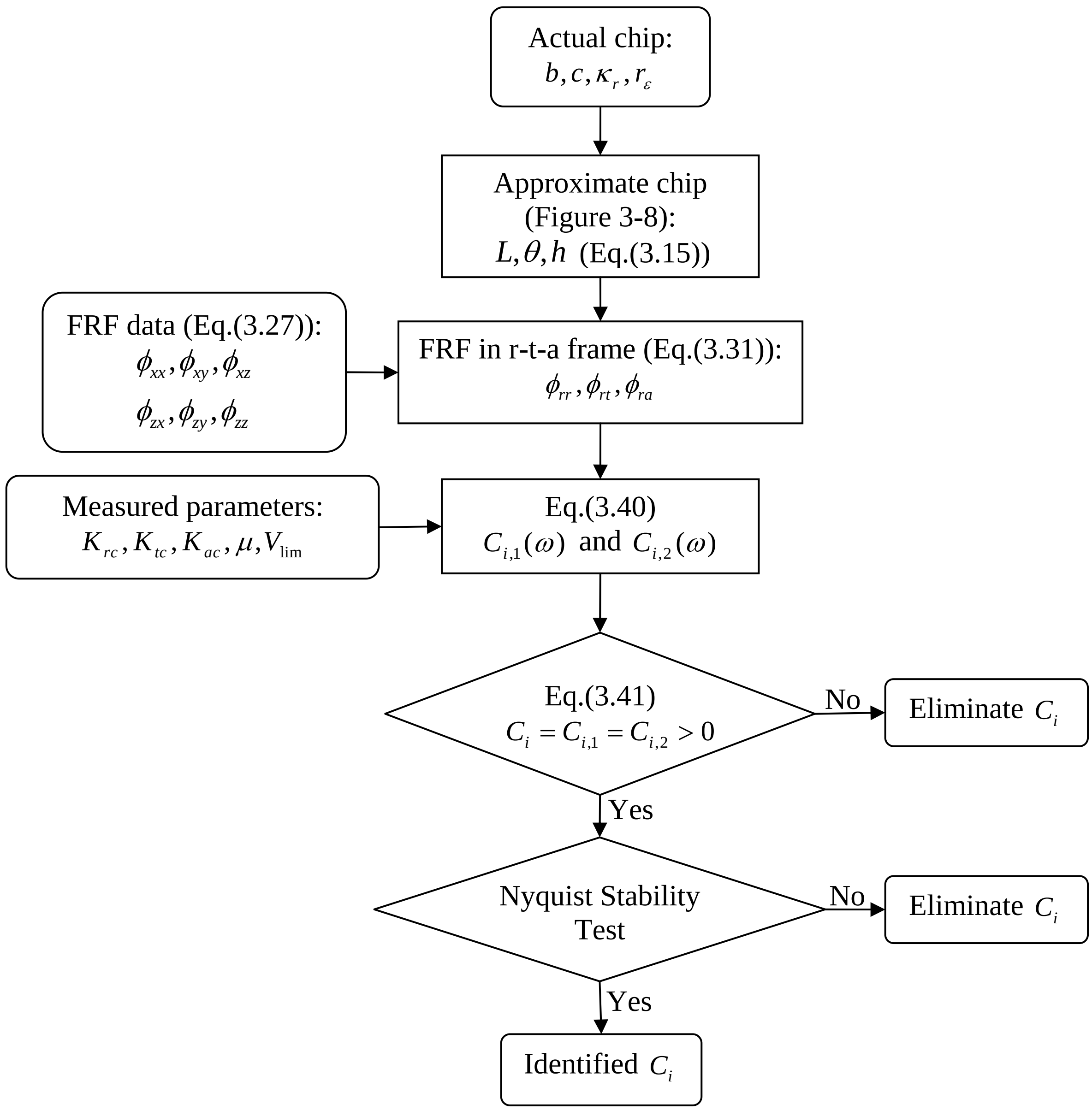

Figure 3-13 : Flowchart for identification of process damping coefficient

3.6 Experimental Results

In this section, experimental studies to identify the process damping coefficient are presented. Since the purpose is to see the transition from unstable to stable cutting, a long cylindrical workpiece is used to create a flexible system which is prone to chatter. The frequency response function is measured by using an instrumented hammer and an accelerometer as presented in Figure 3-14.

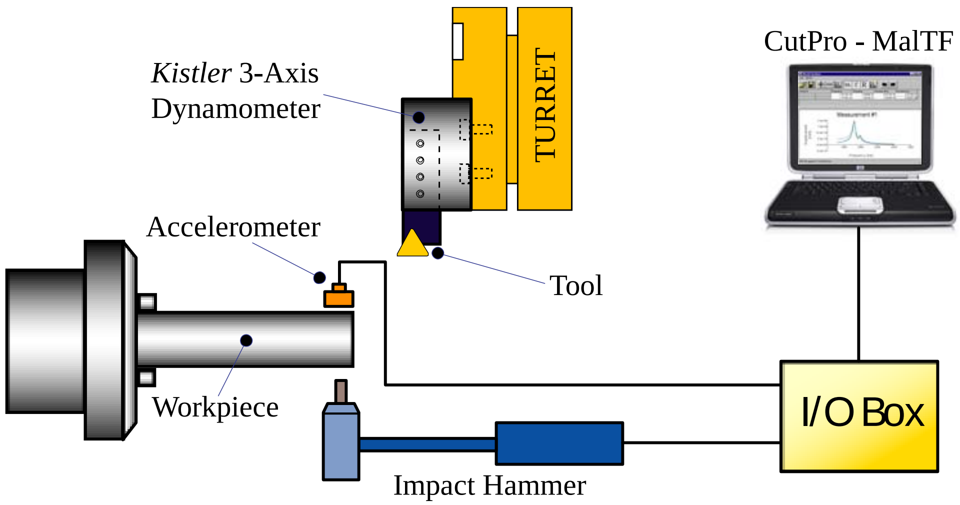

Figure 3-14 : Experimental setup for FRF measurement

The cutting forces are measured using a dynamometer, and the sound created during the cutting operation is recorded using a microphone. The cutting experiment setup is given in Figure 3-15. All of the experiments are conducted on the Hardinge Superslant turning machine.

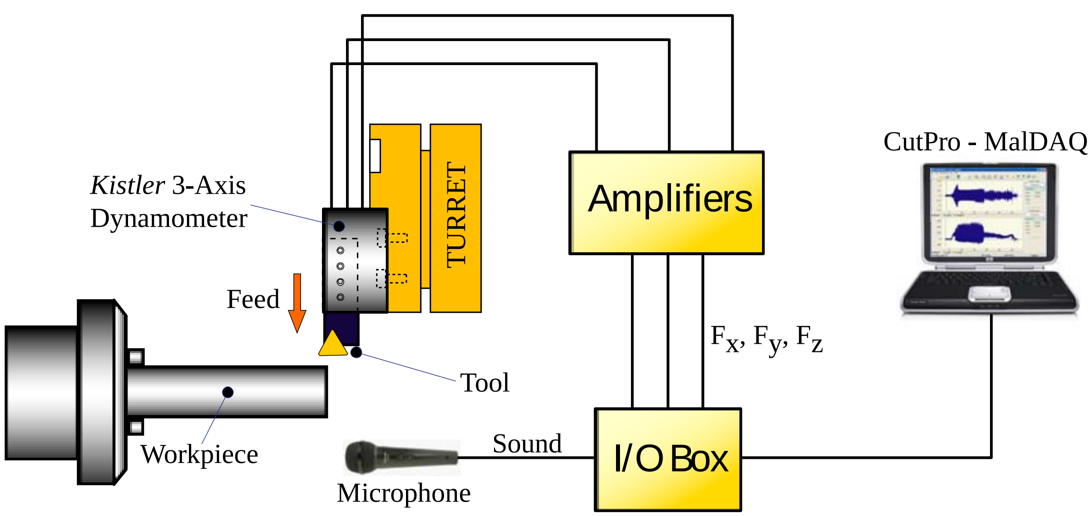

Figure 3-15 : Experimental setup for plunge turning tests

3.6.1 Identification Results

A cold rolled AISI 1045 steel with 232 HB hardness is used during the tests. Specifications of the workpiece and insert, which are used in tests, are given in Table 3.2.

Table 3.2 : Tool and workpiece specifications

Insert	Type	TNMA 16 04 08-KR 3205
	Nose radius [mm]	0.8
	Rake angle [°]	-6
	Helix angle [°]	-6
	Approach angle [°]	91
Workpiece	Material	AISI 1045
	Diameter [mm]	41.275
	Hardness [HB]	232

The cutting coefficients of the tool-workpiece are obtained from the chatter-free force measurements (Figure 3-16) and given in Table 3.3.

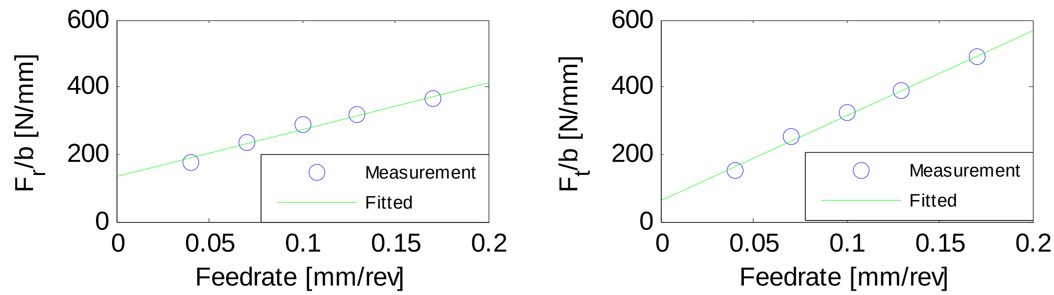

Figure 3-16 : Cutting forces F_r and F_t for different feed rates c at 2 mm width of cut, 2000 rpm spindle speed and 80 mm length of workpiece

Table 3.3 : Cutting force coefficients for steel 1045

$K_{rc}\ [N/mm^2]$	1413	$K_{re}\ [N/mm]$	131
$K_{tc}\ [N/mm^2]$	2530	$K_{te}\ [N/mm]$	62
$K_{ac}\ [N/mm^2]$	0	$K_{re}\ [N/mm]$	0

The flexibilities of both the workpiece and tool are measured in frequency domain. The workpiece length is kept at 250 mm. Since the workpiece is very long, it is more flexible than the tool as seen in Figure 3-17. Only the FRF measurements necessary for calculating the transfer function in the chip flow direction are provided, as suggested in

Eq.(3.31) and Eq.(3.39). The most dominant mode is at 349 Hz which is the first bending mode of the workpiece.

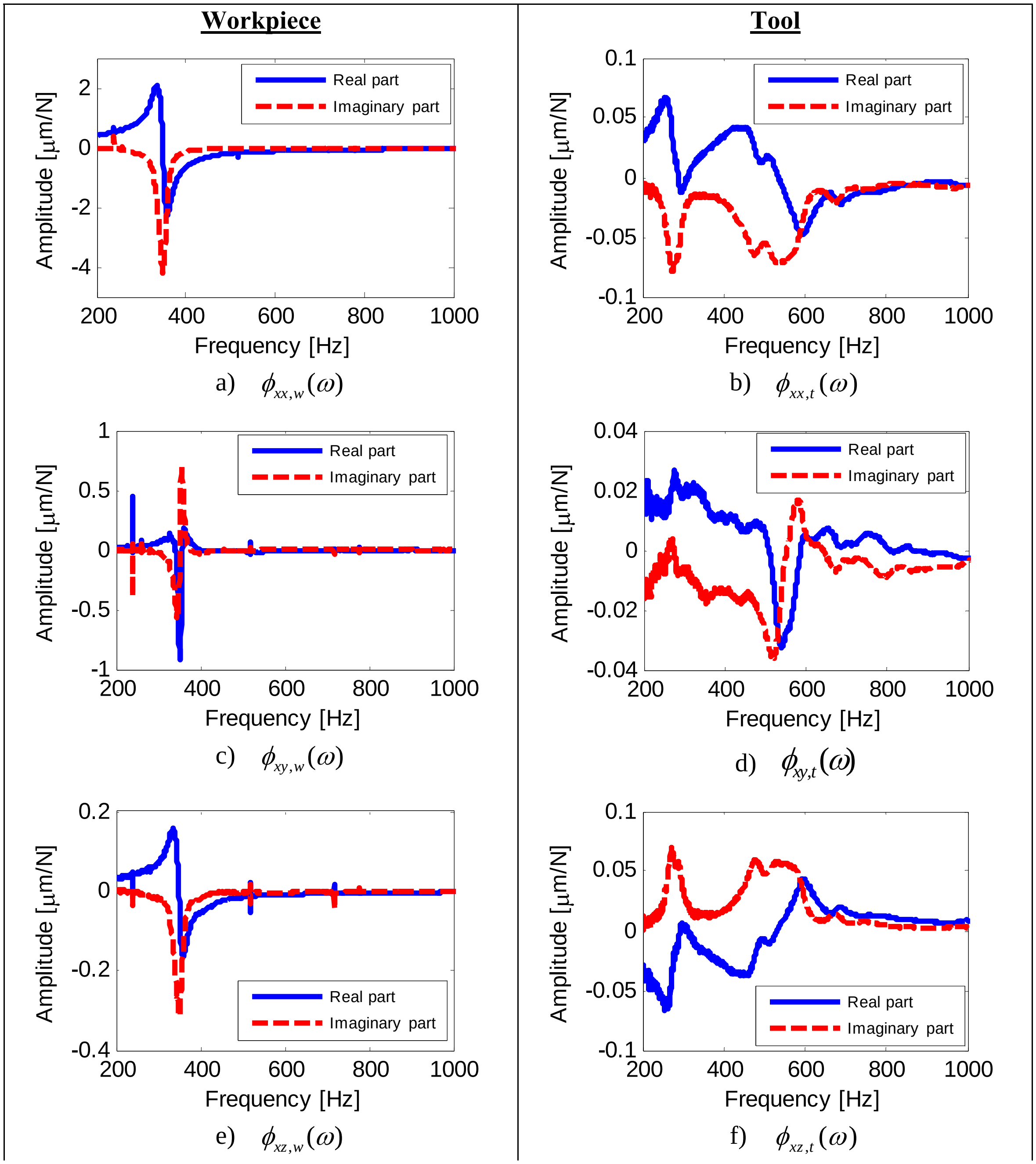

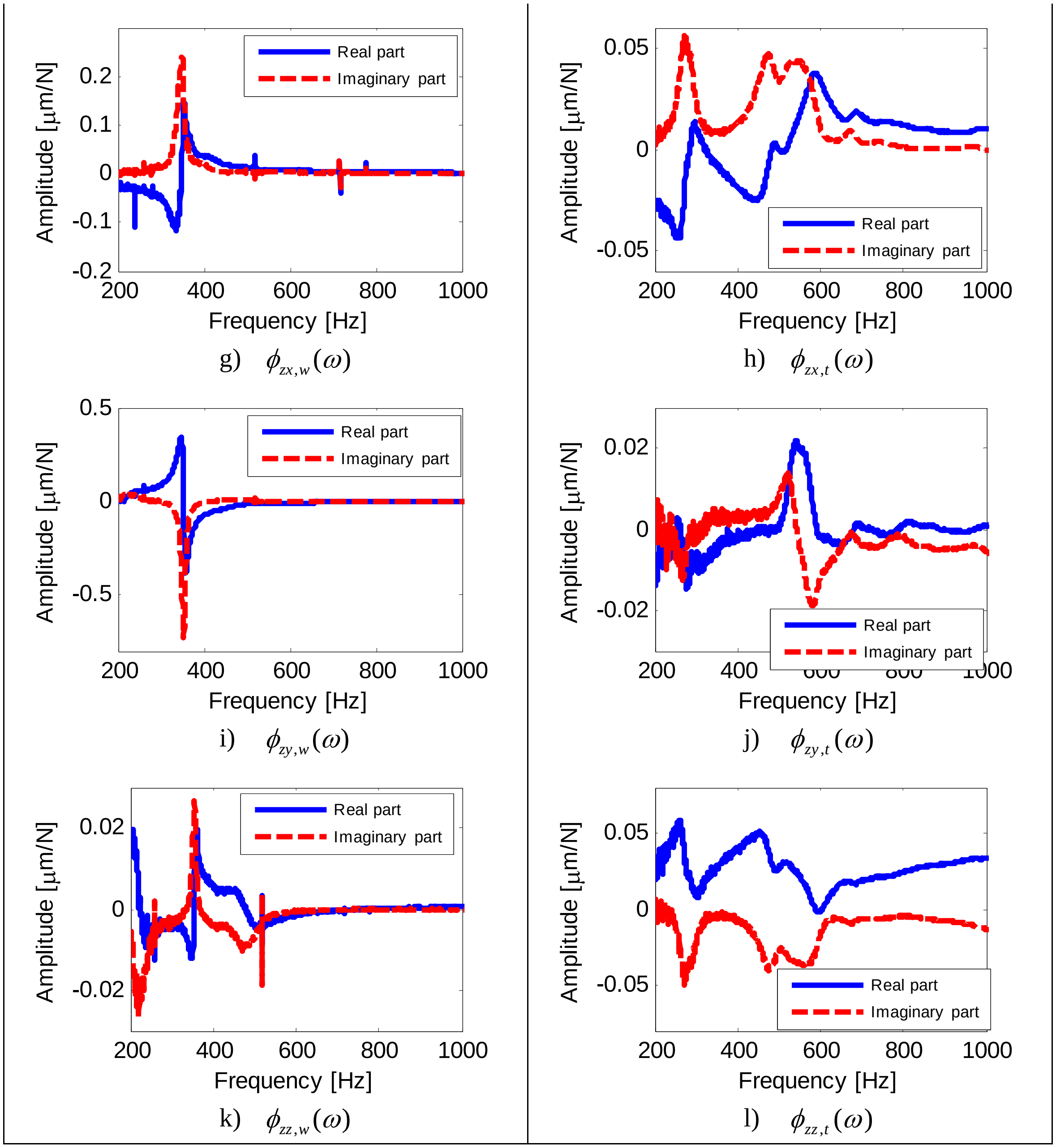

Figure 3-17 : Measured frequency response functions of workpiece (250 mm, steel 1045) and tool in machine coordinates

The force and sound are measured using the experimental setup shown in Figure 3-15. The workpiece is 250 mm long. Orthogonal plunge turning tests are conducted for two sets of cutting conditions listed in Table 3.4. Since the effect of the process damping is greater at low speeds, a low spindle speed of 1000 rpm is used for the tests. Five cutting tests are conducted for each set of conditions.

Table 3.4 : Cutting conditions for process damping coefficient identification of AISI 1045

	Quantity	Symbol	Size
Set 1	Width of cut [mm]	b	0.6
	Feed rate [mm/rev]	c	0.05
	Spindle speed [rpm]	n	1000
Set 2	Width of cut [mm]	b	0.7
	Feed rate [mm/rev]	c	0.10
	Spindle speed [rpm]	n	1000

Figure 3-18b shows the cutting forces in the chip flow direction (F_r) for one of the measurements of the first set of cutting conditions. The corresponding sound data is shown in Figure 3-18a. Both measurements experience an unstable cutting with large chatter vibrations in the beginning and a stable cutting with small vibrations after some time. As the workpiece diameter reduces, so does the cutting velocity, the process damping effect becomes dominant and transition occurs at the critical cutting velocity. In other words, the sound and cutting forces start attenuating after critical velocity. The sound and force measurements suggest that this transition happens approximately after 13.6 seconds, which corresponds to a workpiece diameter of 18.6 mm and a critical cutting velocity of 58.5 m/min.

Frequency content of the force and sound data is calculated by taking fast Fourier transform (FFT) of the signals. For the time range of 3 to 13 seconds, chatter vibrations are clearly visible and chatter frequency is 381 Hz as shown in Figure 3-19(a-c). However chatter vanishes for the time range of 15 to 24 seconds. Frequency content is not dominated by any of the frequencies as in Figure 3-19(b-d).

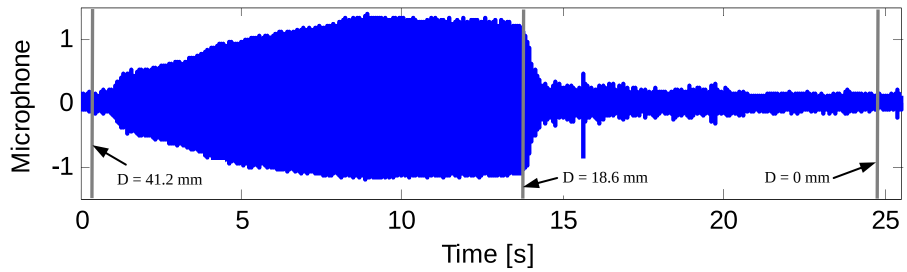

a) Sound measurement

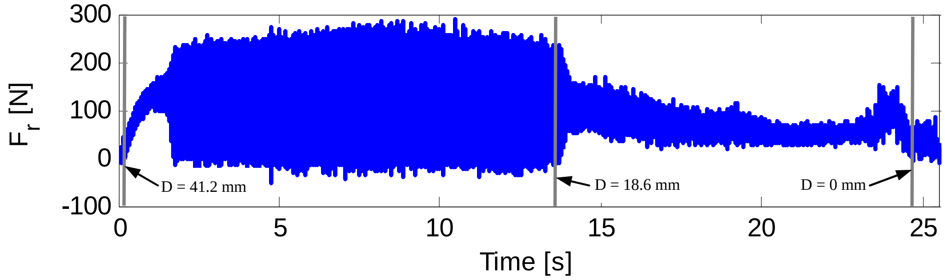

b) Force Measurement

Figure 3-18 : Sound (a) and force (b) measurement in time domain with cutting conditions of set 1 as given in Table 3.4

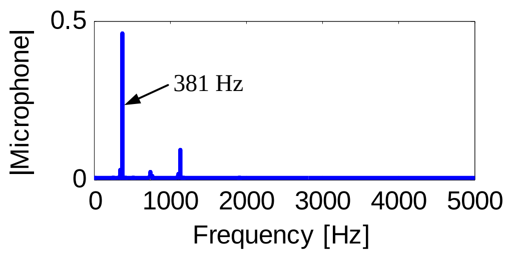

a) Sound FFT from 3 to 13 seconds (Unstable)

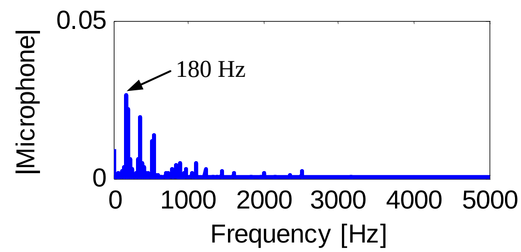

b) Sound FFT from 15 to 24 seconds (Stable)

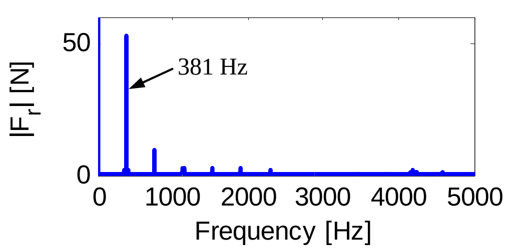

c) Force FFT from 3 to 13 seconds(Unstable)

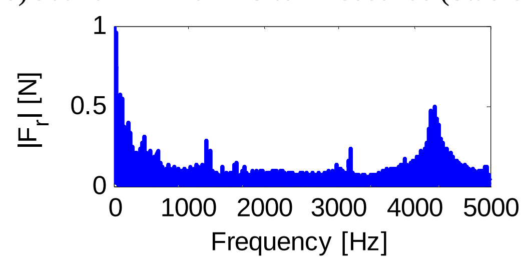

d) Force FFT from 15 to 24 seconds (Stable)

Figure 3-19 : Sound (a-b) and force (c-d) measurement in frequency domain for cutting conditions of set 1 as given in Table 3.4

For the second set of cutting conditions (see Table 3.4), the sound and force measurements are illustrated in Figure 3-20(a-b). In that case, the transition from unstable to stable cutting is not as clear in the force and sound data as it is in the first set. However, when FFT of the force and sound data are taken for the time range of 1 to 7 seconds, chatter can be noticed clearly at a frequency of 381 Hz, see Figure 3-21(a-c). For the time range of 8 to 12 seconds, chatter disappears as shown in Figure 3-21(b-d).

Although the contribution of chatter is not enough to distinguish it clearly in the force and sound measurements, frequency analysis proves that the transition from unstable to stable cutting exists in the second set of cutting conditions. The transition occurs at a time of 7.5 seconds, which corresponds to the workpiece diameter of 16.5 mm and the critical cutting velocity of 51.8 m/min.

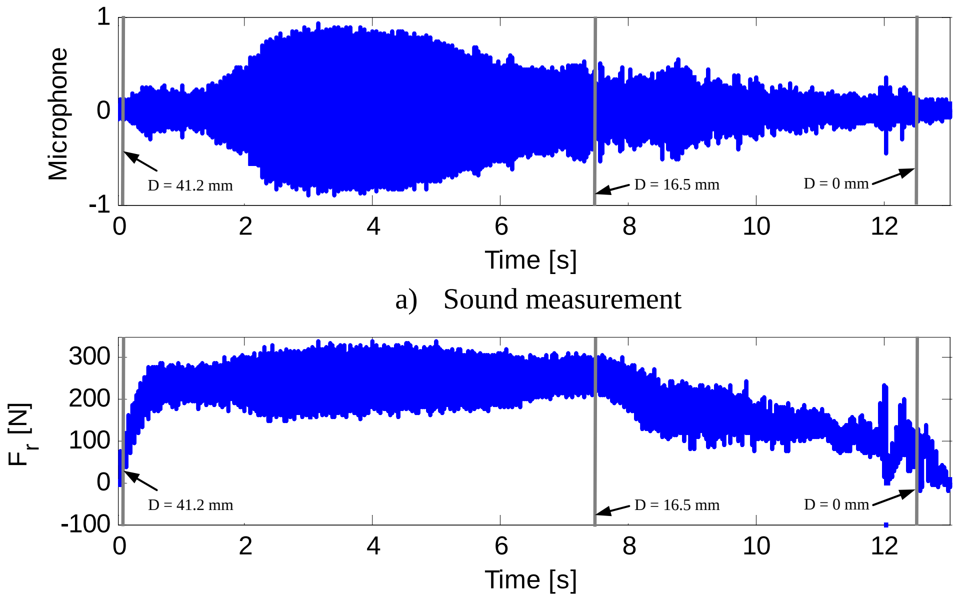

a) Sound measurement

b) Force Measurement

Figure 3-20 : Sound (a) and force (b) measurement in time domain with cutting conditions of set 2 as given in Table 3.4

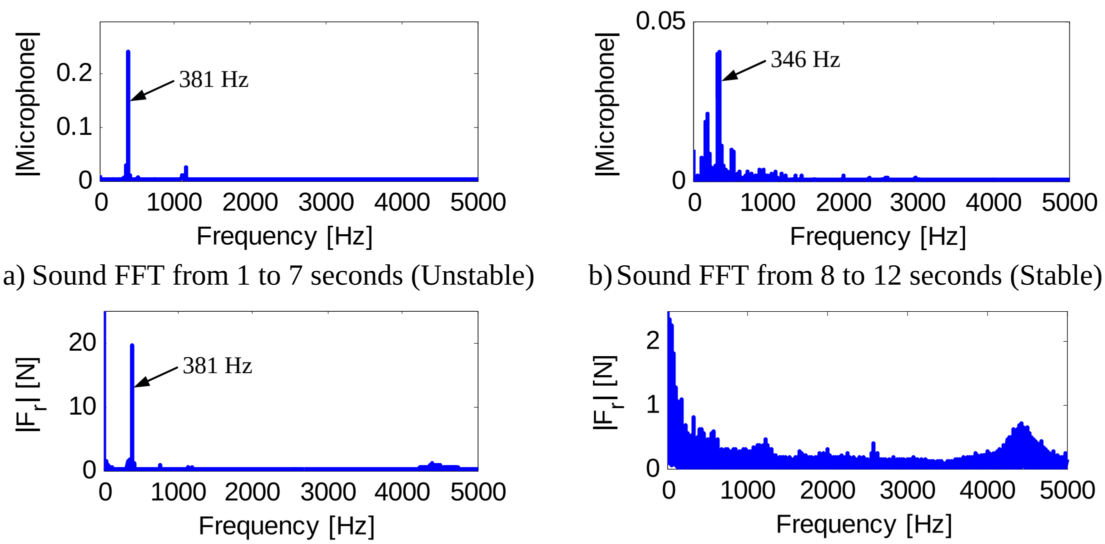

a) Sound FFT from 1 to 7 seconds (Unstable)

b) Sound FFT from 8 to 12 seconds (Stable)

c) Force FFT from 1 to 7 seconds(Unstable)

d) Force FFT from 8 to 12 seconds (Stable)

Figure 3-21 : Sound (a-b) and force (c-d) measurement in frequency domain for cutting conditions of set 2 as given in Table 3.4

Among the five tests conducted for each set of cutting conditions, the calculated critical velocities do not deviate more than 4 m/min. Thus, the calculated critical velocities listed in Table 3.5 are used for identification of the process damping coefficient.

Table 3.5 : Critical cutting velocities for AISI 1045 steel

	Quantity	Symbol	Size
Set 1	Critical cutting velocity [m/min]	V_{lim}	58.5
Set 2	Critical cutting velocity [m/min]	V_{lim}	51.8

Having all of the parameters in Eq.(3.40), the damping coefficients can be calculated from the real part ($C_{i,1}$) and the imaginary part ($C_{i,2}$) of the characteristic equation at a range of frequencies within the neighbourhood of a chatter frequency of 381 Hz. Variation of the damping coefficient (C_i) with frequency is illustrated in Figure 3-22 for both set 1 and set 2 conditions.

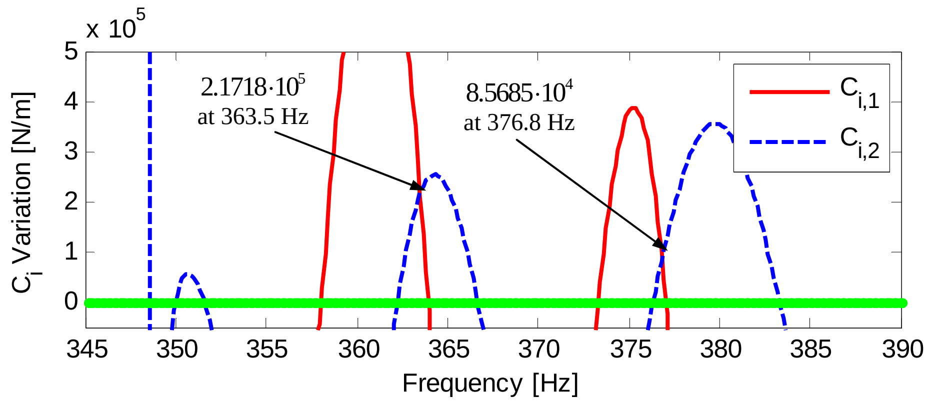

a) Variation of $C_{i,1}$ and $C_{i,2}$ for set 1 conditions

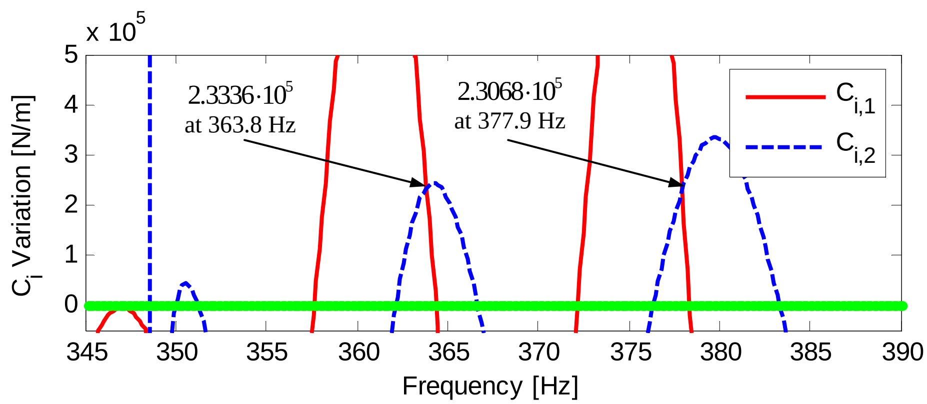

b) Variation of $C_{i,1}$ and $C_{i,2}$ for set 2 conditions

Figure 3-22 : Process damping coefficient variation in neighbourhood of chatter frequency 381 Hz. See Table 3.4 for cutting conditions

C_i values, which satisfy the condition specified in Eq.(3.41), are of interest in this case because only those values guarantee that both the real and the imaginary parts of the characteristic equation are zero. There are numerous C_i values which satisfy this condition throughout the frequency range. There are even 2 C_i values at frequencies close to the chatter frequency as shown in Figure 3-22 for each set of conditions. The Nyquist stability criterion is used to check whether the corresponding C_i value satisfies the critical stability of the dynamic plunge turning operation. The Nyquist plots of the characteristic equation (see Eq.(3.39)) are illustrated in Figure 3-23. Figures (a) and (b) show that the system is critically stable as both of the curves pass through (0,0) without encircling it. Although the curves are passing through (0,0) point in figures (c) and (d), they also encircle (0,0) point which makes the dynamic system unstable (see section 3.6.2 for more details). As a result, C_i values in (c) and (d) are eliminated from the identification procedure by the Nyquist criteria.

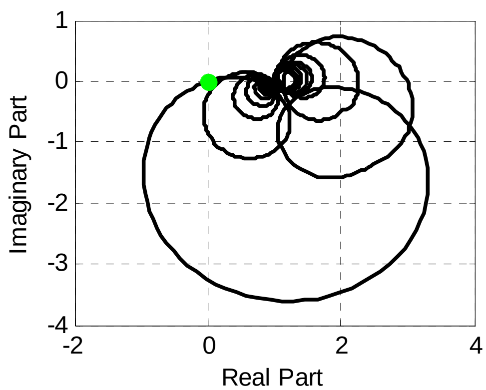

a) Set 1 : $C_i = 2.1718 \cdot 10^5 \ N/m$

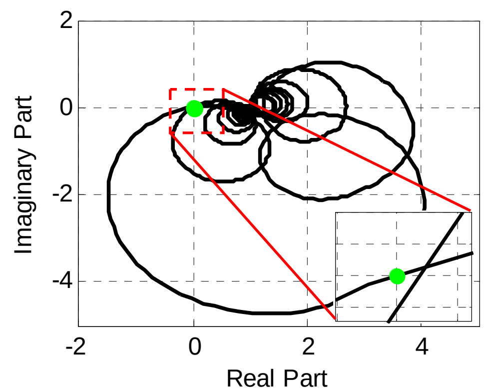

b) Set 2 : $C_i = 2.3336 \cdot 10^5 \ N/m$

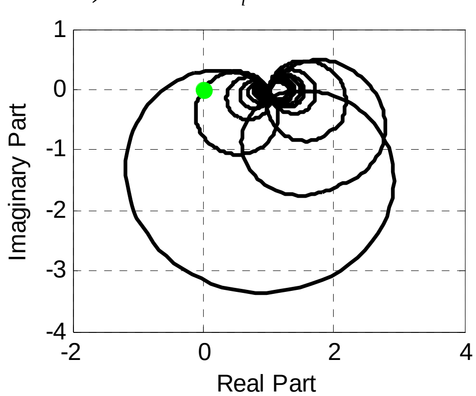

c) Set 1 : $C_i = 0.8568 \cdot 10^5 \ N/m$

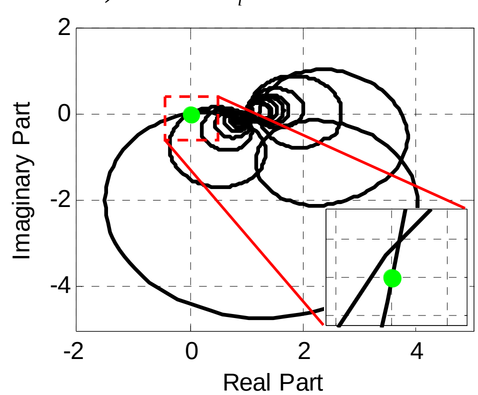

d) Set 2 : $C_i = 2.3068 \cdot 10^5 \ N/m$

Figure 3-23 : Nyquist diagrams of characteristic equation for conditions of set 1 and set 2.

Hence, there is only one process damping coefficient value estimated for each set of conditions. They are reasonably close to each other as summarized in Table 3.6. For the following sections, an average value of 2.25×10^5 N/m is used for AISI 1045 steel.

Table 3.6 : Identified process damping coefficient for AISI 1045 steel

	Quantity	Symbol	Size
Set 1	Process damping coefficient [N/m]	C_i	2.17×10^5
Set 2	Process damping coefficient [N/m]	C_i	2.33×10^5

3.6.2 Experimental Validation of Stability Chart

The prediction of the chatter stability chart, which demonstrates the stable and unstable cutting conditions, is presented in this section. Given the characteristic equation, the well known Nyquist stability criterion [52-54] is used for the prediction of the critically stable width of cut and corresponding spindle speed values. The method is briefly explained below. The characteristic equation in Eq.(3.38) can be written as:

$$CE(s) = 1 + H(s) = 0$$

where $H(s)$ is the open-loop transfer function. According to the Nyquist stability criterion, a closed loop system is stable if all the zeros of the characteristic equation are in the left half plane as:

$$Z = N + P = 0 \tag{3.43}$$

where

Z : number of zeros of $\left(1+H(s)\right)$ (poles of closed loop system) in the right-half plane.
N : net number of clockwise encirclements of $-1+0j$ point by the $H(j\omega)$ locus.
P : number of poles of the open-loop transfer function, $H(s)$ in the right half plane.

Poles of $H(s)$ are the poles of the structure, ($\phi_{pq}(s)$ see Eq.(3.27)) which are all stable (P = 0). Therefore any clockwise encirclement of $-1+0j$ point by the $H(j\omega)$ locus (or $0+0j$ point by the $CE(j\omega)$ locus) means an unstable pole of the system.

For the chatter stability chart, the Nyquist criterion is employed at every width of cut and spindle speed value, and the closed-loop system is checked to determine if it is stable or not. The process damping coefficient identified in the previous section is also included in the prediction. Chatter tests are conducted using cold rolled AISI 1045 steel and the tool is replaced with a new one without much wear. Test results are shown in Figure 3-24. Chatter is detected when the frequency content of the sound and force measurement have a high amplitude around the natural frequency of the structure. When the amplitude at the natural frequency is relatively small or comparable with the other frequencies, such as the spindle's rotational frequency, the cutting test is considered stable. The critically stable width of cut value is constant at 0.48 mm for all speed ranges when the process damping effect is neglected, which fails to predict chatter at low speeds. However, the cutting test results agree with the prediction of the critical stability at low speeds when the damping effect is included. Two samples of the sound measurements at low speed are shown in Figure 3-24 which represent stable and chatter cases. As the spindle speed increases, the effect of the process damping decreases and two stability curves converge. There are discrepancies between the predicted stability border and chatter tests after 3000 rpm spindle speed.

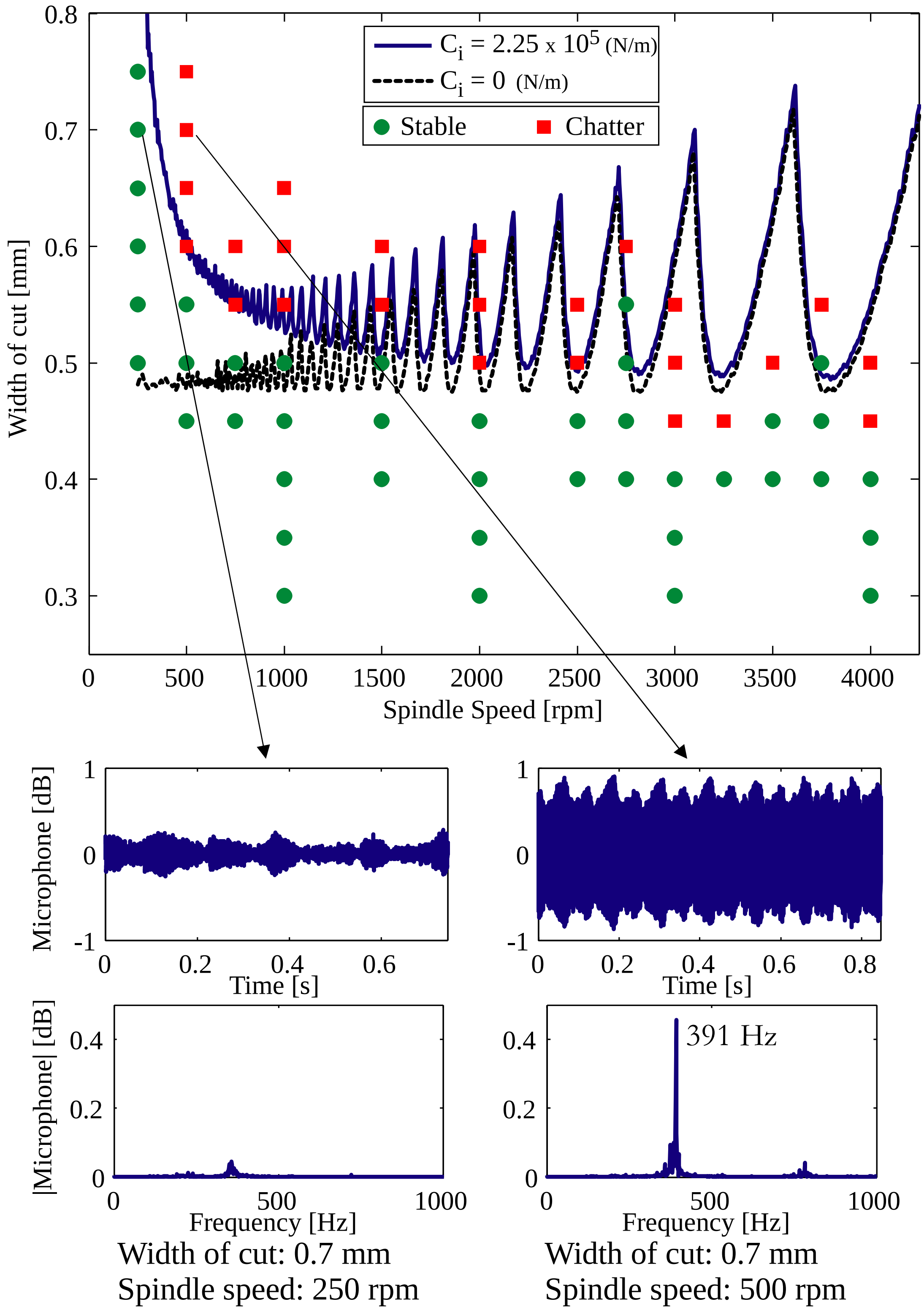

Figure 3-24 : Comparison of experimental results and the predicted chatter stability chart with two sample sound measurements at stable and unstable tests. Feed rate, c = 0.05 mm/rev, See Table 3.3 and Figure 3-17 for cutting coefficients and FRF measurements respectively.

The identified process damping coefficient for AISI 1045 (232 HB) is compared against the value identified with different methods in the literature. In this study C_i value is estimated as 2.25×10^5 N/m. Altintas and Eynian [27] implemented the in-phase sinusoidal excitation approach and identified the C_i value as 6.11×10^5 N/m for AISI 1045(210 HB). The experimental study carried out in [27] along with the stability borders predicted with the result of two identification methods are illustrated in Figure 3-25. Although some improvement is observed with several unstable tests at a width of cut of 1.0 and 1.2 with the new coefficient, there are still discrepancies at the spindle speed of 750 rpm and 1000 rpm.

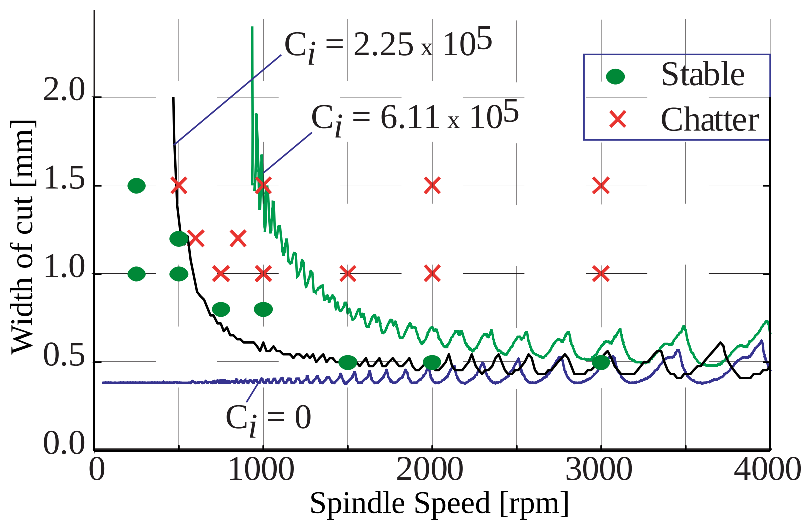

Figure 3-25 : Comparison of identified process damping coefficient with the one identified in [Altintas, 2008]. Structural parameters: m=0.561 kg, c=145 N/(m/s), k=6.48x10^6 N/m, cutting coefficients: $K_r = 1384$ Mpa, $K_t = 2580$ Mpa.

3.7 Summary

A process damping identification method is presented in this chapter. The method uses an approximate chip model which takes cutting parameters and tool geometry into account. Regeneration of the chip is assumed to be in the chip flow direction for the approximate chip model. The characteristic equation is derived for the dynamic plunge turning process including the regenerative chip thickness, speed dependent process damping effect, and all of the tool and workpiece flexibilities. Because the cutting velocity continuously changes in the plunge turning process, the critical cutting velocity at the transition from unstable to stable cutting is detected. The process damping coefficients are searched for around the chatter frequency. The detected coefficients are tested with the Nyquist stability criterion to verify if critical stability is reached. The value which satisfies the critical stability is the identified coefficient for process damping. The stability of the dynamic system is investigated by the Nyquist criterion and chatter tests are in good agreement with the predicted stability border.

Chapter 4

Stability of Line Boring Operation

4.1 Introduction

An automotive engine is composed of many stationary parts such as a cylinder block and head, as well as moving/rotating parts such as pistons, crankshaft and camshaft. The connection between stationary and rotating parts is carried through holes in the main blocks. The diameter and the length of the holes depend on the engine type but, in general, the length of the hole varies between L=10 to 600mm, whereas the diameter range is between D=5 to 90mm. After drilling the hole or directly after casting, the precision boring operation is applied to give the final diameter to the hole. Since the camshaft and crankshaft are very long, they are connected to the cylinder block and cylinder head through several bores, as illustrated in Figure 4-1. Half of the bore is on the main body of the engine, the other half is a separate component called the "crank bearing cap" and "cam bearing cap". The caps are mounted to the main blocks by means of bolts. Since the camshaft and crankshaft are two of the most critical mechanical parts of the engine, the quality of the camshaft and crankshaft bores is of the utmost importance. Especially, the crankshaft operates to transfer the power produced by the engine through the transmission and powertrain. Large forces are generated through the crankshaft, and bearings at the crankshaft bores carry the forces. Thus, crankshaft bores have tight tolerances considering the clearances necessary for the bearings and the concentricity of the axially spaced bores.

a-Cylinder Block **b- Cylinder Head**

Figure 4-1 : Main engine components: a) Cylinder block, b) Cylinder head

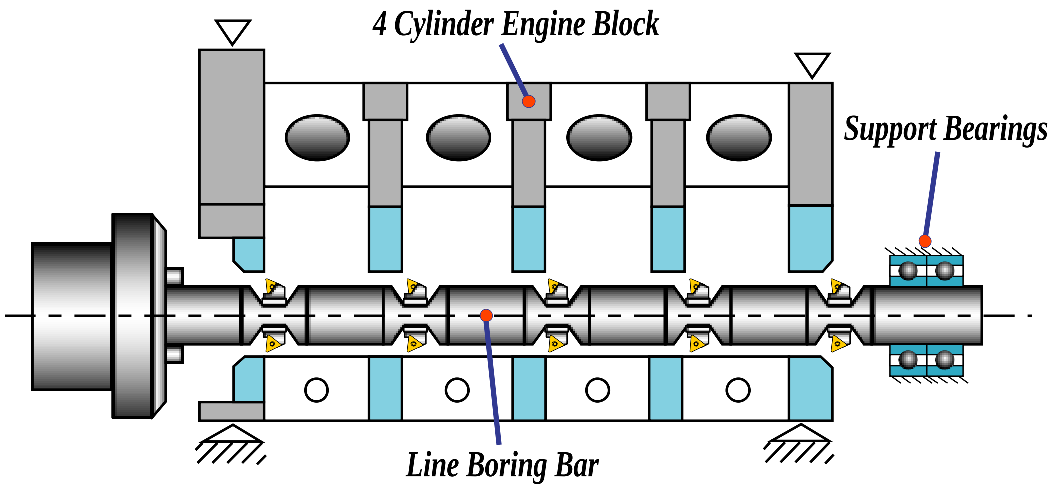

Figure 4-2: Application of line boring process; machining of crankshaft bores of a 4-cylinder engine

A special precision boring tool, called a line boring machine, is designed in order to machine the crankshaft and camshaft bores. This tool has a long bar on which there are as many axially spaced inserts as the number of bores to be machined. All of the bores are machined simultaneously with this tool, as shown in Figure 4-2. Various types of line boring tools are available, as well as customized designs for specific engines.

The machine tool designer must consider several criteria during the design stage. The first criterion is the high productivity in manufacturing where the designer must think about the number of inserts on the line boring bar, the machine down time for setup, and the tool change time for each machining operation. There are line boring tools which do semi-finishing and finishing in one stroke of machining to increase productivity. An example of that type is shown in Figure 4-3. The second criterion is the surface quality of the final hole. In this case, misalignment of the boring tool with respect to the engine block and the vibrations during cutting must be taken into account. It is quite possible to observe chatter marks on the surface because the boring bar is very long and flexible; the length and diameter (L/D) ratio lies between 5 and 20.

In this chapter, the dynamics of the line boring process is investigated in detail to predict the stable operating conditions. Various support conditions, as well as different insert configurations, are compared through simulations of the process.

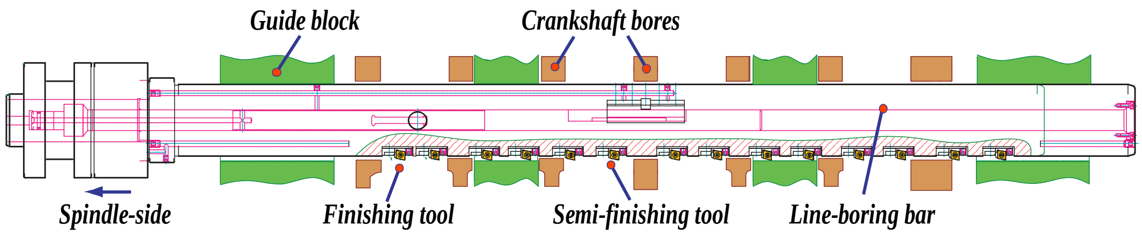

Figure 4-3 : Line boring bar for 6 cylinder engine block, supported by guide blocks

4.2 FE Modeling of Line Boring Bar

In order to study the dynamics of the line boring process, the structure of the line boring bar should be analyzed. When the shape of the line boring bar is considered, it does not differ much from a shaft having different diameters along its axis, see Figure 4-2. Some of them also have a hole through the rotation axis of the bar in order to reduce the weight, as shown in Figure 4-3.

In this study, the Finite Element Method (FEM) is applied to estimate the structural behaviour of the system. Since the line boring bar resembles a linear beam, it is considered a combination of beam elements having circular cross-sections. There are several beam models such as the Euler-Bernoulli beam and the Timoshenko beam theory. The former takes only the bending moment into account, whereas the latter additionally considers inertia coming from the rotation and the shear effect [55]. When the bar is long and thin (i.e. length/diameter (L/D) ratio is high), both of the theories give similar results for low frequency modes but the high frequency modes are different. As the L/D ratio decreases, the difference increases and the Euler-Bernoulli theory fails to estimate the natural frequencies accurately. This is due to the increased effect of the rotary inertia and shear deformation which are ignored in the Euler-Bernoulli beam theory at low L/D ratios. In the line boring application, the L/D ratio is high enough, however, the intention of this study is to develop a general model which can also be used for short boring heads where small L/D ratios exist. Hence the Timoshenko beam theory is applied throughout the rest of the thesis. The elemental mass ($\mathbf{M}_{elm}$) and stiffness ($\mathbf{K}_{elm}$) matrices for 6 degrees of freedom per node (dof/node) beam element are provided in Appendix A [56]. For the damping of the system, reasonable damping ratio (ζ) values are assumed for each mode within the range of 0.02 - 0.05.

Supporting conditions vary depending on the length of the bar. Usually, there is one support at the free end of the bar which is called the outboard support, see Figure 4-2. In addition to outboard support, there is inboard support placed between two ends of the bar to increase the rigidity of the structure. In order to introduce the effect of the support bearings on structural dynamics, the radial and axial spring elements are allowed in the Finite Element model at the corresponding nodes as shown in Figure 4-4a.

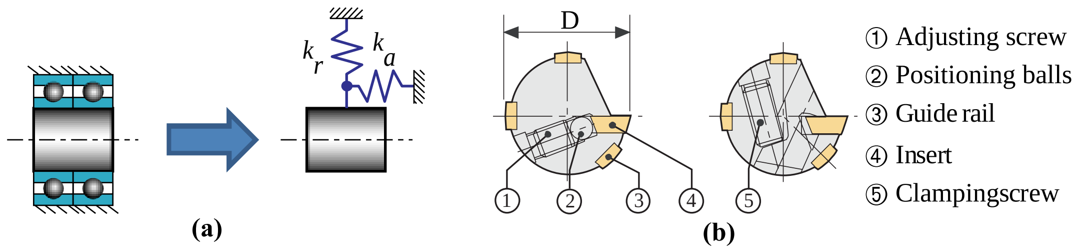

Figure 4-4 : (a) Representation of out-board and in-board support bearings as spring elements having radial and axial stiffness (b) Single insert line boring tool having guiding pads

In some applications, other than bearing elements, guide blocks are placed along the bar as a support component. In this case, the contact stiffness between the guide block and the boring bar should be known, so that it can be input into the Finite Element model. As an example, four guide blocks are used in the case shown in Figure 4-3. Furthermore, there are some types of line boring applications where there is only insert at the free end of the bar. The cutting operation starts with the first bore of the engine block, and one by one all of the bores are cut. In that case, the boring bar is supported by the previously machined bores with the help of guiding pads placed around the circumference of the boring bar, as shown in Figure 4-4b. The guiding pads have a slightly smaller diameter than the just machined bore. However, as discussed in [57], it is challenging to model the support conditions, because after the first bore it is not clear which guide pad is in contact with the bar during the cutting operation. In other words, the first machined bore is supporting the bar during the second bore cutting, but when the fourth bore is being cut, the second machined bore might not support the bar but only the first and third ones support. Given the dimensions, material properties and boundary conditions of the structure, the next step is the discretization of the boring bar into beam elements. After assembling each elemental matrix, global mass ($\mathbf{M}$) and stiffness ($\mathbf{K}$) matrices are obtained [58]. The natural frequencies (ω_n) and corresponding mode shapes ($\mathbf{u}$) are calculated by solving the eigenvalue problem of a free-undamped system which is given by:

$$\mathbf{K}\cdot\mathbf{u} = \omega^2\mathbf{M}\cdot\mathbf{u} \tag{4.1}$$

From a design point of view, the support conditions have a big effect on the mode shapes and the natural frequencies. To see this effect, mode shapes are plotted for 3 different supporting conditions. Dimensions and material properties of the tool are given in

Figure 4-13 and

Table 4-1 respectively. The overhang ratio (L/D) of the boring bar is 12 and the bar is discretized into 20 elements. The spindle side of the boring bar can be assumed as fixed by considering the high overhang ratio of the bar. The first case has fixed-free boundary conditions as shown in Figure 4-5, which does not have any real application because the structure is too flexible. It is presented here for comparison purposes. In this case, the first bending mode (at 97 Hz) is very dominant.

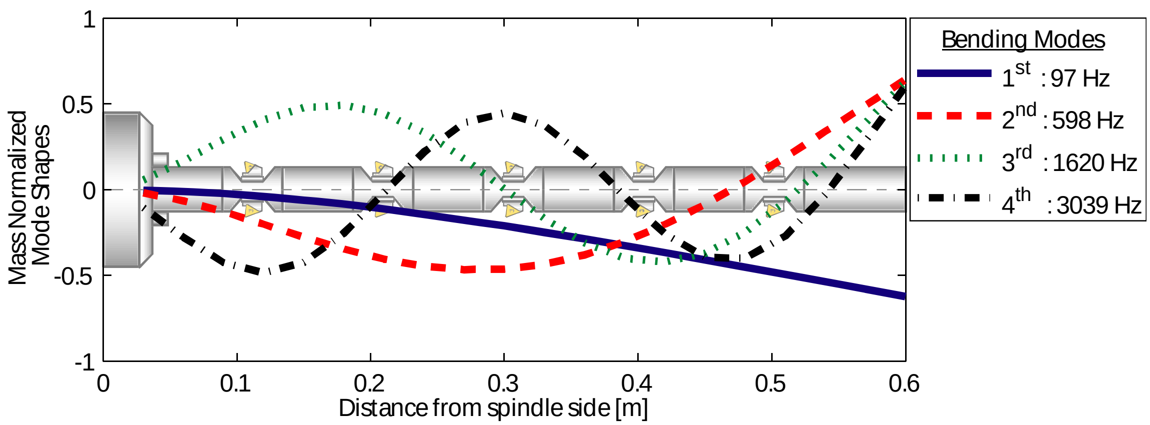

Figure 4-5 : First 4 mass normalized mode shapes of the line boring bar at fixed-free boundary conditions

The second case has outboard bearing support at the free end of the bar. The bearing is assumed to have only radial stiffness ($k_r = 3.85\times10^8 \, N/m, \quad k_a = 0$). The first bending mode (at 417 Hz) is still dominant, but the effect of the other modes is comparable. The mode shapes and corresponding natural frequencies are shown in Figure 4-6.

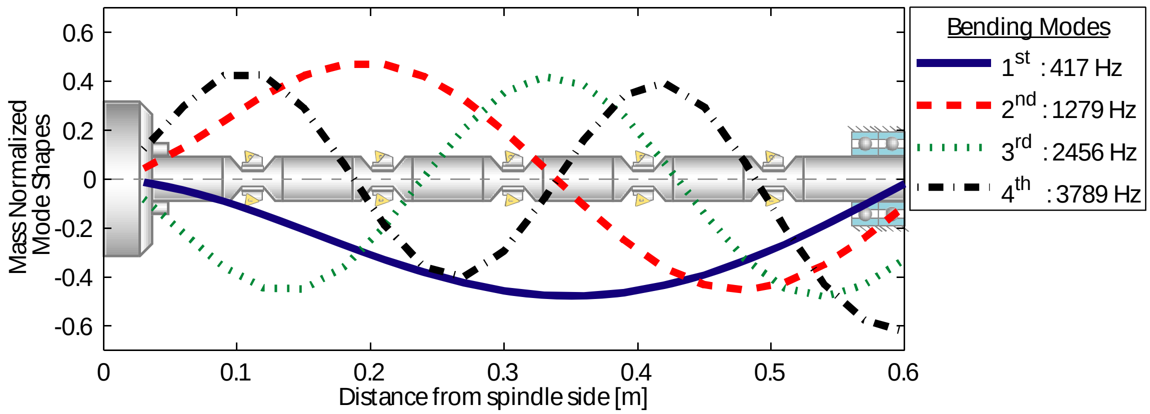

Figure 4-6 : First 4 mass normalized mode shapes of the line boring bar at fixed-outboard bearing boundary conditions

In addition to outboard support, inboard support having the same stiffness value is located in the middle of the boring bar in order to increase the rigidity of the structure. The influence of the inboard bearing is better observed in the first 2 bending modes (at 1074 and 1541 Hz), see Figure 4-7.

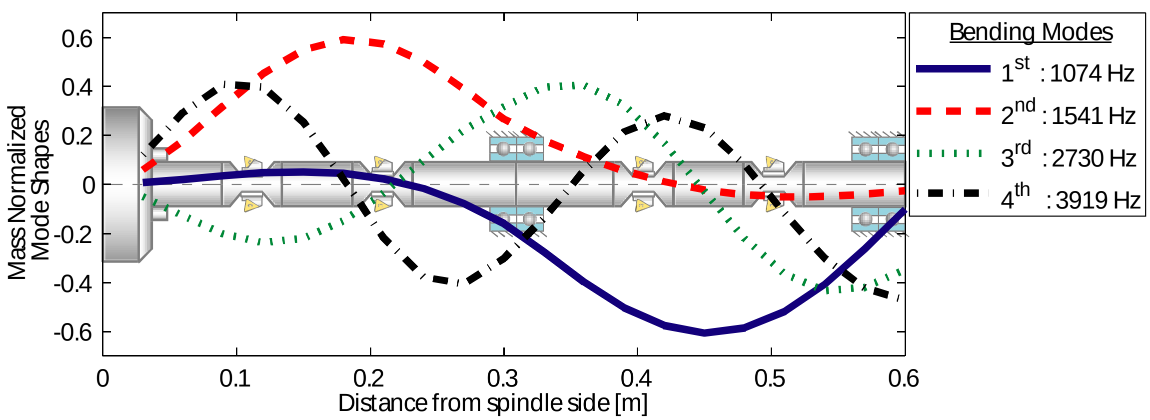

Figure 4-7 : First 4 mass normalized mode shapes of the line boring bar at fixed-inboard and outboard bearing boundary conditions

The result of FE modal analysis is used to obtain the force-displacement transfer function of the bar at the tool-workpiece interaction points which are then used for stability prediction in the following sections. The semi-discrete time domain method requires the natural frequency (ω_n), damping ratio (ζ_n) of each structural mode, and the modal matrix which is defined as $\mathbf{U} = [\mathbf{u}_1 \quad \cdots \quad \mathbf{u}_m]$ where m is the total number of modes considered in the analysis. In frequency domain analysis, the Frequency Response Function is obtained as [7], [59]:

$$\mathbf{\Phi}(\omega) = \sum_{k=1}^{m} \frac{\mathbf{u}_k \cdot \mathbf{u}_k^{\mathbf{T}}}{\omega_{n,k}^2 - \omega^2 + j2\zeta_k \omega_{n,k}\omega} \tag{4.2}$$

Regardless of the number of inserts along the bar, the transfer function remains constant as long as the same geometric dimensions and support conditions are considered.

Note that the spindle dynamics is also significant when the tool is not the most flexible component in a machine tool. The line boring bar is much more flexible than the spindle because it is very long. However, the proposed stability methods in the following sections are applicable and configurable to all of the boring types as well as short boring heads. Thus, one needs to consider the effect of spindle dynamics in those cases. Regardless of the type/length of the boring tool, if the machine is in-hand, the best way to obtain the transfer function is by measuring through modal testing. However, if the machine tool is not available during the design stage, an estimation of the transfer function is crucial for the design engineer.

4.3 Cutting Forces in Line Boring Process

The cutting forces are previously discussed in section 3.4.1 for single point cutting operations. In line boring operations, there are multiple inserts located radially and axially along the bar. As a result, all of the cutting forces must be taken into account. In addition to the forces, the torque created by the tangential cutting force is also included because the effect of the torsional vibrations is regarded as a source of the chip regeneration mechanism [60]. The general force model (as in Eq.(3.9)) including shearing, ploughing and process damping forces is written as:

$$\mathbf{F_{rta}} = \mathbf{K_c} \cdot A + \mathbf{K_e} \cdot L - \mathbf{P_d} \cdot \frac{C_i L}{V_c} \dot{r}(t) \tag{4.3}$$

where each vector is expressed as:

$$\begin{aligned}
\mathbf{F_{rta}} &= \{F_r \quad F_t \quad F_a \quad T\}^{\mathrm{T}} \\
\mathbf{K_c} &= \{K_{rc} \quad K_{tc} \quad K_{ac} \quad -R \cdot K_{tc}\}^{\mathrm{T}} \\
\mathbf{K_e} &= \{K_{re} \quad K_{te} \quad K_{ae} \quad -R \cdot K_{te}\}^{\mathrm{T}} \\
\mathbf{P_d} &= \{1 \quad \mu \quad 0 \quad -R\mu\}^{\mathrm{T}}
\end{aligned} \tag{4.4}$$

In Eq.(4.4), the torque created by the tangential forces is added as $T = -R \cdot F_t$, which is depicted in Figure 4-8b. The radial distance from the rotation axis to the tangential force is denoted by R. Note the minus sign comes from the direction of the torque that is in the opposite direction of the spindle rotation, which is considered as the positive direction. In order to cover different configurations of boring systems, a general model is used in this section. There are M number of inserts located axially on the boring bar and superscript i denotes the ith tool location ($i = 1, ..., M$). At each tool location, that is ith tool, there are N number of inserts radially spaced around the circumference of the bar and superscript j denotes the jth insert ($j = 1, ..., N$). Furthermore, three coordinate frames are introduced to express the forces and the displacements. The first one is the fixed machine coordinate system defined for each axially located tool (x^i, y^i, z^i, ϕ^i for ith tool in Figure 4-8a-b). The second one is the local coordinate frame defined for each insert radially spaced around the bar (x^j, y^j, z^j, ϕ^j for jth insert in Figure 4-8b-c). The local frame is rotating as the angular position (ϕ^j) of the insert changes. The third frame shows the direction of the cutting forces acting on each insert (r^j, t^j, a^j, ϕ^j for jth insert in Figure 4-8c-d). The force and displacement vector can be transferred between three coordinate frames by means of two transformation matrices. The first transformation matrix ($\mathbf{T_1}$) converts forces and displacements from (r^j, t^j, a^j, ϕ^j) the coordinate frame to the local tool coordinates (x^j, y^j, z^j, ϕ^j) of the jth insert as shown in Figure 4-8c.

$$\begin{aligned} \{x \quad y \quad z \quad \phi\}_j^{\mathbf{T}} &= \mathbf{T_1} \cdot \{r \quad t \quad a \quad \phi\}_j^{\mathbf{T}} \\ \underbrace{\{F_x \quad F_y \quad F_z \quad T_\phi\}_j^{\mathbf{T}}}_{\mathbf{F_j}} &= \mathbf{T_1} \cdot \underbrace{\{F_r \quad F_t \quad F_a \quad T_\phi\}_j^{\mathbf{T}}}_{\mathbf{F_{rta}}} \end{aligned} \tag{4.5}$$

where

$$\mathbf{T_1} = \begin{bmatrix} \cos(\kappa_r) & 0 & \sin(\kappa_r) & 0 \\ 0 & -1 & 0 & 0 \\ \sin(\kappa_r) & 0 & -\cos(\kappa_r) & 0 \\ 0 & 0 & 0 & 1 \end{bmatrix} \tag{4.6}$$

$\mathbf{T}_1$ changes with the approach angle κ_r. However, when the approximate chip model is applied, the approach angle is replaced by the flow angle (θ) as shown in Figure 4-8d. The parameters of the approximate chip are given in Eq.(3.15).

The second transformation matrix ($\mathbf{T}_2$) converts the corresponding vectors from the rotating local tool coordinate frame (x^j, y^j, z^j, ϕ^j) to the fixed machine coordinate system (x^i, y^i, z^i, ϕ^i) of the ith tool location as shown in Figure 4-8b.

$$\{x \quad y \quad z \quad \phi\}_i^{\mathbf{T}} = \mathbf{T_2} \cdot \{x \quad y \quad z \quad \phi\}_j^{\mathbf{T}} \tag{4.7}$$

where

$$\mathbf{T}_2 = \begin{bmatrix} \cos(\phi_j) & \sin(\phi_j) & 0 & 0 \\ -\sin(\phi_j) & \cos(\phi_j) & 0 & 0 \\ 0 & 0 & 1 & 0 \\ 0 & 0 & 0 & 1 \end{bmatrix} \tag{4.8}$$

$\mathbf{T}_2$ changes with the rotation of the bar as the instantaneous immersion angle (ϕ_j) of insert j varies, which is measured counter clockwise from normal x^i axis. As both of the transformation matrices have orthonormal columns, the inverse of them is equal to the transpose of them. Thus the inverse transformation is carried out as:

$$\begin{gathered} \{r \quad t \quad a \quad \phi\}_j^{\mathbf{T}} = \mathbf{T_1^T} \cdot \{x \quad y \quad z \quad \phi\}_j^{\mathbf{T}} \\ \{x \quad y \quad z \quad \phi\}_j^{\mathbf{T}} = \mathbf{T_2^T} \cdot \{x \quad y \quad z \quad \phi\}_i^{\mathbf{T}} \end{gathered} \tag{4.9}$$

The resultant force applied on ith tool is the summation of the forces created by all of the inserts radially spaced around the bar at the same axial location. After substituting Eq.(4.3) and Eq.(4.5), the resultant force acting on ith axial station becomes:

$$\begin{aligned}
\mathbf{F_i} &= \sum_{\mathbf{j}=1}^{N} \mathbf{T_2} \cdot \mathbf{F_j} \\
\mathbf{F_i} &= \sum_{\mathbf{j}=1}^{N} \mathbf{T_2} \cdot \left(\mathbf{T_1} \cdot \mathbf{F_{rta}} \right) \\
\mathbf{F_i} &= \sum_{\mathbf{j}=1}^{N} \mathbf{T_2} \cdot \mathbf{T_1} \cdot \left(\mathbf{K_c} \cdot A^j + \mathbf{K_e} \cdot L - \mathbf{P_d} \cdot \frac{C_i L}{V_c} \dot{r}^{\mathbf{j}}(t) \right) \\
\mathbf{F_i} &= \underbrace{\sum_{\mathbf{j}=1}^{N} \left(\mathbf{T_2} \cdot \mathbf{T_1} \cdot \mathbf{K_c} \cdot A^j \right)}_{\textbf{Shearing forces}} + \underbrace{\sum_{\mathbf{j}=1}^{N} \left(\mathbf{T_2} \cdot \mathbf{T_1} \cdot \mathbf{K_e} \cdot L \right)}_{\textbf{Edge forces}} - \underbrace{\sum_{\mathbf{j}=1}^{N} \left(\mathbf{T_2} \cdot \mathbf{T_1} \cdot \mathbf{P_d} \cdot \frac{C_i L}{V_c} \dot{r}^{\mathbf{j}}(t) \right)}_{\textbf{Process damping forces}}
\end{aligned} \tag{4.10}$$

When the spindle rotates at Ω (rad/s), the instantaneous immersion varies with time as $\phi_j = \Omega \cdot t$. The resultant force ($\mathbf{F_i}$) is time dependent, but periodic at the tooth period $\tau = 2\pi / N\Omega$.

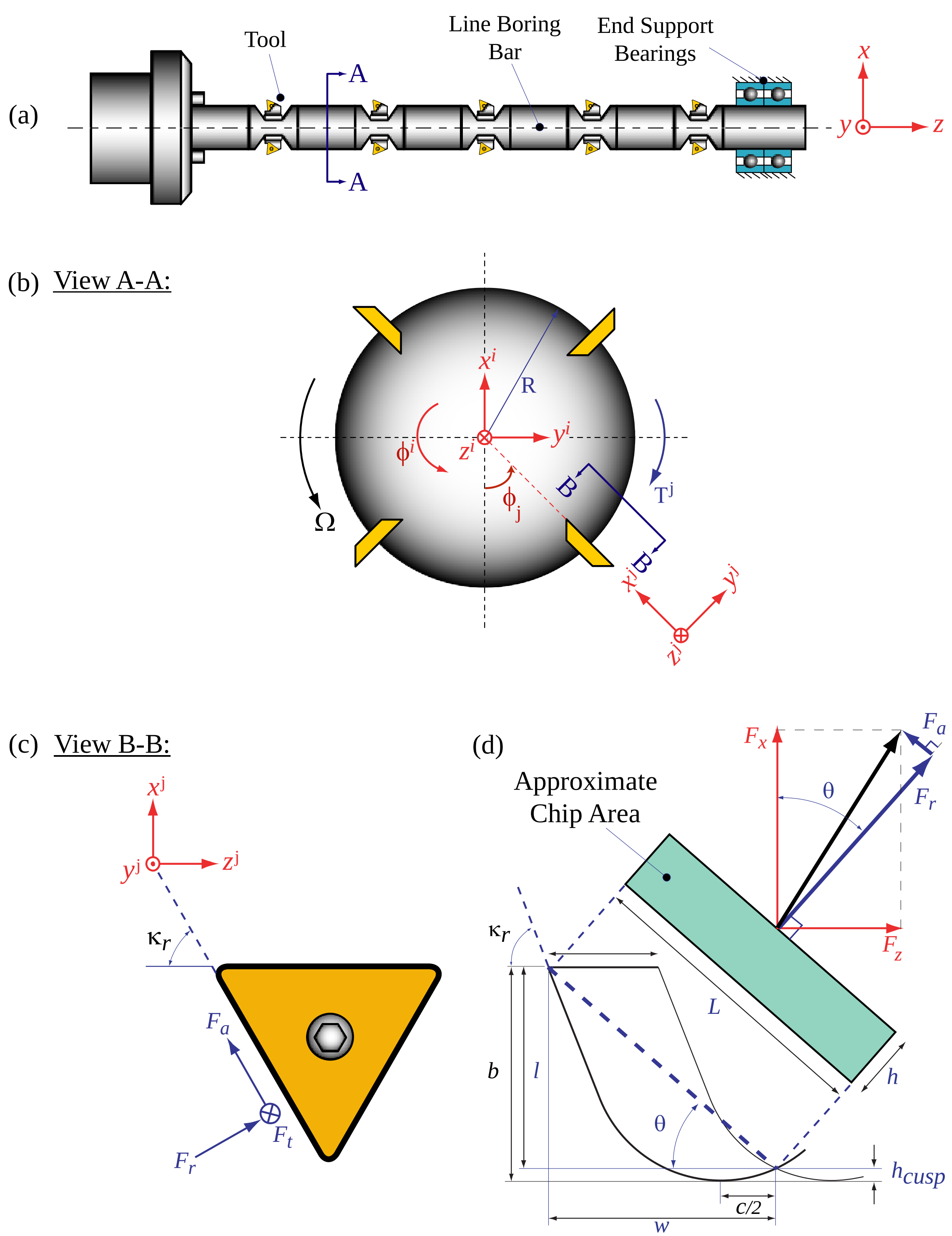

Figure 4-8 : (a) Schematic representation of line boring operation (b) Cross sectional view of ith node (view A-A) (c) Projected view of jth insert (view B-B) (d) Approximate chip model of jth insert

4.4 Stability Analysis of Line Boring in Frequency Domain

The cutting forces result in displacement of the line boring bar. The displacements make the chip thickness change at each tooth period of the boring bar. If unstable cutting conditions are selected, the displacements trigger the regeneration mechanism and result in chatter vibrations. In this section, stability of the line boring process is investigated with two analytical methods in frequency domain, namely the Zero Order Solution and the Nyquist Stability criterion.

4.4.1 Zero Order Solution

For stability analysis, the edge forces can be dropped from the general force model because they do not contribute to the chip regeneration mechanism. Furthermore, if the speed dependent process damping forces are neglected, the stability of the line boring operation can be predicted analytically in frequency domain. In other words, the critically stable width of cut values and corresponding spindle speeds can be derived explicitly as it is done for the milling operation similar to the theory presented in [10]. After applying the aforementioned simplifications, the force acting on the ith tool location (Eq.(4.10)) becomes as:

$$\mathbf{F_i} = \sum_{\mathbf{j}=1}^{N} \left(\mathbf{T_2} \cdot \mathbf{T_1} \cdot \mathbf{K_c} \cdot A^j \right) \tag{4.11}$$

The chip area (A^j) can be expressed by multiplication of the dynamic chip thickness and the edge length as:

$$A^j = \frac{b}{\sin(\kappa_r)} h_d^j \tag{4.12}$$

For the chip area, geometric nonlinearity arising from the nose radius is not included. When the approximate chip model is used, the linear stability model becomes dependent on the current width of cut which prevents the prediction of stable width of cuts explicitly.

The dynamic chip thickness (h_d^j) is modulated by the current vibrations and vibrations one tooth period earlier, as illustrated in Figure 4-9. The influence of vibrations in x^j and

z^j directions are also discussed in Chapter 3 and illustrated in Figure 4-9(a-b). In addition to them, torsional vibrations (ϕ^j) cause movements in the axial direction (z^j) which result in chip thickness variation, see Figure 4-9c. Thus, the dynamic chip becomes as:

$$h_d^j = c \cdot \sin(\kappa_r) - \Delta x^j \cos(\kappa_r) - \Delta z^j \sin(\kappa_r) - \Delta\phi^j \frac{c}{\phi_p} \sin(\kappa_r) \tag{4.13}$$

where $\Delta p = p(t) - p(t-\tau) \leftarrow p \in \{x^j, y^j, z^j, \phi^j\}$ and τ is the tooth passing period.

In Eq.(4.11), the $c \cdot \sin(\kappa_r)$ term represents the rigid body motion of the cutter. Since the rigid body motion affects only the static deflections and forced vibrations, but not stability, it is dropped from the dynamic chip thickness. Thus, dynamic chip for the j^{th} insert becomes:

$$h_d^j = \mathbf{T_3} \cdot \mathbf{\Delta p}^j \tag{4.14}$$

where

$$\begin{aligned} \mathbf{T_3} &= \left\{ -\cos(\kappa_r) \quad 0 \quad -\sin(\kappa_r) \quad -\frac{c}{\phi_p}\sin(\kappa_r) \right\} \\ \mathbf{\Delta p}^j &= \left\{ \Delta x^j \quad \Delta y^j \quad \Delta z^j \quad \Delta\phi^j \right\}^{\mathbf{T}} \end{aligned} \tag{4.15}$$

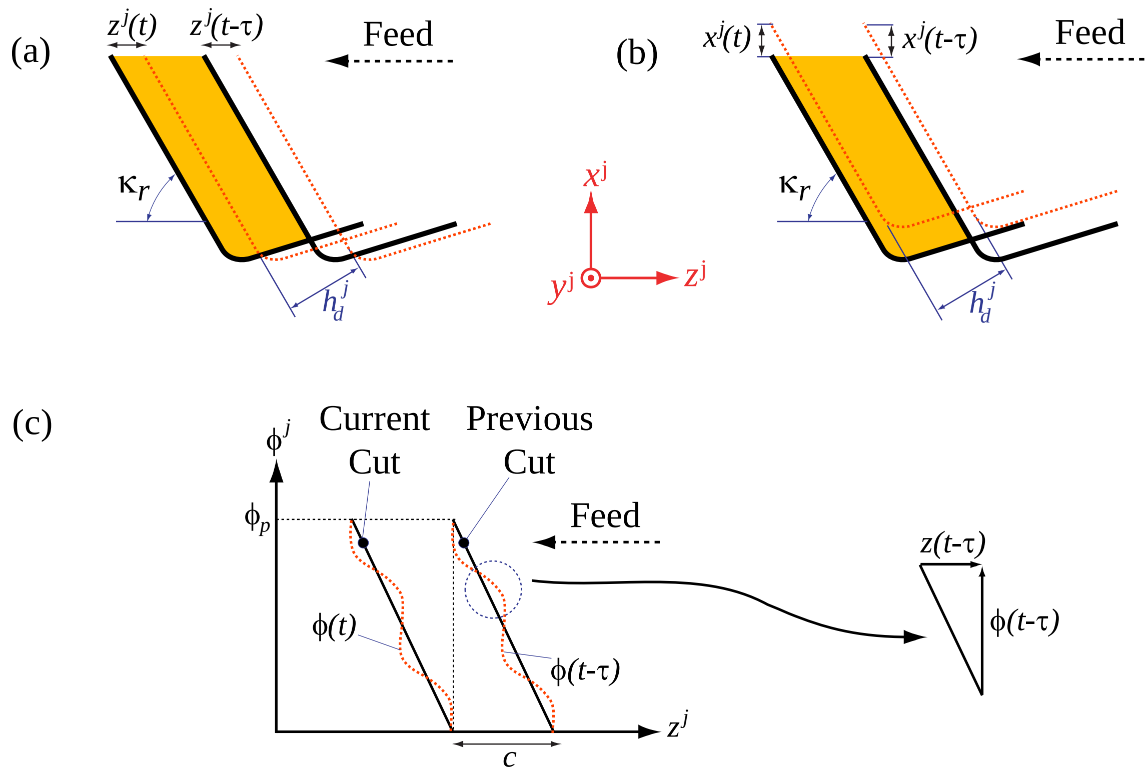

Figure 4-9 : Variation of chip thickness with (a) vibrations in x^j direction (b) vibrations in z^j (c) torsional vibrations (ϕ^j)

Substituting the chip thickness and the chip area into the force model, Eq.(4.11), yields:

$$\mathbf{F_i} = \sum_{\mathbf{j}=1}^{N} \left(\mathbf{T_2} \cdot \mathbf{T_1} \cdot \mathbf{K_c} \cdot \frac{b}{\sin(\kappa_r)} \cdot \mathbf{T_3} \cdot \mathbf{\Delta p}^j \right) \tag{4.16}$$

Equation (4.16) shows the displacements ($\mathbf{\Delta p}^j$) in rotating coordinates of the jth insert. Inverse transformation ($\mathbf{T_2^T}$) can be used to express them in fixed machine coordinates where the frequency response of the flexible system is obtained. Thus, the dynamic force acting on the ith tool location becomes:

$$\begin{aligned} \mathbf{F_i} &= \sum_{\mathbf{j}=1}^{N} \left(\mathbf{T_2} \cdot \mathbf{T_1} \cdot \mathbf{K_c} \cdot \frac{b}{\sin(\kappa_r)} \cdot \mathbf{T_3} \cdot \mathbf{T_2^T} \cdot \mathbf{\Delta p}^i \right) \\ \mathbf{F_i} &= b \cdot \mathbf{A}_i(\phi) \cdot \mathbf{\Delta p}^i \end{aligned} \tag{4.17}$$

where $\mathbf{A}(\phi)$ is called the directional coefficient matrix:

$$\mathbf{A}_i(\phi) = \sum_{\mathrm{j}=1}^{N} \left(\mathbf{T}_2 \cdot \mathbf{T}_1 \cdot \boldsymbol{K}_c \cdot \frac{1}{\sin(\kappa_r)} \cdot \mathbf{T}_3 \cdot \mathbf{T}_2^{\mathrm{T}} \right)$$
$$\mathbf{A}_i(\phi) = \begin{bmatrix} a_{xx} & a_{xy} & a_{xz} & a_{x\phi} \\ a_{yx} & a_{yy} & a_{yz} & a_{y\phi} \\ a_{zx} & a_{zy} & a_{zz} & a_{z\phi} \\ a_{\phi x} & a_{\phi y} & a_{\phi z} & a_{\phi\phi} \end{bmatrix} \tag{4.18}$$

The variation of the elements of $\mathbf{A}_i(\phi)$ with respect to the angular position of insert (ϕ) is given in Figure 4-10 and Figure 4-11. When the number of radially located inserts is one or two ($N=1,2$), most of the coefficients in $\mathbf{A}_i(\phi)$ vary periodically with the angular position, see Figure 4-10 for $N=1$. However, for all insert numbers greater than two, the coefficients are constant, i.e. independent of the immersion angle, see Figure 4-11 for $N=5$.

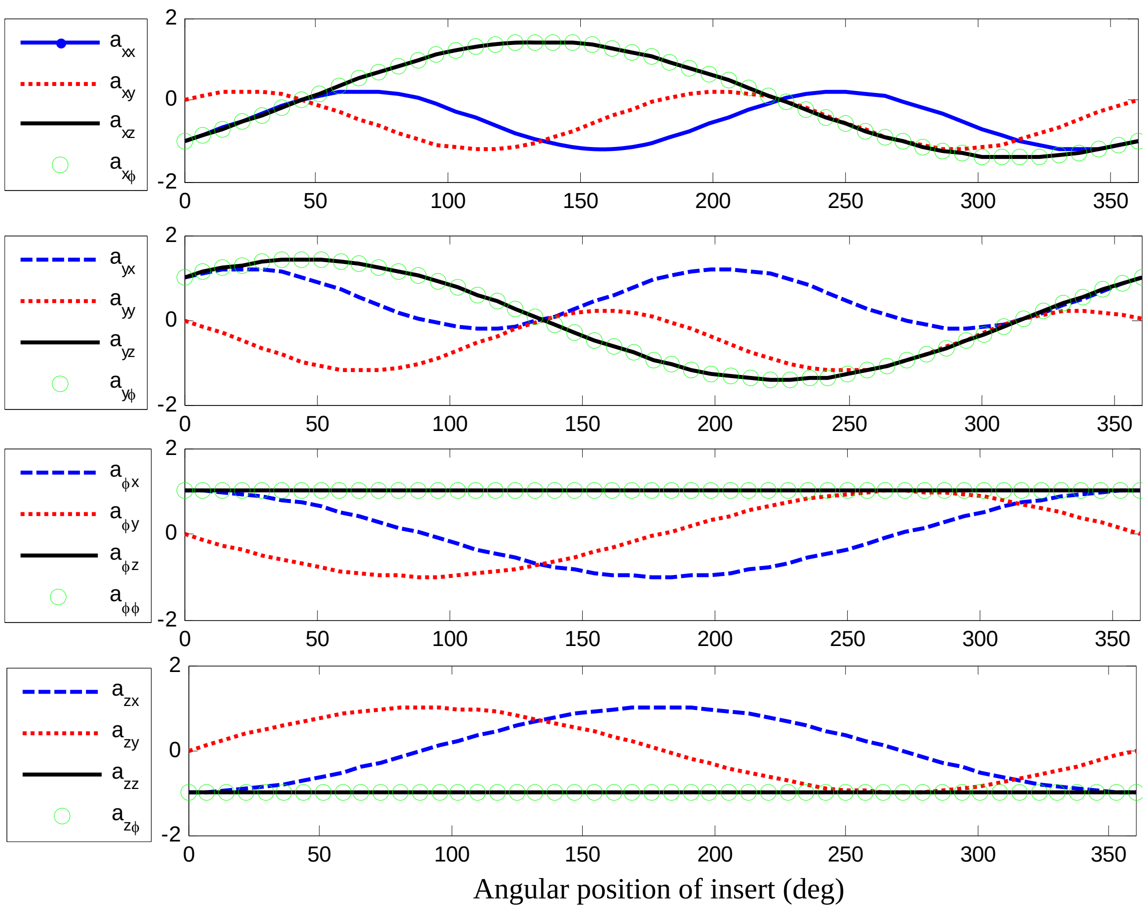

Figure 4-10 : Variation of directional coefficients with angular position of 1 insert (N=1)

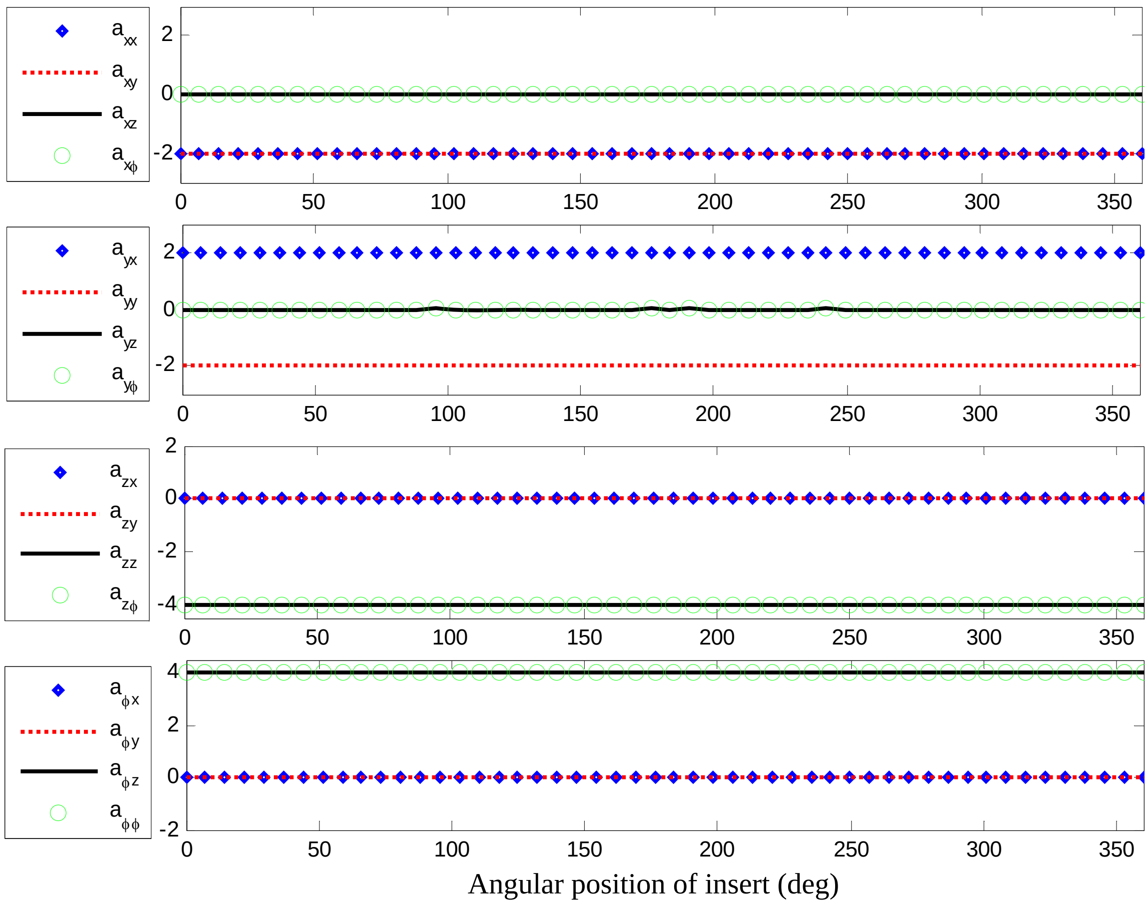

Figure 4-11 : Variation of directional coefficients with angular position of insert when 5 inserts are used around the periphery of the bar at fixed location (N=5)

Budak [10] presented a stability solution when varying directional coefficients are present. Altintas [61] proved that unless the cutting process is highly intermittent, the average of the directional coefficients leads to as accurate stability solution as the case when varying directional terms are considered. In the line boring case, when insert number (N) is greater than two, the directional terms are constant, so taking the average does not introduce any approximation. If there are only 1 or 2 inserts, taking the average still does not influence the stability of the process because the cutting operation is continuous, and directional terms do not have short impulse-wave forms where strong harmonic components are present in addition to the average value. Thus, the average component of $\mathbf{A}_i(\phi)$ becomes:

$$\mathbf{A}_{0i} = \frac{1}{\tau}\int_0^{\tau} \mathbf{A}_i(t)dt = \frac{1}{2\pi}\int_{\phi=0}^{\phi=2\pi} \mathbf{A}_i(\phi)d\phi = \frac{N}{2}\begin{bmatrix} \alpha_{xx} & \alpha_{xy} & \alpha_{xz} & \alpha_{x\phi} \\ \alpha_{yx} & \alpha_{yy} & \alpha_{yz} & \alpha_{y\phi} \\ \alpha_{zx} & \alpha_{zy} & \alpha_{zz} & \alpha_{z\phi} \\ \alpha_{\phi x} & \alpha_{\phi y} & \alpha_{\phi z} & \alpha_{\phi\phi} \end{bmatrix} \tag{4.19}$$

where α terms are:

$$\begin{aligned}
&\alpha_{xx} = \alpha_{yy} = -K_{rc}\cos(\kappa_r)\cot(\kappa_r) - K_{ac}\cos(\kappa_r) \\
&\alpha_{xy} = -K_{tc}\cot(\kappa_r), \qquad \alpha_{yx} = -\alpha_{xy} \\
&\alpha_{zz} = 2K_{ac}\cos(\kappa_r) - 2K_{rc}\sin(\kappa_r) \\
&\alpha_{z\phi} = \frac{2c}{\phi_p}\cdot\alpha_{zz}, \qquad \alpha_{\phi z} = 2K_{tc}R \\
&\alpha_{\phi\phi} = \frac{2c}{\phi_p}\cdot\alpha_{\phi z}, \\
&\alpha_{xz} = \alpha_{x\phi} = \alpha_{yz} = \alpha_{y\phi} = \alpha_{zx} = \alpha_{zy} = \alpha_{\phi x} = \alpha_{\phi y} = 0
\end{aligned} \tag{4.20}$$

For more than two inserts ($N > 2$), taking the average yields the exact solution because the directional terms are time invariant, i.e. $\mathbf{A}_{0i} = \mathbf{A}_i(\phi)$. Analytical proof of time invariant directional terms is given in Appendix C. For the line boring operation where the tool is always in contact, the entry and exit angles are 0 and 2π, respectively. In the case of different entry and exit angles, the proposed Zero Order Solution is still capable of predicting stability, but average terms must be calculated by integrating $\mathbf{A}_i(\phi)$ over the spindle period 2π again, including a windowing function as explained in [10]. Here, care must be taken because the more interrupted the cutting operation is, the more approximation is introduced by averaging the directional terms.

The displacement vector ($\Delta\mathbf{p}^i$), given in Eq.(4.17), represents the relative movement of the tool with respect to the workpiece. Displacements are written for insert i in fixed coordinate frame as:

$$\Delta\mathbf{p}^i = \mathbf{p}^i(t) - \mathbf{p}_0^i(t-\tau) \tag{4.21}$$

where vibrations at the present time (t) and previous tooth period ($t-\tau$) are defined as:

$$\begin{aligned}\mathbf{p}^i(t) &= \{x(t) \quad y(t) \quad z(t) \quad \phi(t)\}_i^{\mathbf{T}} \\ \mathbf{p}_0^i(t-\tau) &= \{x(t-\tau) \quad y(t-\tau) \quad z(t-\tau) \quad \phi(t-\tau)\}_i^{\mathbf{T}}\end{aligned} \tag{4.22}$$

Vibrations can be described at chatter frequency ω_c by using the Frequency Response Function (FRF) of the structure:

$$\begin{aligned}\mathbf{p}^i(\mathbf{i}\omega_c) &= \{\mathbf{H}_{i1} \quad \cdots \quad \mathbf{H}_{ii} \quad \cdots \quad \mathbf{H}_{iM}\} \cdot \begin{Bmatrix}\mathbf{F}_1 \\ \vdots \\ \mathbf{F}_i \\ \vdots \\ \mathbf{F}_M\end{Bmatrix} \cdot e^{-\mathbf{i}\omega_c t} \\ \mathbf{p}_0^i(\mathbf{i}\omega_c) &= \mathbf{p}^i(\mathbf{i}\omega_c) \cdot e^{-\mathbf{i}\omega_c \tau}\end{aligned} \tag{4.23}$$

where

$$\begin{aligned}\boldsymbol{H}_{ab} &= \begin{bmatrix}\phi_{xx} & \phi_{xy} & \phi_{xz} & \phi_{x\phi} \\ \phi_{yx} & \phi_{yy} & \phi_{yz} & \phi_{y\phi} \\ \phi_{zx} & \phi_{zy} & \phi_{zz} & \phi_{z\phi} \\ \phi_{\phi x} & \phi_{\phi y} & \phi_{\phi z} & \phi_{\phi\phi}\end{bmatrix}_{ab} \leftarrow a,b \in \{1,\ldots,M\} \\ \mathbf{F}_i &= \{F_x \quad F_y \quad F_z \quad T_\phi\}_i^{\mathbf{T}} \;\; and \;\; \mathbf{i} = \sqrt{-1}\end{aligned} \tag{4.24}$$

$\omega_c \tau$ is the phase delay between vibrations at successive tooth periods. Combining Eq.(4.17),(4.19),(4.21) and (4.23), the cutting force vector $\mathbf{F}_i$ for each axially spaced insert (i^{th} insert) can be expressed as:

$$\mathbf{F}_i \cdot e^{-\mathbf{i}\omega_c t} = b \cdot \left(1 - e^{-\mathbf{i}\omega_c \tau}\right) \cdot \mathbf{A}_{\mathbf{0}i} \cdot \{\mathbf{H}_{i1} \quad \cdots \quad \mathbf{H}_{ii} \quad \cdots \quad \mathbf{H}_{iM}\} \cdot \begin{Bmatrix}\mathbf{F}_1 \\ \vdots \\ \mathbf{F}_i \\ \vdots \\ \mathbf{F}_M\end{Bmatrix} \cdot e^{-\mathbf{i}\omega_c t} \tag{4.25}$$

All of the cutting force vectors can be written in an augmented matrix format as:

$$\begin{Bmatrix} \mathbf{F}_1 \\ \vdots \\ \mathbf{F}_i \\ \vdots \\ \mathbf{F}_M \end{Bmatrix} \cdot e^{-\mathbf{i}\omega_c t} = b\cdot\left(1-e^{-\mathbf{i}\omega_c\tau}\right)\cdot \underbrace{\begin{bmatrix} \mathbf{A}_{01} & \mathbf{0} & \cdots & \mathbf{0} & \mathbf{0} \\ \vdots & \ddots & & & \vdots \\ \mathbf{0} & \cdots & \mathbf{A}_{0i} & \cdots & \mathbf{0} \\ \vdots & & & \ddots & \vdots \\ \mathbf{0} & \mathbf{0} & \cdots & \mathbf{0} & \mathbf{A}_{0M} \end{bmatrix}}_{[\mathbf{DCM}]} \cdot \underbrace{\begin{bmatrix} \mathbf{H}_{11} & & \cdots & & \mathbf{H}_{1M} \\ \vdots & \ddots & & & \vdots \\ \mathbf{H}_{i1} & \cdots & \mathbf{H}_{ii} & \cdots & \mathbf{H}_{iM} \\ \vdots & & & \ddots & \vdots \\ \mathbf{H}_{M1} & & \cdots & & \mathbf{H}_{MM} \end{bmatrix}}_{\mathbf{\Phi}} \cdot \underbrace{\begin{Bmatrix} \mathbf{F}_1 \\ \vdots \\ \mathbf{F}_i \\ \vdots \\ \mathbf{F}_M \end{Bmatrix}}_{\mathbf{F}} \cdot e^{-\mathbf{i}\omega_c t} \tag{4.26}$$

which turns the dynamic boring system to an eigenvalue problem:

$$\det\left[\mathbf{I} + \Lambda\cdot[\mathbf{DCM}]\cdot\mathbf{\Phi}\right] = 0 \tag{4.27}$$

where the complex eigenvalue is,

$$\Lambda = -b\cdot\left(1-e^{-\mathbf{i}\omega_c\tau}\right) = \Lambda_R + \mathbf{i}\Lambda_I \tag{4.28}$$

where Λ_R and Λ_I are the real and imaginary parts of the eigenvalue Λ. The number of eigenvalues is the same as the size of the overall directional coefficient matrix $[\mathbf{DCM}]$. Since the size is greater than two in most of the cases, it is not possible to find an explicit analytical expression for eigenvalues as in [10]. Instead, they are solved numerically for a given chatter frequency ω_c. Once the eigenvalues are calculated numerically, the critical width of cut, $b_{\lim}$, values are calculated by substituting $e^{-\mathbf{i}\omega_c\tau} = \cos(\omega_c\tau) - \mathbf{i}\sin(\omega_c\tau)$ into Eq.(4.28) as:

$$b_{\lim} = -\frac{1}{2}\left(\frac{\Lambda_I\sin(\omega_c\tau) + \Lambda_R(1-\cos(\omega_c\tau))}{1-\cos(\omega_c\tau)} + \mathbf{i}\,\frac{\Lambda_I(1-\cos(\omega_c\tau)) - \Lambda_R\sin(\omega_c\tau)}{1-\cos(\omega_c\tau)}\right) \tag{4.29}$$

However, the width of cut is a physical quantity and must be a real number. As a result, the imaginary part of $b_{\lim}$ in Eq.(4.29) must be zero,

$$\Lambda_I(1-\cos(\omega_c\tau)) - \Lambda_R\sin(\omega_c\tau) = 0 \tag{4.30}$$

By assigning a variable κ for the ratio of Λ_I to Λ_R and substituting κ into Eq.(4.29), the critical width of cut value can be found explicitly as:

$$b_{\lim} = -\frac{1}{2}\Lambda_R\left(\kappa^2+1\right) \tag{4.31}$$

where

$$\kappa = \frac{\Lambda_I}{\Lambda_R} = \frac{\sin(\omega_c\tau)}{1-\cos(\omega_c\tau)} \tag{4.32}$$

Eq.(4.32) is rewritten by implementing the half angle conversions:

$$\kappa = \frac{\cos(\omega_c\tau/2)}{\sin(\omega_c\tau/2)} = \tan(\pi/2-\omega_c\tau/2) \tag{4.33}$$

Taking the inverse of both sides of Eq.(4.33):

$$\psi = \arctan(\kappa) = \frac{\pi}{2}-\frac{\omega_c\tau}{2}+n\pi \qquad \text{where} \qquad n\in\mathbb{Z} \tag{4.34}$$

On the other hand, the total number of vibration cycles can be divided into two components. The first component k is the number of full vibration cycles. The second component is a fraction of a full cycle, ε, which actually implies the phase shift between the current and previous vibration marks resulting in the regeneration of the chip:

$$\omega_c\tau = 2k\pi+\varepsilon \quad \text{where} \quad k\in\mathbb{N}_0 \tag{4.35}$$

provided that the below condition is satisfied.

$$0\le\varepsilon<2\pi \tag{4.36}$$

When Eq.(4.35) is substituted into Eq.(4.34), ε is extracted as:

$$\varepsilon = 2\pi(n-k)+\pi-2\psi \tag{4.37}$$

Special care must be taken when calculating the inverse tangent in Eq.(4.34) with digital computers. When *atan* function (defined as $-\pi/2<\mathrm{atan}(\Lambda_I/\Lambda_R)<\pi/2$) is utilized for this purpose, in order to satisfy the condition given in Eq.(4.36), $(n-k)$ must be zero, thus the phase shift becomes:

$$\varepsilon = \pi - 2\,\mathrm{atan}\left(\frac{\Lambda_I}{\Lambda_R}\right) \tag{4.38}$$

For each critical width of cut value calculated with Eq.(4.31), the corresponding spindle speed $n\ (\mathrm{rev/min})$ for each stability lobe ($k = 0,1,..$) is calculated as:

$$\tau = \frac{2k\pi + \varepsilon}{\omega_c} \quad \rightarrow \quad n = \frac{60}{N\tau} \tag{4.39}$$

The above explained zero order stability solution usually results in as many stability lobes as the number of eigenvalues having a negative real part. However, when stable cutting conditions are of interest, the region below the critical stability border must be used after superimposing all of the lobes.

4.4.2 Stability Using Nyquist Criterion with Process Damping

The effect of process damping on stability is investigated in this section. Since the process damping forces in Eq.(4.3) depend on the cutting speed, the stable spindle speeds cannot be calculated explicitly unlike the zero order solution. However, the stability is checked by the Nyquist criterion at each spindle speed and width of cut pair. The chatter stability chart is obtained by scanning a range of spindle speeds.

The Zero Order Solution is not able to take full chip geometry into account because of the geometric nonlinearity introduced by the nose radius. However, when the process damping force exists in the force model, the stability of the system is checked at each operating condition which allows the use of the approximate chip model. Thus, the approximate chip model shown in Figure 4-8 is implemented in this section. Details of the approximate chip model are provided in section 3.4.1.

The cutting forces applied to each bore location ($\mathbf{F_i}$) in Eq.(4.10) are rewritten below:

$$\mathbf{F_i} = \underbrace{\sum_{\mathbf{j}=1}^{N}\left(\mathbf{T_2}\cdot\mathbf{T_1}\cdot\mathbf{K_c}\cdot A^j\right)}_{\textbf{Shearing forces}} + \underbrace{\sum_{\mathbf{j}=1}^{N}\left(\mathbf{T_2}\cdot\mathbf{T_1}\cdot\mathbf{K_e}\cdot L\right)}_{\textbf{Edge forces}} - \underbrace{\sum_{\mathbf{j}=1}^{N}\left(\mathbf{T_2}\cdot\mathbf{T_1}\cdot\mathbf{P_d}\cdot\frac{C_i L}{V_c}\dot{r}^{\mathbf{j}}(t)\right)}_{\textbf{Process damping forces}}$$

The edge forces can be dropped because they do not affect the stability of the system:

$$\mathbf{F_i} = \sum_{\mathbf{j}=1}^{N}\left(\mathbf{T_2}\cdot\mathbf{T_1}\cdot\mathbf{K_c}\cdot A^j\right) - \sum_{\mathbf{j}=1}^{N}\left(\mathbf{T_2}\cdot\mathbf{T_1}\cdot\mathbf{P_d}\cdot\frac{C_i L}{V_c}\dot{r}^{\mathbf{j}}(t)\right) \tag{4.40}$$

Where the $\mathbf{T_1}$ transformation matrix is a function of the chord angle (θ). The chord length (L), chord angle (θ) and equivalent chip thickness (h) are shown in Figure 4-8 and calculated in Eq.(3.15). Substituting the dynamic chip thickness (h_d^j as in Eq.(4.14)), the chip area of each insert (A^j) is expressed in terms of displacements ($\mathbf{p}^i(t)$, $\mathbf{p}_0^i(t-\tau)$ in Eq.(4.22)) in the fixed coordinate system as:

$$\begin{aligned} A^j &= L\cdot h_d^j \\ &= L\cdot\mathbf{T_3}\cdot\mathbf{\Delta p}^j \qquad\qquad \text{where } \mathbf{T_3} = f(\theta) \\ &= L\cdot\mathbf{T_3}\cdot\mathbf{T_2^T}\cdot\left(\mathbf{p}^i(t)-\mathbf{p}_0^i(t-\tau)\right) \end{aligned} \tag{4.41}$$

Moreover, $\dot{r}^{\mathbf{j}}(t)$ term in the process damping force in Eq.(4.40) is transformed into the fixed frame as:

$$\begin{aligned} \dot{r}^{\mathbf{j}}(t) &= \mathbf{T_4}\cdot\dot{\mathbf{p}}^j(t) \\ &= \mathbf{T_4}\cdot\mathbf{T_2^T}\cdot\dot{\mathbf{p}}^i(t) \end{aligned} \tag{4.42}$$

where $\mathbf{T}_4$ is defined as:

$$\mathbf{T_4} = \left\{\cos(\theta) \quad 0 \quad \sin(\theta) \quad \frac{c}{\phi_p}\sin(\theta)\right\} \tag{4.43}$$

By substituting Eq.(4.41) and Eq.(4.42) into Eq.(4.40), the dynamic force vector becomes:

$$\mathbf{F_i} = \mathbf{J}^i\cdot\mathbf{p}^i(t) + \mathbf{J}_{\boldsymbol{\tau}}^i\cdot\mathbf{p}_0^i(t-\tau) + \mathbf{J}_{\mathbf{v}}^i\cdot\dot{\mathbf{p}}^i(t) \tag{4.44}$$

where direct ($\mathbf{J}^i$), delay ($\mathbf{J}_{\boldsymbol{\tau}}^i$), and process damping ($\mathbf{J}_{\mathbf{v}}^i$) gain matrices are:

$$\begin{aligned} \mathbf{J}^i &= \sum_{\mathbf{j}=1}^{N}\left(\mathbf{T_2}\cdot\mathbf{T_1}\cdot\mathbf{K_c}\cdot L\cdot\mathbf{T_3}\cdot\mathbf{T_2^T}\right) \\ \mathbf{J}_{\boldsymbol{\tau}}^i &= -\mathbf{J}^i \\ \mathbf{J}_{\mathbf{v}}^i &= -\sum_{\mathbf{j}=1}^{N}\left(\mathbf{T_2}\cdot\mathbf{T_1}\cdot\mathbf{P_d}\cdot\frac{C_i L}{V_c}\cdot\mathbf{T_4}\cdot\mathbf{T_2^T}\right) \end{aligned} \tag{4.45}$$

Similar to the directional coefficient matrix ($\mathbf{A}_i(\phi)$ as in Eq.(4.18)), process gain matrices are time-variant and periodic at the tooth passing period (τ) because $\mathbf{T_2}$ is a function of the rotation angle (ϕ). In order to investigate the stability, the average of each matrix is calculated which makes the dynamic line boring system time-invariant. The average direct and delay gain matrices ($\overline{\mathbf{J}}^i$, $\overline{\mathbf{J}}^i_{\boldsymbol{\tau}}$) are:

$$\overline{\mathbf{J}}^i = \frac{1}{2\pi}\cdot\int_{\phi=0}^{\phi=2\pi}\mathbf{J}^i(\phi)d\phi = L\cdot\frac{N}{2}\cdot\begin{bmatrix}\alpha_{xx} & \alpha_{xy} & 0 & 0\\ \alpha_{yx} & \alpha_{yy} & 0 & 0\\ 0 & 0 & 2\alpha_{zz} & 2\alpha_{z\phi}\\ 0 & 0 & 2\alpha_{\phi z} & 2\alpha_{\phi\phi}\end{bmatrix} \tag{4.46}$$

$$\overline{\mathbf{J}}^i_{\boldsymbol{\tau}} = -\overline{\mathbf{J}}^i$$

where

$$\begin{aligned}
\alpha_{xx} &= \alpha_{yy} = -K_{rc}\cos^2(\theta) - K_{ac}\sin(\theta)\cos(\theta)\\
\alpha_{xy} &= -K_{tc}\cos(\theta), \qquad \alpha_{yx} = -\alpha_{xy}\\
\alpha_{zz} &= K_{ac}\sin(\theta)\cos(\theta) - K_{rc}\sin^2(\theta)\\
\alpha_{z\phi} &= \frac{c}{\phi_p}\cdot\alpha_{zz}\\
\alpha_{\phi z} &= K_{tc}R\sin(\theta)\\
\alpha_{\phi\phi} &= \frac{c}{\phi_p}\cdot\alpha_{\phi z}
\end{aligned} \tag{4.47}$$

Similarly, the average of the process damping gain matrix ($\overline{\mathbf{J}}^i_{\mathbf{v}}$) is:

$$\overline{\mathbf{J}}^i_{\mathrm{v}} = \frac{1}{2\pi}\cdot\int_{\phi=0}^{\phi=2\pi}\mathbf{J}^i_{\mathrm{v}}(\phi)d\phi = \frac{C_iL}{V_c}\cdot\frac{N}{2}\cdot\begin{bmatrix}\alpha_{xx} & \alpha_{xy} & 0 & 0\\ \alpha_{yx} & \alpha_{yy} & 0 & 0\\ 0 & 0 & 2\alpha_{zz} & 0\\ 0 & 0 & 2\alpha_{\phi z} & 0\end{bmatrix} \tag{4.48}$$

where

$$
\begin{aligned}
&\alpha_{xx} = \alpha_{yy} = -\cos^2(\theta) \\
&\alpha_{xy} = -\mu\cos(\theta), \qquad \alpha_{yx} = -\alpha_{xy} \\
&\alpha_{zz} = -\sin^2(\theta), \qquad \alpha_{\phi z} = R\mu\sin(\theta) \\
&\alpha_{z\phi} = \frac{c}{\phi_p}\cdot\alpha_{zz}, \qquad \alpha_{\phi\phi} = \frac{c}{\phi_p}\cdot\alpha_{\phi z}
\end{aligned}
\tag{4.49}
$$

By substituting the average terms into Eq.(4.44) and transforming them into the Laplace domain as:

$$
\mathbf{F}_i(s) = \underbrace{\left(\bar{\mathbf{J}}^i + \bar{\mathbf{J}}^i_{\boldsymbol{\tau}} e^{-s\boldsymbol{\tau}} + s\bar{\mathbf{J}}^i_{\mathbf{v}}\right)}_{\bar{\mathbf{A}}_i} \cdot \mathbf{p}^i(s) \;=\; \bar{\mathbf{A}}_i \cdot \mathbf{p}^i(s) \tag{4.50}
$$

where $\bar{\mathbf{A}}_i$ stands for the average directional coefficient matrix for the i^{th} bore location. The transfer function of the whole line boring structure can be placed into Eq.(4.50) as:

$$
\begin{aligned}
&\begin{Bmatrix} \mathbf{F}_1(s) \\ \vdots \\ \mathbf{F}_i(s) \\ \vdots \\ \mathbf{F}_M(s) \end{Bmatrix} = \underbrace{\begin{bmatrix} \bar{\mathbf{A}}_1 & & \cdots & & \mathbf{0} \\ \vdots & \ddots & & & \vdots \\ \mathbf{0} & \cdots & \bar{\mathbf{A}}_i & \cdots & \mathbf{0} \\ \vdots & & & \ddots & \vdots \\ \mathbf{0} & & \cdots & & \bar{\mathbf{A}}_M \end{bmatrix}}_{[\mathbf{DCM}]} \underbrace{\begin{bmatrix} \mathbf{H}_{11}(s) & & \cdots & & \mathbf{H}_{1M}(s) \\ \vdots & \ddots & & & \vdots \\ \mathbf{H}_{i1}(s) & \cdots & \mathbf{H}_{ii}(s) & \cdots & \mathbf{H}_{iM}(s) \\ \vdots & & & \ddots & \vdots \\ \mathbf{H}_{M1}(s) & & \cdots & & \mathbf{H}_{MM}(s) \end{bmatrix}}_{\mathbf{\Phi}(s)} \underbrace{\begin{Bmatrix} \mathbf{F}_1(s) \\ \vdots \\ \mathbf{F}_i(s) \\ \vdots \\ \mathbf{F}_M(s) \end{Bmatrix}}_{\mathbf{F}(s)} \\
&\{0\}_{4M\times 1} = \left([\mathbf{I}]_{4M\times 1} - [\mathbf{DCM}]\cdot\mathbf{\Phi}(s)\right)\cdot\mathbf{F}(s)
\end{aligned}
\tag{4.51}
$$

From Eq.(4.51) the characteristic equation of the dynamic system is represented as:

$$
\det\left([\mathbf{I}]_{4M\times 1} - [\mathbf{DCM}]\cdot\mathbf{\Phi}(s)\right) = 0 \tag{4.52}
$$

At each cutting condition, the stability of the system represented by the characteristic equation is investigated using the Nyquist stability criterion in frequency domain ($s \to j\omega_c$). Details of this method are discussed in section 3.6.2.

4.5 Analysis of Line Boring with Semi Discrete Time Domain Solution

The line boring process is investigated in frequency domain in previous sections. Stepan, [33], presented an analytical method called Semi-Discretization (SD) to solve the stability of delayed periodic systems like milling in time domain. The main advantage of the SD method is that periodic directional coefficients are taken into account without taking their average. Since directional terms are also time varying and periodic in the line boring process when the number of radially spaced inserts is less than 3 (i.e. $N < 3$), the SD method is utilized in this section for stability analysis. In addition to stability, the SD method can be used to predict the vibrations and cutting forces when the linear force model is considered.

The total cutting forces acting at the i^{th} bore location (Eq.(4.10)) are given below:

$$\mathbf{F_i} = \underbrace{\sum_{\mathbf{j}=1}^{N}\left(\mathbf{T_2}\cdot\mathbf{T_1}\cdot\mathbf{K_c}\cdot A^j\right)}_{\textbf{Shearing forces}} + \underbrace{\sum_{\mathbf{j}=1}^{N}\left(\mathbf{T_2}\cdot\mathbf{T_1}\cdot\mathbf{K_e}\cdot L\right)}_{\textbf{Edge forces}} - \underbrace{\sum_{\mathbf{j}=1}^{N}\left(\mathbf{T_2}\cdot\mathbf{T_1}\cdot\mathbf{P_d}\cdot\frac{C_i L}{V_c}\dot{r}^{\mathbf{j}}(t)\right)}_{\textbf{Process damping forces}} \tag{4.53}$$

$\mathbf{F_i}$ can be expressed in machine coordinates by using a similar transformation given in Eqs.(4.41)-(4.45).

$$\mathbf{F_i} = \mathbf{J}^i\cdot\mathbf{p}^i(t) + \mathbf{J}^i_{\boldsymbol{\tau}}\cdot\mathbf{p}^i_0(t-\tau) + \mathbf{J}^i_{\mathbf{v}}\cdot\dot{\mathbf{p}}^i(t) + \mathbf{G}_i(t) \quad \text{with} \quad i = 1,..,M \tag{4.54}$$

where $\mathbf{J}^i, \mathbf{J}^i_{\boldsymbol{\tau}}, \mathbf{J}^i_{\mathbf{v}}$ are process gain matrices, and the stationary cutting force vector $\mathbf{G}_i(t)$ which includes the edge forces and forces arising from the rigid body motion of the line boring bar is:

$$\mathbf{G}_i(t) = \sum_{\mathbf{j}=1}^{N}\left(\mathbf{T_2}\cdot\mathbf{T_1}\cdot\mathbf{K_c}\cdot L\cdot c\sin(\theta)\right) + \sum_{\mathbf{j}=1}^{N}\left(\mathbf{T_2}\cdot\mathbf{T_1}\cdot\mathbf{K_e}\cdot L\right) \tag{4.55}$$

The governing equation of motion (EOM) of the line boring process is written in the machine coordinate system as:

$$\begin{aligned}
&\mathbf{M}\cdot\ddot{\mathbf{p}}(t) + \mathbf{C}\cdot\dot{\mathbf{p}}(t) + \mathbf{K}\cdot\mathbf{p}(t) = \mathbf{F}(t,\tau) \\
&\mathbf{M}\cdot\ddot{\mathbf{p}}(t) + \mathbf{C}\cdot\dot{\mathbf{p}}(t) + \mathbf{K}\cdot\mathbf{p}(t) = \mathbf{J}\cdot\mathbf{p}(t) + \mathbf{J}_{\boldsymbol{\tau}}\cdot\mathbf{p}_0(t-\tau) + \mathbf{J}_{\mathbf{v}}\cdot\dot{\mathbf{p}}(t) + \mathbf{G}(t)
\end{aligned} \tag{4.56}$$

where the total force vector , $\mathbf{F}(t,\tau)$, is constructed by writing the individual forces ($\mathbf{F_i}$) in an augmented matrix form and $\mathbf{M, C, K}$ refer to mass, damping and stiffness matrices respectively. The process gain matrices ($\mathbf{J}$, $\mathbf{J}_{\boldsymbol{\tau}}$, $\mathbf{J}_{\mathbf{v}}$) of the whole line boring structure are introduced as:

$$\mathbf{J}=\begin{Bmatrix}\mathbf{J}^1 & \cdots & \mathbf{0}\\ \vdots & \ddots & \vdots\\ \mathbf{0} & \cdots & \mathbf{J}^M\end{Bmatrix},\ \mathbf{J}_{\boldsymbol{\tau}}=\begin{Bmatrix}\mathbf{J}_{\boldsymbol{\tau}}^1 & \cdots & \mathbf{0}\\ \vdots & \ddots & \vdots\\ \mathbf{0} & \cdots & \mathbf{J}_{\boldsymbol{\tau}}^M\end{Bmatrix},\ \mathbf{J}_{\mathbf{v}}=\begin{Bmatrix}\mathbf{J}_{\mathbf{v}}^1 & \cdots & \mathbf{0}\\ \vdots & \ddots & \vdots\\ \mathbf{0} & \cdots & \mathbf{J}_{\mathbf{v}}^M\end{Bmatrix},$$
$$\mathbf{G}(t)=\begin{Bmatrix}\mathbf{G}_1(t)\\ \vdots\\ \mathbf{G}_M(t)\end{Bmatrix},\ \mathbf{p}(t)=\begin{Bmatrix}\mathbf{p}^1(t)\\ \vdots\\ \mathbf{p}^M(t)\end{Bmatrix} \tag{4.57}$$

In order to apply the SD method, the governing EOM (Eq.(4.56)) is transformed into modal coordinates using mass normalized modal matrix ($\mathbf{U}$):

$$\mathbf{I}\cdot\ddot{\mathbf{q}}(t)+\mathbf{C}_q\cdot\dot{\mathbf{q}}(t)+\mathbf{K}_q\cdot\mathbf{q}(t)=\mathbf{J}_q\cdot\mathbf{q}(t)+\mathbf{J}_{q,\boldsymbol{\tau}}\cdot\mathbf{q}_0(t-\tau)+\mathbf{J}_{q,\mathbf{v}}\cdot\dot{\mathbf{q}}(t)+\mathbf{G}_q(t) \tag{4.58}$$

where

$$\begin{aligned}
&\mathbf{J}_q=\mathbf{U}^{\mathbf{T}}\cdot\mathbf{J}\cdot\mathbf{U}, \qquad \mathbf{G}_q(t)=\mathbf{U}^{\mathbf{T}}\cdot\mathbf{G}(t)\\
&\mathbf{J}_{q,\boldsymbol{\tau}}=\mathbf{U}^{\mathbf{T}}\cdot\mathbf{J}_{\boldsymbol{\tau}}\cdot\mathbf{U}, \qquad \mathbf{p}(t)=\mathbf{U}\cdot\mathbf{q}(t)\\
&\mathbf{J}_{q,\mathbf{v}}=\mathbf{U}^{\mathbf{T}}\cdot\mathbf{J}_{\mathbf{v}}\cdot\mathbf{U}, \qquad \mathbf{q}(t)=\mathbf{U}^{\mathbf{T}}\cdot\mathbf{p}(t)\\
&\mathbf{C}_q=\mathbf{U}^{\mathbf{T}}\cdot\mathbf{C}\cdot\mathbf{U}=\begin{bmatrix}2\zeta_1\omega_{n,1} & & 0\\ & \ddots & \\ 0 & & 2\zeta_M\omega_{n,M}\end{bmatrix}\\
&\mathbf{K}_q=\mathbf{U}^{\mathbf{T}}\cdot\mathbf{K}\cdot\mathbf{U}=\begin{bmatrix}\omega_{n,1}^2 & & 0\\ & \ddots & \\ 0 & & \omega_{n,M}^2\end{bmatrix}
\end{aligned} \tag{4.59}$$

The transformation above is carried out by implementing the orthogonality property of the modes and assuming proportional damping [62], [59]. Subscript q denotes the modal coordinate system. Note that the complete modal matrix ($\mathbf{U}$) is introduced in Eq.(4.58) and (4.59) but the incomplete modal matrix ($\mathbf{U}'$) can be used as well by considering only the dominant modes of the structure. That makes the size of the matrices smaller, and computational efficiency can be achieved with an expense of ignoring higher modes. This is applicable for the line boring structure because the first two modes are dominant, thus the higher modes can be neglected without losing significant data. The governing EOM is rearranged by taking the common terms in one group and leaving the retarded vibrations and static component on the right hand side of Eq.(4.58) as:

$$\mathbf{I}\cdot\ddot{\mathbf{q}}(t)+\left(\mathbf{C}_q-\mathbf{J}_{q,\mathbf{v}}\right)\cdot\dot{\mathbf{q}}(t)+\left(\mathbf{K}_q-\mathbf{J}_q\right)\cdot\mathbf{q}(t)=\mathbf{J}_{q,\boldsymbol{\tau}}\cdot\mathbf{q}_0(t-\tau)+\mathbf{G}_q(t) \tag{4.60}$$

The order of the delayed differential equation (DDE) can be reduced by transforming into the state space format:

$$\begin{aligned}\underbrace{\begin{Bmatrix}\dot{\mathbf{q}}_1(t)\\ \dot{\mathbf{q}}_2(t)\end{Bmatrix}}_{\dot{\mathbf{r}}(t)}&=\underbrace{\begin{bmatrix}[\mathbf{0}] & [\mathbf{I}]\\ -\left(\mathbf{K}_q-\mathbf{J}_q\right) & -\left(\mathbf{C}_q-\mathbf{J}_{q,\mathbf{v}}\right)\end{bmatrix}}_{\mathbf{L}(t)}\cdot\underbrace{\begin{Bmatrix}\mathbf{q}_1(t)\\ \mathbf{q}_2(t)\end{Bmatrix}}_{\mathbf{r}(t)}\\ &\quad+\underbrace{\begin{bmatrix}[\mathbf{0}] & [\mathbf{0}]\\ \mathbf{J}_{q,\boldsymbol{\tau}} & [\mathbf{0}]\end{bmatrix}}_{\mathbf{R}(t)}\cdot\underbrace{\begin{Bmatrix}\mathbf{q}_1(t-\tau)\\ \mathbf{q}_2(t-\tau)\end{Bmatrix}}_{\mathbf{r}(t-\tau)}+\underbrace{\begin{Bmatrix}\{\mathbf{0}\}\\ \mathbf{G}_q(t)\end{Bmatrix}}_{\mathbf{S}(t)}\\ \dot{\mathbf{r}}(t)&=\mathbf{L}(t)\cdot\mathbf{r}(t)+\mathbf{R}(t)\cdot\mathbf{r}(t-\tau)+\mathbf{S}(t)\end{aligned} \tag{4.61}$$

where displacement ($\mathbf{q}_1(t)$) and velocity ($\mathbf{q}_2(t)$) vectors are defined as:

$$\begin{aligned}\mathbf{q}_1(t)&=\mathbf{q}(t), &\quad \dot{\mathbf{q}}_1(t)&=\frac{d\mathbf{q}(t)}{dx}\\ \mathbf{q}_2(t)&=\frac{d\mathbf{q}(t)}{dx}, &\quad \dot{\mathbf{q}}_2(t)&=\frac{d^2\mathbf{q}(t)}{dx^2}\end{aligned} \tag{4.62}$$

The SD method requires the delay period τ to be discretized in time. Thus, τ is divided into k number of discrete time intervals.

$$\tau=k\cdot\Delta t \tag{4.63}$$

The most important aspect of the SD method is that it converts the time varying DDE given in Eq.(4.61) into many ordinary differential equations (ODE) with constant coefficients by approximating the delayed displacement vector ($\mathbf{r}(t-\tau)$) as a linear combination of the delayed discrete values. Let the value of $\mathbf{r}(t_i)$ at time t_i be $\mathbf{r}_i$ and $\mathbf{r}(t_i-\tau)$ be $\mathbf{r}_{i-k}$ as shown in Figure 4-12. Then, when the time interval is small enough, the delayed term can be approximated as:

$$\mathbf{r}(t-\tau) \approx \frac{\mathbf{r}_{i-k} + \mathbf{r}_{i-k+1}}{2} \qquad \text{if} \qquad t \in [t_i, t_{i+1}] \tag{4.64}$$

It should be noted that the higher order approximation of the delayed term is also used in literature, as presented by Insperger [63]. The same as the delayed term, if time interval is chosen to be sufficiently small, the time dependent state matrices $\mathbf{L}(t)$, $\mathbf{R}(t)$ and $\mathbf{S}(t)$ can be approximated as constant in each time interval.

$$\begin{aligned}
\mathbf{L}(t) &= \mathbf{L}_i = \frac{1}{\Delta t}\int_{t_i}^{t_{i+1}} \mathbf{L}(t)dt \\
\mathbf{R}(t) &= \mathbf{R}_i = \frac{1}{\Delta t}\int_{t_i}^{t_{i+1}} \mathbf{R}(t)dt \quad \text{if} \quad t \in [t_i, t_{i+1}] \\
\mathbf{S}(t) &= \mathbf{S}_i = \frac{1}{\Delta t}\int_{t_i}^{t_{i+1}} \mathbf{S}(t)dt
\end{aligned} \tag{4.65}$$

As a result, by substituting (4.64) and (4.65) into (4.61), the DDE is reduced to an ODE in the small time intervals as:

$$\dot{\mathbf{r}}(t) = \mathbf{L}_i \cdot \mathbf{r}(t) + \mathbf{R}_i \cdot \left(\frac{\mathbf{r}_{i-k} + \mathbf{r}_{i-k+1}}{2}\right) + \mathbf{S}_i \qquad \text{if} \qquad t \in [t_i, t_{i+1}] \tag{4.66}$$

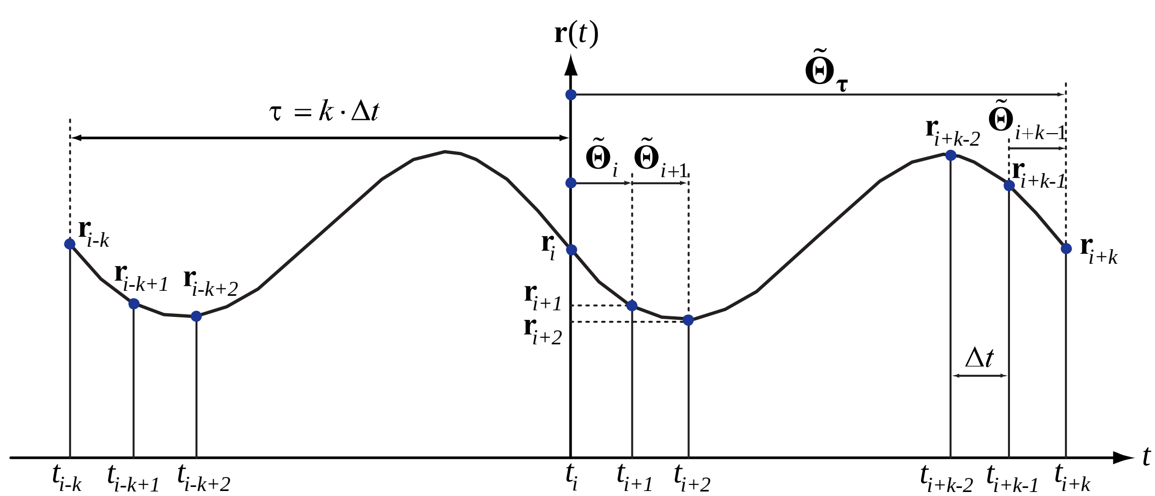

Figure 4-12 : Discretization of periodic vibrations at each semi-discrete interval

The exact solution of the first order ODE (4.66) can be evaluated at each semi-discretization interval (i.e. $t_i < t < t_{i+1}$). Details of the solution are provided in Appendix B. The solution is presented below as a recursive equation:

$$\mathbf{r}_{i+1} = \mathbf{N}_{i,1} \cdot \mathbf{r}_i + \mathbf{N}_{i,2} \cdot \left(\mathbf{r}_{i-k} + \mathbf{r}_{i-k+1}\right) + \mathbf{N}_{i,3} \tag{4.67}$$

where the coefficient matrices:

$$\begin{aligned} \mathbf{N}_{i,1} &= e^{\mathbf{L}_i \Delta t} \\ \mathbf{N}_{i,2} &= \frac{1}{2}\left(e^{\mathbf{L}_i \Delta t} - \mathbf{I}\right) \cdot \mathbf{L}_i^{-1} \cdot \mathbf{R}_i \\ \mathbf{N}_{i,3} &= \frac{1}{2}\left(e^{\mathbf{L}_i \Delta t} - \mathbf{I}\right) \cdot \mathbf{L}_i^{-1} \cdot \mathbf{S}_i \end{aligned} \tag{4.68}$$

This recursive expression indicates that the next state vector ($\mathbf{r}_{i+1}$) can be expressed in terms of the current state vector ($\mathbf{r}_i$) and one tooth period (τ) earlier state vectors ($\mathbf{r}_{i-k}$, $\mathbf{r}_{i-k+1}$) of the dynamic system.

4.5.1 Chatter Stability Analysis Using Semi-Discretization

The stability of the dynamic line boring process is investigated by employing the SD method. As it is the case in frequency domain analysis, the static component of the force ($\mathbf{G}_i(t)$ in Eq.(4.55)) is dropped because it does not influence the instability of the system. Thus, the derived first order ODE (Eq.(4.66)) in small time steps becomes as:

$$\dot{\mathbf{r}}(t) = \mathbf{L}_i \cdot \mathbf{r}(t) + \mathbf{R}_i \cdot \left(\frac{\mathbf{r}_{i-k} + \mathbf{r}_{i-k+1}}{2}\right) \quad \text{where} \quad t \in \left[t_i, t_{i+1}\right] \tag{4.69}$$

The solution of Eq.(4.69) is obtained in the same way as it was in the previous section. The only difference is that the static force vector ($\mathbf{S}_i$) does not appear in the solution. As a result, the recursive equation for the next state vector has the form:

$$\mathbf{r}_{i+1} = \mathbf{N}_{i,1} \cdot \mathbf{r}_i + \mathbf{N}_{i,2} \cdot \left(\mathbf{r}_{i-k} + \mathbf{r}_{i-k+1}\right) \tag{4.70}$$

where the coefficients $\mathbf{N}_{i,1}$, $\mathbf{N}_{i,2}$ are given in Eq.(4.68). If the series of equations is written at each time step (Δt) within one tooth period (τ) of time by using this recursive equation, a discrete map can be constructed as:

$$\mathbf{\Gamma}_{i+1} = \mathbf{\Theta}_i \cdot \mathbf{\Gamma}_i \tag{4.71}$$

where

$$\boldsymbol{\Gamma}_{i+1} = \begin{Bmatrix} \mathbf{r}_{i+1} \\ \mathbf{r}_i \\ \vdots \\ \mathbf{r}_{i-k+1} \end{Bmatrix}, \quad \boldsymbol{\Gamma}_i = \begin{Bmatrix} \mathbf{r}_i \\ \vdots \\ \mathbf{r}_{i-k+1} \\ \mathbf{r}_{i-k} \end{Bmatrix}, \quad \boldsymbol{\Theta}_i = \begin{bmatrix} \mathbf{N}_{i,1} & \mathbf{0} & \cdots & \mathbf{0} & \mathbf{N}_{i,2} & \mathbf{N}_{i,2} \\ \mathbf{I} & \mathbf{0} & \cdots & \mathbf{0} & \mathbf{0} & \mathbf{0} \\ \mathbf{0} & \mathbf{I} & & \vdots & \vdots & \vdots \\ \vdots & \vdots & \ddots & \mathbf{0} & \mathbf{0} & \mathbf{0} \\ \mathbf{0} & \cdots & \mathbf{0} & \mathbf{I} & \mathbf{0} & \mathbf{0} \\ \mathbf{0} & \cdots & \mathbf{0} & \mathbf{0} & \mathbf{I} & \mathbf{0} \end{bmatrix} \tag{4.72}$$

The size of the transition matrix $\boldsymbol{\Theta}_i$ is $2q(k+1)\,\mathbf{x}\,2q(k+1)$ and $q,\ k$ denote the number of structural modes considered and number of discretizations, respectively. However, a simplification can be applied to reduce the size of the transition matrix [33]. Since $\dot{\mathbf{q}}_0(t-\tau)$ does not appear in the EOM (see Eq.(4.58)), the second column of matrix $\mathbf{R}_i$ is zero, so is the second column of matrix $\mathbf{N}_{i,2}$. Thus, $\mathbf{r}_{i+1}$ does not depend on $\dot{\mathbf{q}}_{i-k+1}$ and $\dot{\mathbf{q}}_{i-k}$. For this reason, a new vector ($\tilde{\boldsymbol{\Gamma}}_i$) is defined instead of $\boldsymbol{\Gamma}_i$ as:

$$\tilde{\boldsymbol{\Gamma}}_i = \begin{Bmatrix} \mathbf{q}_i & \dot{\mathbf{q}}_i & \mathbf{q}_{i-1} & \mathbf{q}_{i-2} & \cdots & \mathbf{q}_{i-k} \end{Bmatrix}^{\mathbf{T}} \tag{4.73}$$

where the size of $\tilde{\boldsymbol{\Theta}}_i$ and $\tilde{\boldsymbol{\Gamma}}_i$ is reduced to $q(k+2)\,\mathbf{x}\,q(k+2)$ and $q(k+2)\,\mathbf{x}\,\mathbf{1}$ respectively. The transition over the tooth period τ is determined by coupling each transition matrix $\tilde{\boldsymbol{\Theta}}_i$ as illustrated in Figure 4-12 and given by:

$$\tilde{\boldsymbol{\Gamma}}_{i+k} = \tilde{\boldsymbol{\Theta}}_\tau \cdot \tilde{\boldsymbol{\Gamma}}_i \tag{4.74}$$

where the overall transition matrix is $\tilde{\boldsymbol{\Theta}}_\tau = \tilde{\boldsymbol{\Theta}}_{i+k-1} \cdot \tilde{\boldsymbol{\Theta}}_{i+k-2} \cdots \tilde{\boldsymbol{\Theta}}_{i+1} \cdot \tilde{\boldsymbol{\Theta}}_i$. Here each transition matrix should be calculated at its own time interval because of the time varying periodic process gain matrices $\mathbf{J},\ \mathbf{J}_{\boldsymbol{\tau}},\ \mathbf{J}_{\mathbf{v}}$ in Eq.(4.56). But it is sufficient to calculate transition matrix over one tooth period due to the periodic nature of the cutting operation, i.e. $\tilde{\boldsymbol{\Theta}}_{\tau+k} = \tilde{\boldsymbol{\Theta}}_\tau$.

The stability of the dynamic system can be investigated by calculating the eigenvalues of the transition matrix $\tilde{\boldsymbol{\Theta}}_\tau$ based on the Floquet Theory. The system is stable if all of the eigenvalues have modulus less than one, critically stable if all of them have unity modulus and unstable if any of the eigenvalues have modulus greater than one. In order to obtain a stability chart, a range of spindle speeds and width of cut values must be scanned. In that sense, a matrix size reduction carried in Eq.(4.73) is very useful in terms of computational efficiency because the stability is inspected repeatedly at each cutting condition.

At low spindle speeds, which correspond to high stability lobes, there are many vibration waves left on the surface. In order to capture those vibrations in the SD stability analysis, one has to increase the number of divisions in one period, i.e. high k value. This results in computational difficulties because the size of the transition matrix becomes very big and the computation time increases as well.

4.5.2 Prediction of Cutting Forces and Vibrations in Time Domain

The time domain simulation of linear cutting processes is also possible using the Semi Discretization method. Unlike the stability analysis, the static component of the total force vector should be accounted for in the vibration prediction, that is $\mathbf{G}_i(t)$ in Eq.(4.55). The reason for this is that the static component brings in forced vibrations which cannot be ignored in the transient part of the time domain simulation. The recursive equation obtained by solving the DDE in small time intervals can be used to calculate the state vector at the next time step that requires three state vectors ($\mathbf{r}_i$, $\mathbf{r}_{i-k}$ and $\mathbf{r}_{i-k+1}$) as shown below:

$$\mathbf{r}_{i+1} = \mathbf{N}_{i,1} \cdot \mathbf{r}_i + \mathbf{N}_{i,2} \cdot \left(\mathbf{r}_{i-k} + \mathbf{r}_{i-k+1}\right) + \mathbf{N}_{i,3} \tag{4.75}$$

During the first tooth period, there is not any regenerative effect introduced to the process because the cutting surface is assumed to be free of vibration marks initially. Thus, during the first tooth period which corresponds to the first k state vectors, state vectors from the previous pass ($\mathbf{r}_{i-k}$ and $\mathbf{r}_{i-k+1}$) have zero value but still forced vibrations exist, and it determines the displacements and velocities of the next state vector, $\mathbf{r}_{i+1}$. After calculating the states of the first tooth period using Eq.(4.75), $\mathbf{r}_{i-k}$ and $\mathbf{r}_{i-k+1}$ are effective in the system and they introduce the regenerative vibrations to the time domain simulation for the successive state computations. In this way, the vibrations and the velocity of vibrations can be predicted in modal coordinates which can be transformed into the machine coordinate system by multiplying them with the modal matrix $\mathbf{V}$ obtained in section 4.2.

After the vibrations are predicted as explained above, the cutting forces can be calculated by simply substituting the discrete vibrations and velocities into the cutting force expression given in Eqs.(4.56)-(4.57):

$$\mathbf{F}(t_i,\tau) = \mathbf{J}\cdot\mathbf{p}(t_i) + \mathbf{J}_{\boldsymbol{\tau}}\cdot\mathbf{p}_0(t_{i-k}) + \mathbf{J}_{\mathbf{v}}\cdot\dot{\mathbf{p}}(t_i) + \mathbf{G}(t_i) \tag{4.76}$$

which gives force vector at time t_i. By repeating this calculation for several spindle revolutions, the cutting forces are predicted.

Note that the time domain simulation presented above does not take tool jump into account, which happens when excessive vibrations are present in the system. Tool jump introduces non-linearity to the cutting process, and cutting forces are not generated when the tool is out of cut. This is not addressed in the above proposed method.

Examples of the vibration and force prediction are presented in section 4.6.1 for both unstable and stable operating conditions.

4.6 Simulation Results

The proposed methods are compared at different cutting conditions. A 4 cylinder engine is considered as a case study; however, note that the model is reconfigurable to any other type of boring operation. For example, when the axially located insert number is one (i.e. $M=1$), the model represents a boring head. When the engine has many cylinders, the length of the bar also increases. Thus, machine builders put additional support bearings to make a more rigid structure. When the stiffness information of the bearings is available, this can be input to the FE model and proper FRF can be estimated.

Table 4-1 shows all of the simulation parameters including the insert geometry and cutting force coefficients.

Table 4-1 : Simulation parameters: Insert geometry, cutting conditions, workpiece properties

Parameter	Value	Unit
Approach angle (κ_r)	80	[°]
Feed-rate (c)	0.05	[mm/rev/tooth]
Nose radius (r_ε)	0.4	[mm]
Cutting Coefficients (Table 3.3) K_{rc}, K_{tc}, K_{ac} K_{re}, K_{te}, K_{ae}	 1413, 2530, 0 131, 62, 0	 [N/mm^2] [N/mm]
Process damping coefficient (Table 3.6) (C_i)	2.25 x 10^5	[N/m]
Bearing stiffness in radial direction (k_r)	3.85 x 10^8	[N/m]
Line Boring Bar: Radius (R) Young's Modulus (E) Poisson's ratio (ν) Density (ρ)	 25 200 0.3 7850	 [mm] [GPa] [ ] [kg/m^3]
Damping ratio for each mode (ζ)	0.03	[ ]

4.6.1 Comparison of Stability Prediction Methods

Three different methods are proposed for line boring stability prediction, namely the Zero Order Solution, the Nyquist Stability Method, and Semi-Discretization. The first one is easy to apply and computationally fast compared to the others, but it does not consider the effect of insert geometry on the chip flow and process damping forces. The main difference between the Nyquist Method and Semi-Discretization is that, unlike the Nyquist Method, Semi-Discretization is able to consider the time varying directional factors which exist in the system when there are less than 3 inserts at each bore location. A 4-cylinder engine shown in Figure 4-2 is considered for simulations. There are 5 axially spaced inserts ($M = 5$) and at each bore location there is only one insert ($N = 1$). Insert locations along the line boring bar are given in

Figure 4-13, as well as the cross sectional views. In this particular example, all of the inserts are in the same orientation with respect to each other. For supporting conditions, the first node of the bar (marked as 1 in

Figure 4-13) is assumed to be fixed because it is close to the spindle which is less flexible than the line boring bar. The free end of the boring bar is supported with a bearing at node 7. The Finite Element model resulted in bending modes presented in Table 4-2.

Table 4-2 : First 5 natural frequencies of bending modes

	1^{st} Mode	2^{nd} Mode	3^{rd} Mode	4^{th} Mode	5^{th} Mode
Bending Mode [Hz]	492	1488	2336	3057	4787

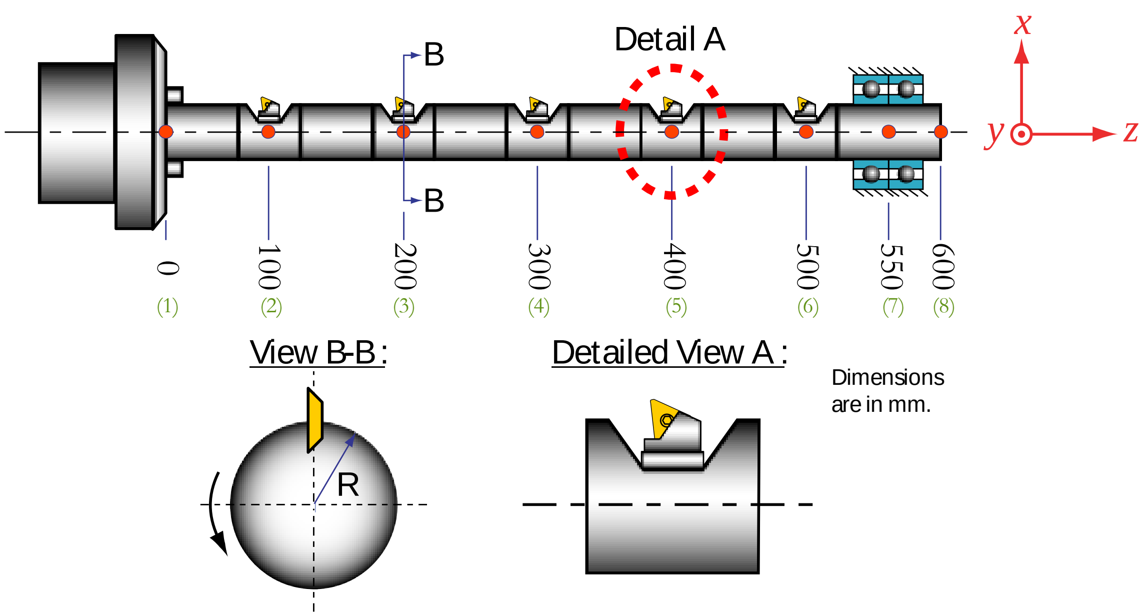

Figure 4-13 : Dimensions of line boring bar for a 4-cylinder engine

All three prediction results are shown in Figure 4-14. The Zero Order Solution (ZOS) resulted in a minimum critical width of cut value of 2 mm, and it is constant through the whole spindle speed range. The reason for the constant minimum value is because the speed dependent process damping force is neglected there. The Nyquist Stability Method (NSM) and Semi-Discretization (SD) resulted in a very low minimum critical width value of around 0.3 mm compared to ZOS. This is because of the equivalent chip flow angle estimation included in the NSM and SD. For each cutting condition, the NSM and

SD adjust the cutting force directions for the stability solution. The chip flow angle is the key parameter for the chatter stability prediction because it determines how much the cutting forces are projected into the chip thickness direction. As the chip flow angle decreases, the forces are directed toward the radial direction of the boring bar which is more flexible than the axial direction. However in ZOS, the chip flow angle is assumed to be constant and equal to the approach angle κ_r which is 80 degrees in this case. At a low speed range, the stable region gets larger in the NSM and SD predictions due to process damping. The difference between two comes from the time varying directional coefficients which are taken into account in the SD method but only average terms are used in the NSM. This difference resulted in a very small difference at high speed predictions which can be neglected, but the difference is significant at low speeds where the process damping is effective. The chatter frequency figure shows that the first bending mode dominates the chatter vibrations.

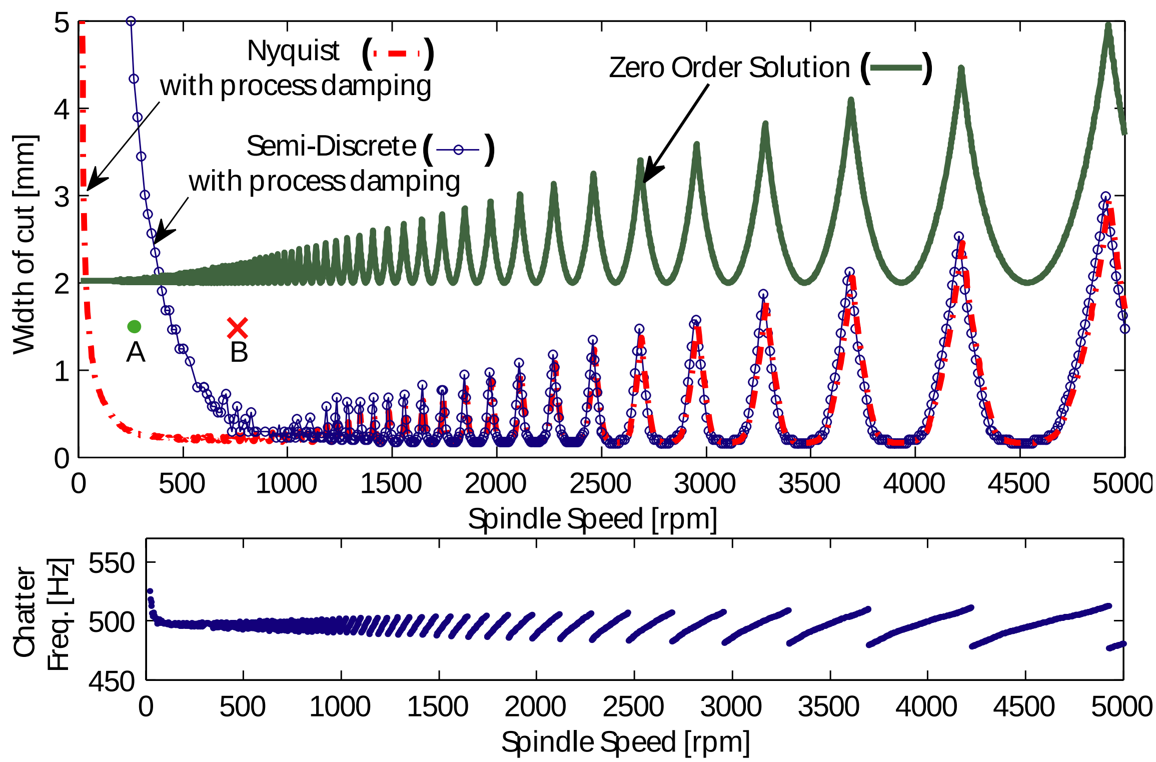

Figure 4-14 : Stability chart and chatter frequencies. Comparison of three stability prediction methods: Zero Orders Solution, Nyquist Method and Semi-discretization. See Table 4-1 and Figure 4-13 for cutting conditions

The vibrations and forces in the machine coordinate system are predicted by methods developed in section 4.5.2. One stable and one unstable condition (marked as A and B in Figure 4-14) are simulated in the time domain for 15 spindle revolutions. Simulation results are plotted in Figure 4-15 and Figure 4-16 respectively. Both of them experience the transient vibrations during the first two revolutions, but after that case A becomes fully stable. On the other hand, regenerative vibrations are dominant in case B and both displacements and forces grow rapidly.

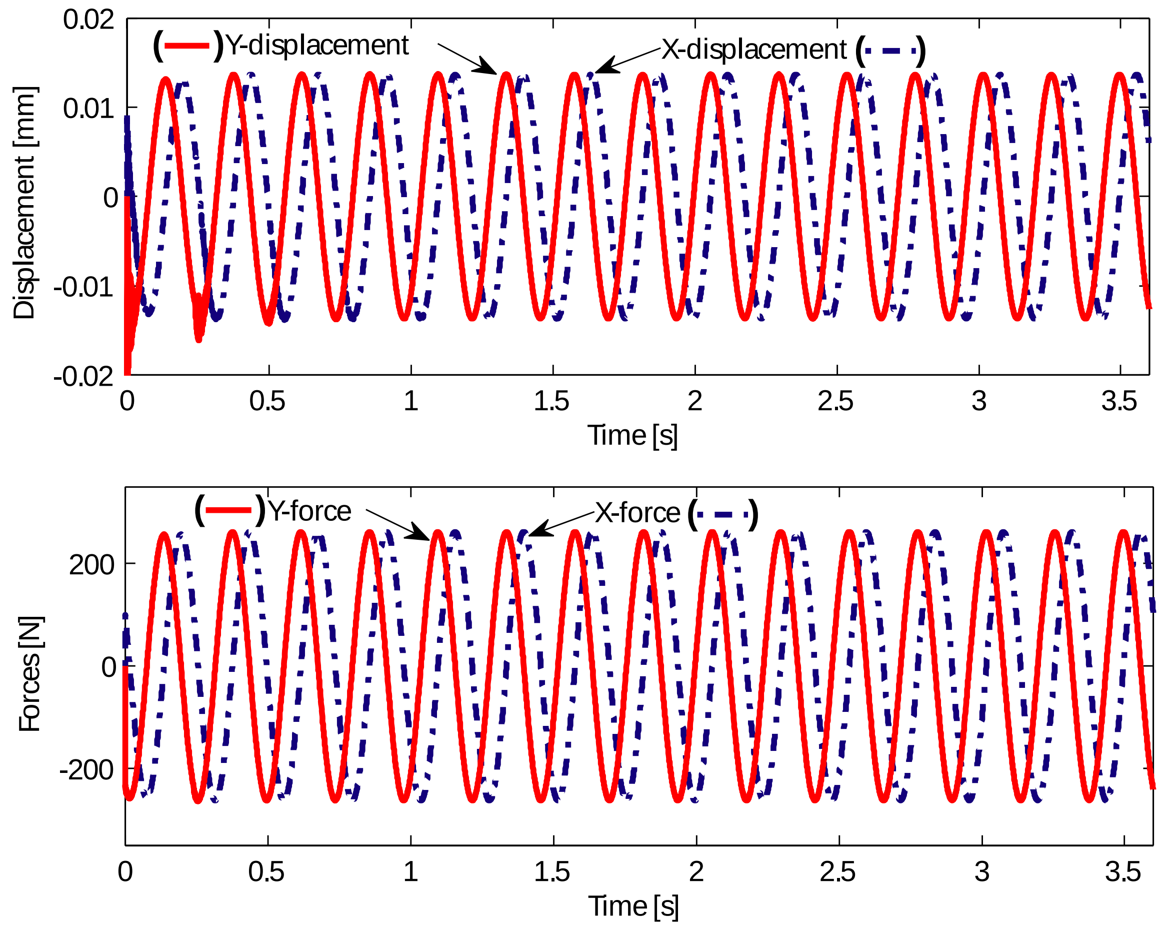

Figure 4-15 : Displacement and force simulation using Semi Discretization time domain method for condition A in Figure 4-14 (Width of cut = 1.5mm, Spindle speed = 250rpm, first 15 revolutions are presented, 4th node in Figure 4-13)

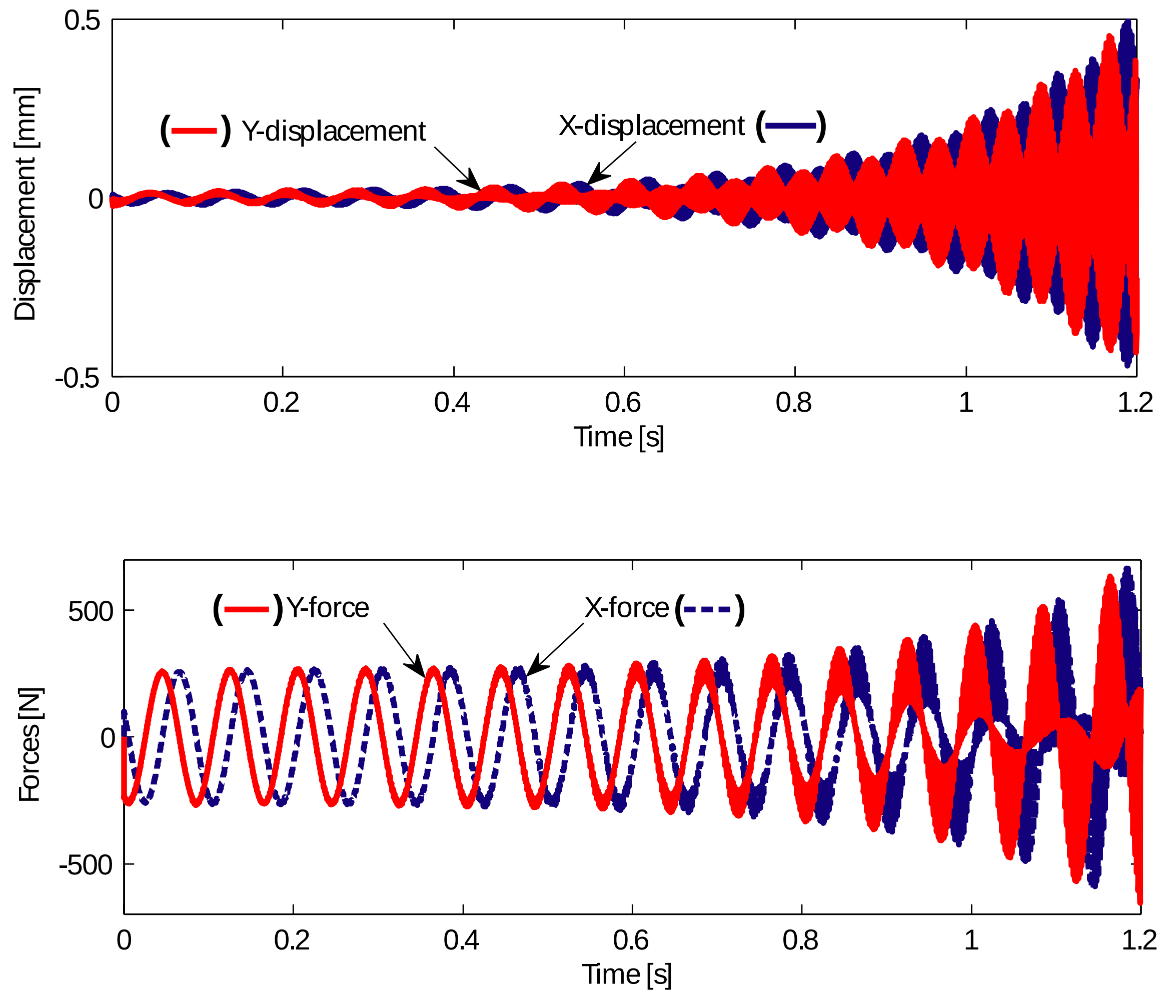

Figure 4-16 : Displacement and force simulation using semi discretization time domain method for condition B in Figure 4-14 (Width of cut = 1.5mm, Spindle speed = 750rpm, first 15 revolutions are presented, 4th node in Figure 4-13)

4.6.2 Comparison of Different Number of Inserts (N=1,2,3)

One of the design considerations of the line boring tool is the number of inserts at each bore. Figure 4-17 shows three different cases for comparison purposes. Case (a) has only one, case (b) has two and case (c) has three inserts at each bore location. Insert orientations with respect to each other are the same for each boring tool. The ZOS results are plotted in Figure 4-18, and it can be concluded that as the number of radially spaced inserts increases, the minimum critical width of cut value decreases. This result can also be obtained by looking at the limit depth of cut expression derived for milling in [10] which suggests that the limit depth value is inversely proportional to the number of teeth in the milling tool. The same analogy applies here when radially spaced inserts are considered as in milling. Thus, as the productivity increases with the number of inserts, the instability problems may arise in the cutting process. The NSM and SD results are shown in Figure 4-14, Figure 4-19 and Figure 4-20 for cases a, b, c shown in Figure 4-17 respectively. Both the NSM and SD show the same trend as it is seen in ZOS when more inserts are used at each bore location. However, since the limit width of cut values are very small, it is hard to distinguish the difference in most of the spindle speed range. When 1-insert (N=1, Figure 4-14) and 2-insert (N=2, Figure 4-19) cases are analyzed, it is again clear that SD and NSM show a very small difference at high speeds but a large difference at low speeds, i.e. below 1000 rpm. But the 3-insert (N=3, Figure 4-20) case demonstrates that NSM and SD predictions match at high speeds as well as low speeds. This is an expected result because the time varying coefficients become time invariant when there are 3 or more inserts at each bore location, i.e. N≥3 as discussed in section 4.6.1.

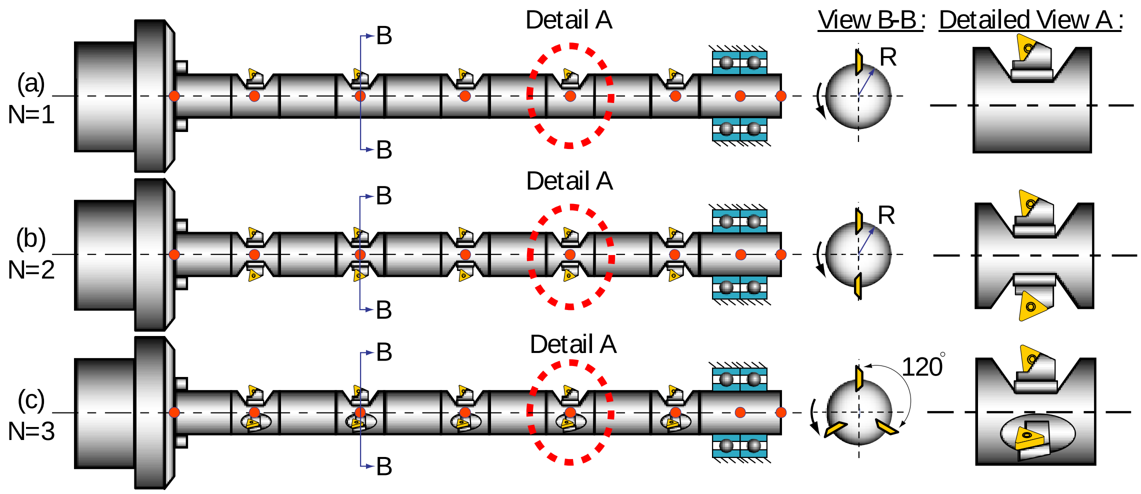

Figure 4-17 : Pictorial representation of line boring bar having different number of insert at each bore location (N=1,2,3), cross sectional and detailed views.

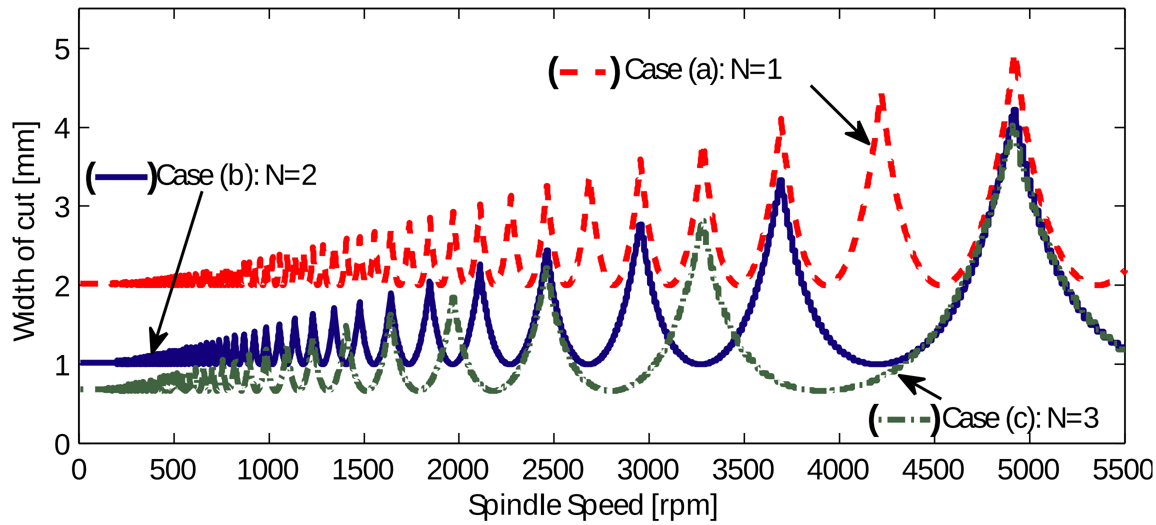

Figure 4-18 : Comparison of number of inserts with Zero Order Solution for cases given in Figure 4-17. Case (a) : 1 insert (N=1), Case (b) : 2 inserts (N=2) and Case (c) : 3 inserts (N=3)

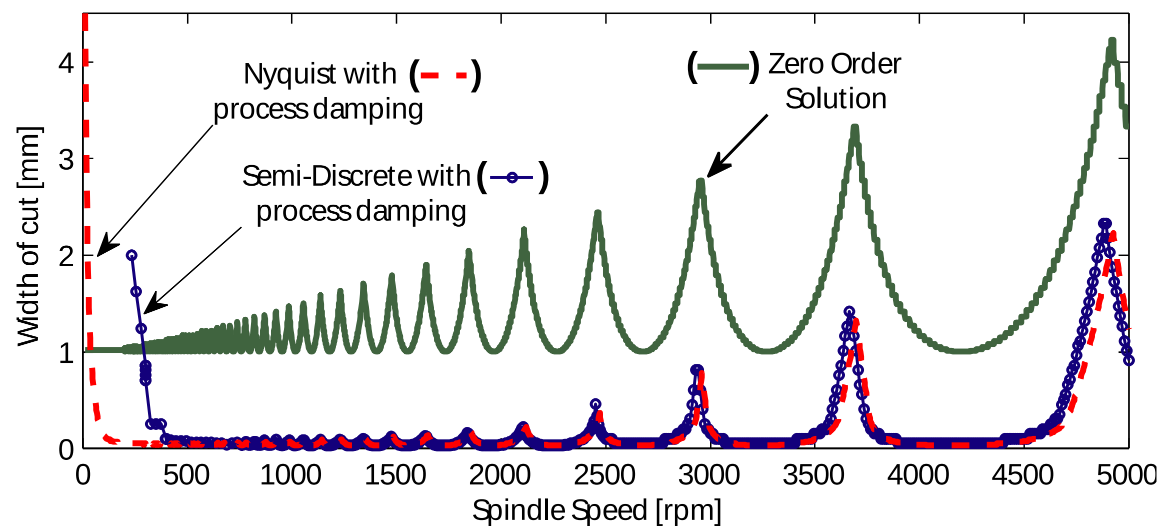

Figure 4-19 : Comparison of stability charts when there are 2 inserts (N=2) at each bore location, see Figure 4-17-b. Process damping effect is included.

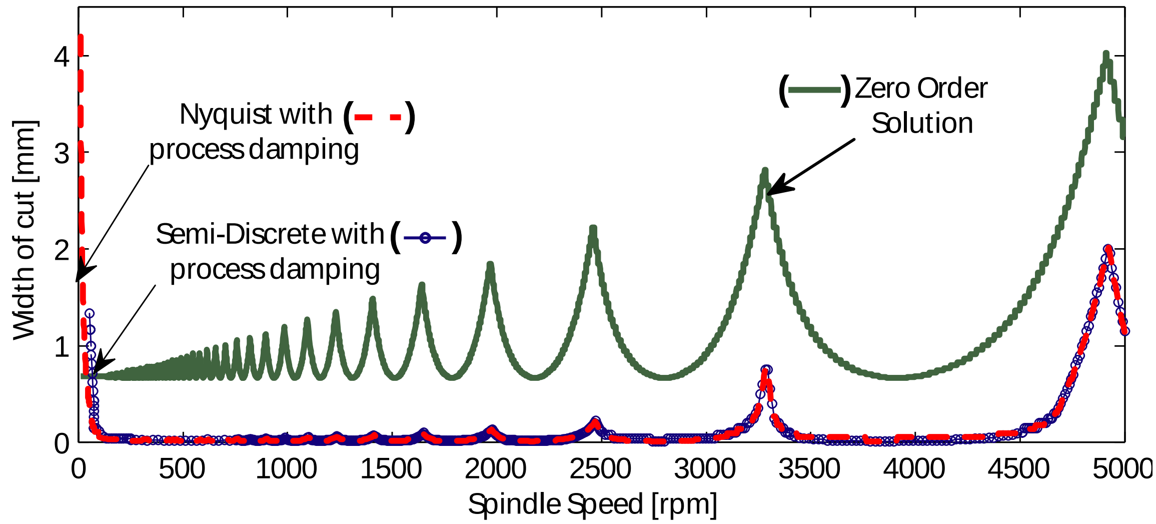

Figure 4-20 : Comparison of stability charts when there are 3 inserts (N=3) at each bore location, see Figure 4-17-c. Process damping effect is included.

4.6.3 Comparison of Different Angular Position of Inserts

Besides the number of inserts, the angular orientation of the insert with respect to each other is also an important design consideration addressed in this section. For this purpose, 1-insert, 2-insert and 3-insert tools with different angular orientations are compared. The main reason for this is to investigate the influence of time varying coefficients in detail.

Figure 4-21 demonstrates 3 cases, all of which have 1-insert at each bore (N=1). Case (a) has all the inserts at the same orientation which is also studied in previous sections. Case (b) differs from case (a) by having consecutive inserts with 180° angular difference with respect to each other. Case (c) has inserts having 90° and 270° angular differences at each successive bore position. Stability charts are obtained with ZOS, NSM and SD methods. However, the ZOS and NSM result in the same stability border for all 3 cases because average directional terms are used in those methods. Different angular orientation introduces just a phase shift in directional coefficients, but average terms stay the same no matter what the orientation is, as long as the number of inserts is kept constant. Thus, stability of each case is investigated by SD method only, as shown in Figure 4-22. Case (a) and case (b) gave exactly the same result which can be explained with the directional terms again. Figure 4-10 shows the variation of directional terms with respect to the angular position of the insert. Since bending vibrations are dominant in the line boring application, directional terms in radial directions (a_{xx}, a_{xy}, a_{yx} and a_{yy}) are the key parameters where stability is concerned. But all of the four terms are 180° periodic, so the phase shift does not introduce any difference to the dynamic system, and case (a) and case (b) give identical results. Case (c) obviously is the worst angular orientation among the 3 cases according to the stability results.

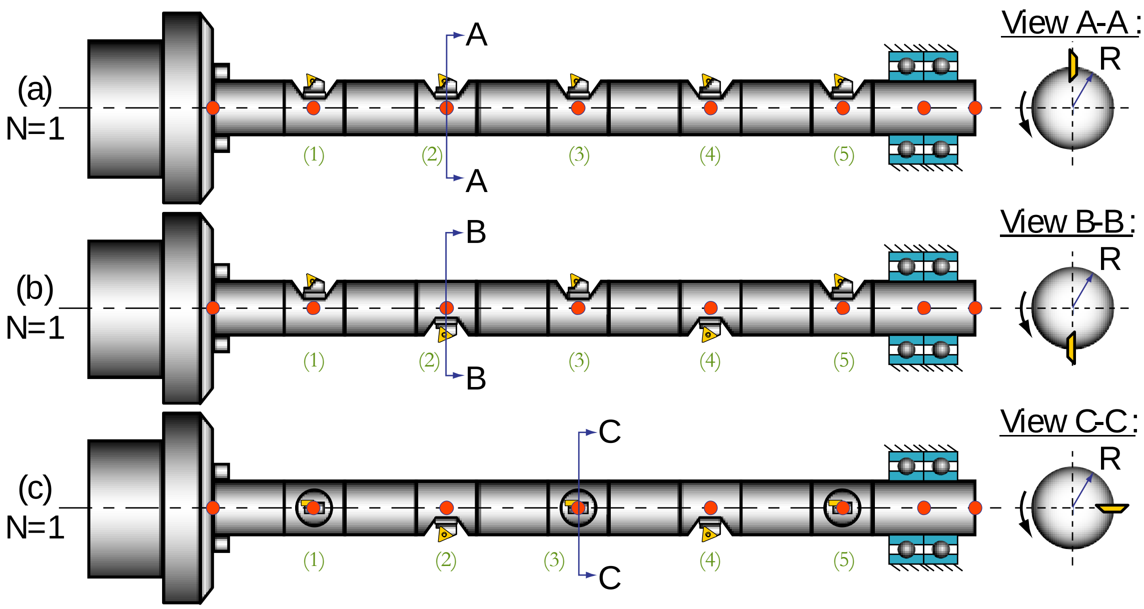

Figure 4-21 : 1 insert at each bore location (N=1) (a) All of the inserts have view A-A orientation. (b) inserts at nodes 1,3,5 have view A-A, nodes 2,4 have view B-B orientation (c) inserts at nodes 1,3,4 have view C-C, nodes 2,4 have view B-B orientation

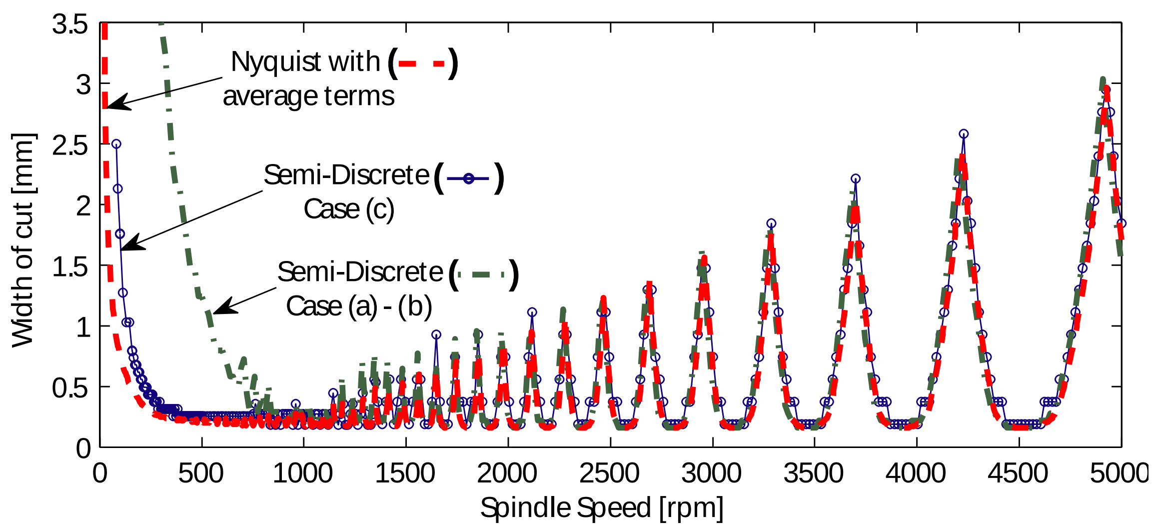

Figure 4-22 : Stability comparison for case a-b-c in Figure 4-21. (N=1)

A similar approach is employed for the 2-insert condition. Insert configurations are illustrated in Figure 4-23. Case (a) has the same orientation for all inserts, whereas a 90° angular difference exists from one insert to the next one in case (b). Since directional terms are still time variant and periodic at 180°, the ZOS and NSM are not able to capture the difference; only the SD method can capture that. Thus, the SD results are shown in Figure 4-24 along with the NSM results. Case (b) resulted in almost the same stability border with the NSM. However, case (a) differs from case (b) especially at low spindle speeds and gives higher stable width of cut values.

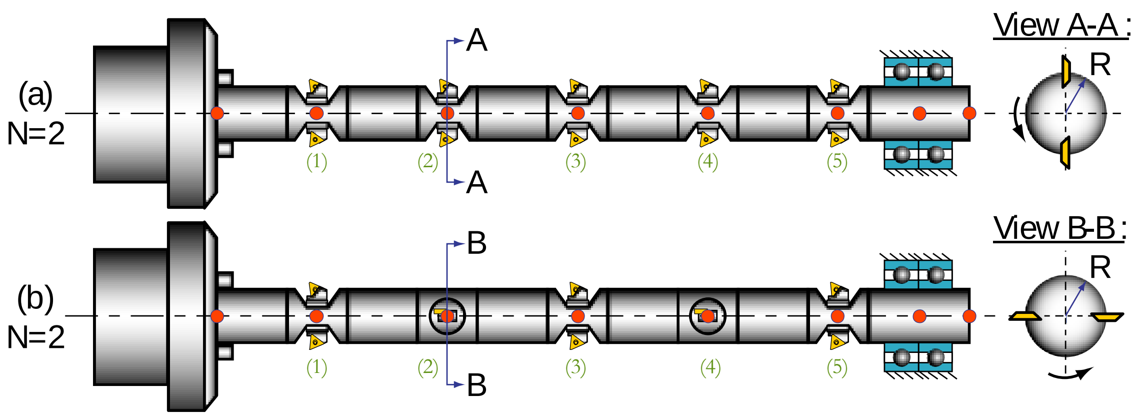

Figure 4-23 : 2 inserts at each bore location. (a) All of the inserts have view A-A orientation. (b) inserts at nodes 1,3,5 have view A-A, nodes 2,4 have view B-B orientation

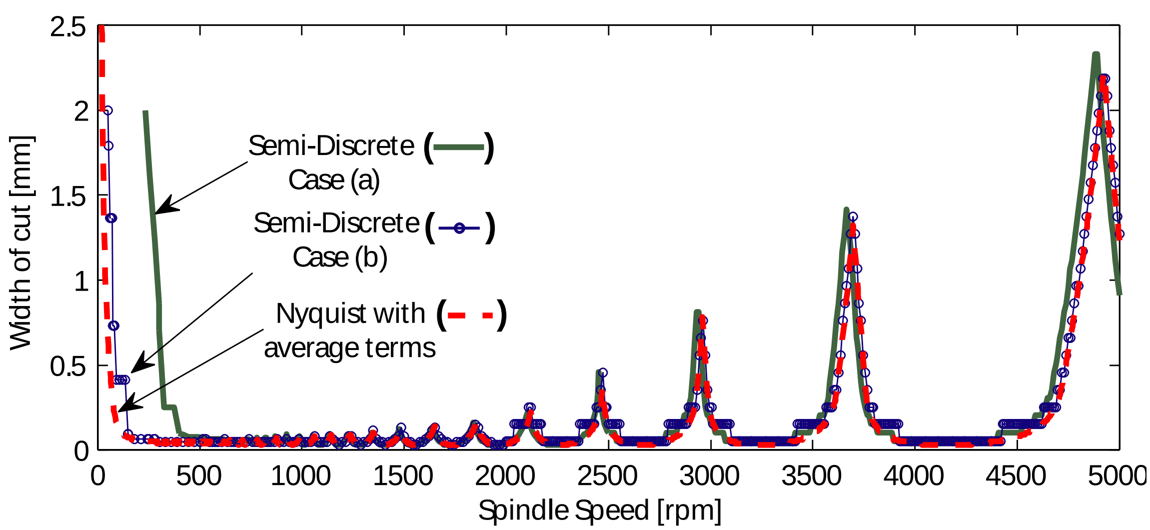

Figure 4-24 : Stability comparison for case a-b in Figure 4-23. ($N = 2$)

The last angular orientation comparison is done for 3-inserted line boring tools. Angular configurations are shown in Figure 4-25. Case (a) has the same angular orientation for all inserts, but case (b) has inserts which are oriented with a 60° angular phase difference. It is previously mentioned that when the insert number at each bore location is greater than two, the directional coefficients turn into time-invariant values and are equal to the average terms. Thus, case (a), case (b) and NSM should theoretically result in the same stability border. Results are illustrated in Figure 4-26 and, as expected, all three gave exactly the same stability border.

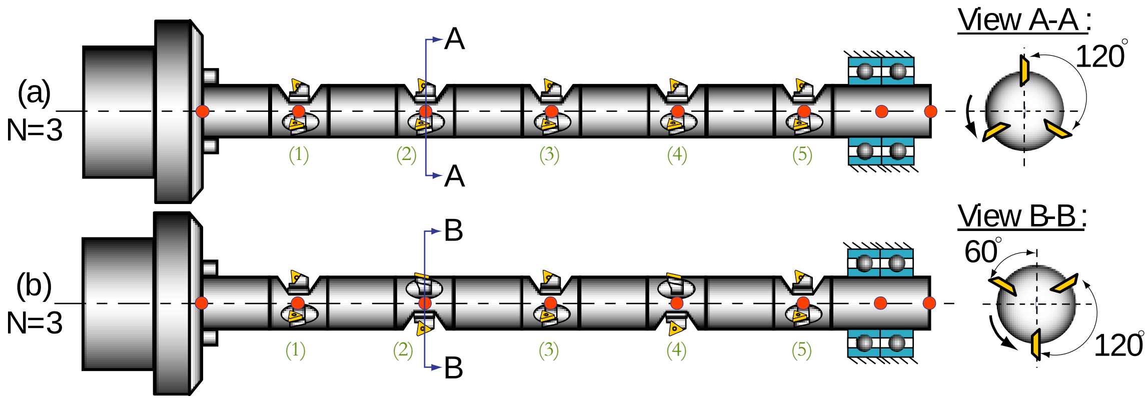

Figure 4-25 : 3 inserts at each bore location (N=3) (a) All of the inserts are oriented same as view A-A. (b) inserts at nodes 1,3,5 have view A-A, nodes 2,4 have view B-B orientation

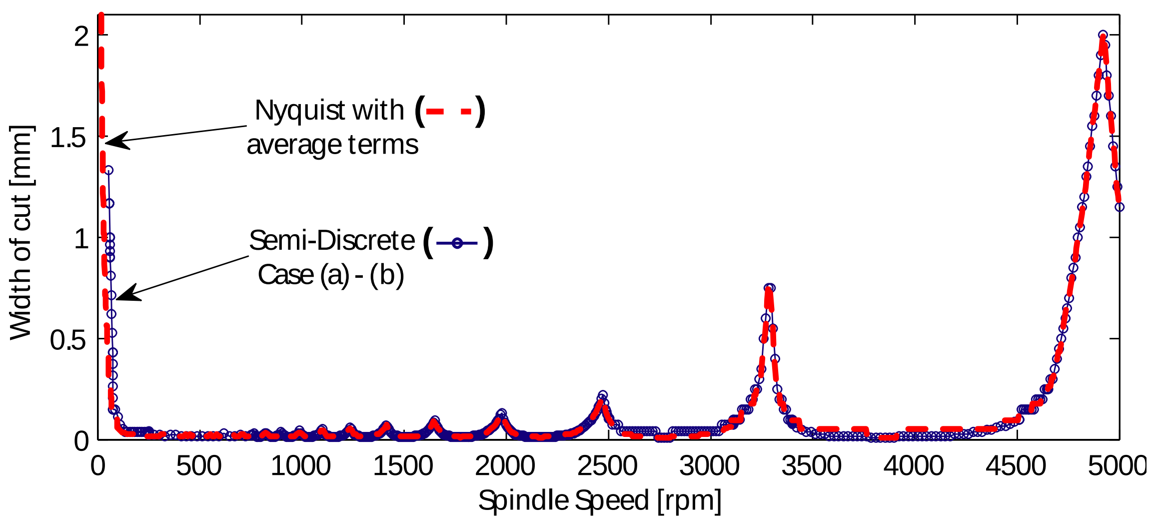

Figure 4-26 : Stability comparison for case a-b in Figure 4-25. ($N = 3$)

4.6.4 Comparison of Different Support Conditions

The effect of support conditions on natural frequencies and mode shapes is discussed in section 4.2. In this section, the location of the support bearing will be examined. For this purpose, a 5-cylinder engine, which has 6 crankshaft bores, is considered in simulations.

The dimensions of the boring bar and the insert locations are shown in Figure 4-27. Other simulation parameters are the same as the ones used in previous sections. Angular orientation of the inserts is kept the same in order to see the support effect on chatter stability.

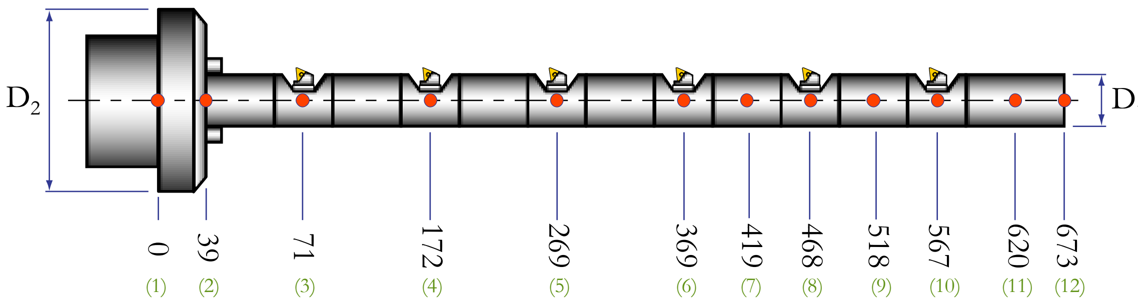

Figure 4-27 : Dimensions of line boring bar for a 5-cylinder engine, one insert for each bore (N=1), dimension are in mm. $D_1 = 50$mm, $D_2 = 100$mm

The outboard bearing is placed at three different positions on the bar; those being the 11th, 9th and 7th node of the bar as seen in Figure 4-28. All three cases are modeled as beam elements, and radial spring elements are added at the corresponding bearing locations. The first four bending natural frequencies are listed in Table 4-3 and mass normalized mode shapes are shown in Figure 4-29. The only difference between those three cases is the FRF at the cutting points.

Table 4-3 : First 4 natural frequencies of bending modes for cases in Figure 4-28

Bending Modes [Hz]	1st Mode	2nd Mode	3rd Mode	4th Mode
Case (a)	438	1337	2233	2758
Case (b)	523	904	1833	3088
Case (c)	318	1086	1881	2816

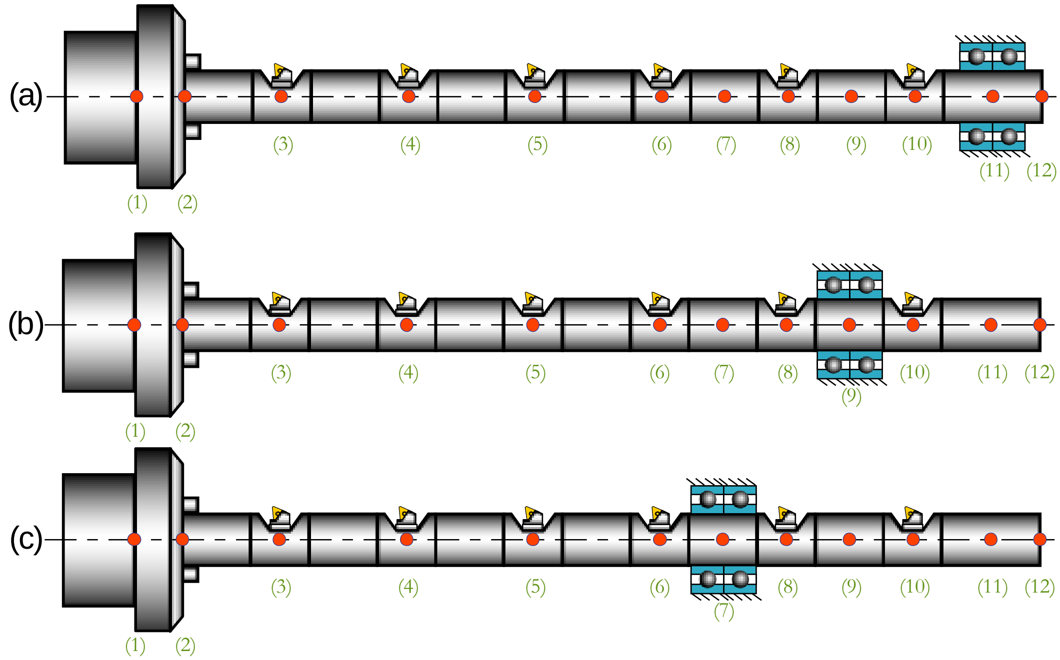

Figure 4-28 : Different support conditions: out-board support is at (a) node 11, (b) node 9, (c) node 7

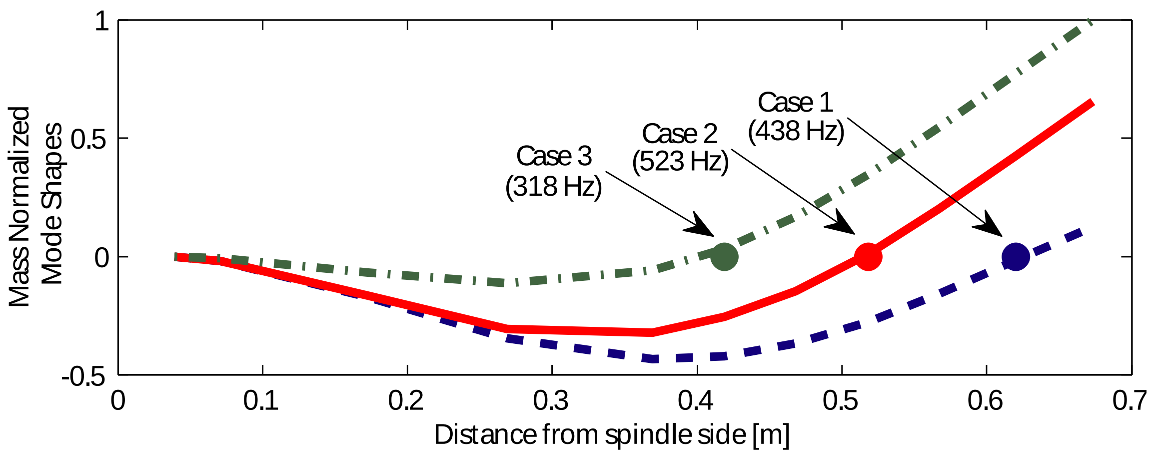

Figure 4-29 : Mass normalized bending mode shapes for 3 different support conditions, see Figure 4-28 for support conditions

The Zero Order Solution and Nyquist Stability Method are used to predict the stability diagram, as shown in Figure 4-30 and Figure 4-31 respectively. Both results suggest that the second bearing location provides higher stable operating conditions. The predicted chatter frequencies confirm that the first bending mode causes regenerative vibrations.

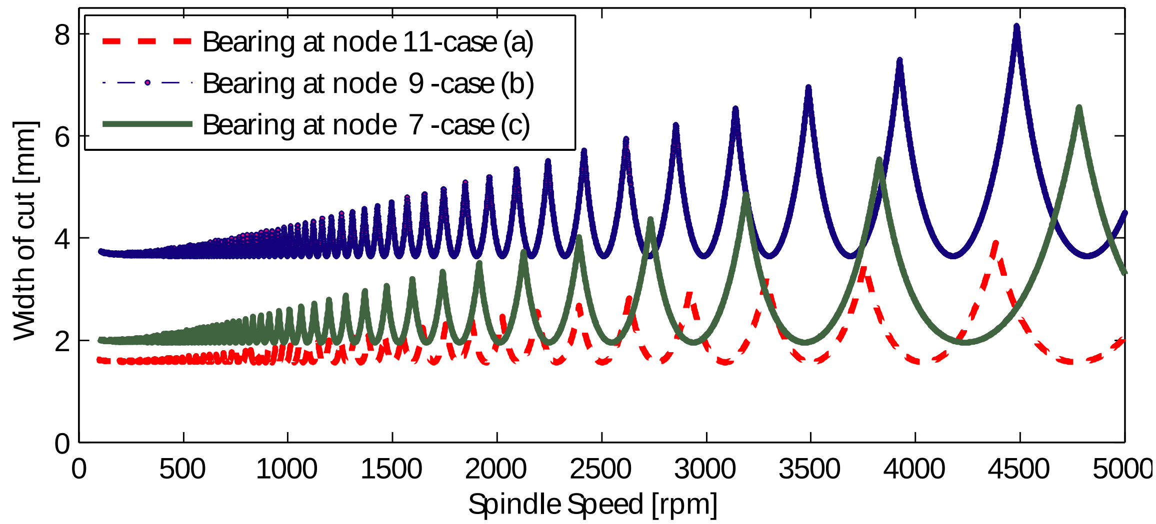

Figure 4-30 : Comparison of support conditions using Zero Order Solution. See Figure 4-28a, b, c for bearing locations.

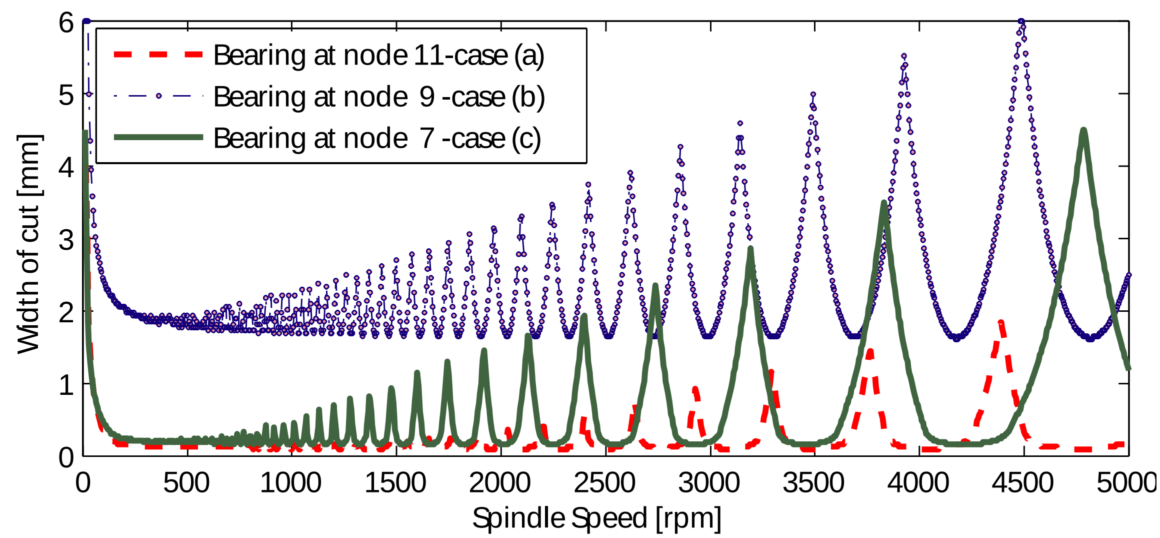

Figure 4-31 : Comparison of support conditions using Nyquist stability criterion. See Figure 4-28a, b, c for bearing locations.

Several observations can be made from the simulation results. The first one is that if there is a slight difference between the NSM and SD at higher stability lobes, the difference becomes larger at low speeds due to the directional coefficients. The second observation is that the SD method always resulted in a higher stability border than the NSM where only average terms are used.

The different angular orientation of the inserts clearly showed that the time varying coefficients have a significant effect on chatter stability limit at low speeds. The cases which ended up giving higher stability border do not necessarily mean that they are always the best insert configurations. It totally depends on the mode shapes of the dominant structural modes. The support conditions change the mode shapes considerably. In simulations, only the cases which have the same number of inserts at each bore location are examined. In those cases, the delay time is same for all cutting locations. Although there is not a line boring tool that has a different number of inserts at each station, i.e. delay time is not the same, the stability of those can still be analyzed by using Nyquist Stability Method by changing the delay for each cutting point.

4.7 Summary

In this chapter, the mechanics and dynamics of the line boring operation are presented. The method uses a similar force model as presented in the previous chapter. However, forces generated at each bore location are taken into account for the dynamic analysis. The transfer function at the cutter locations is estimated using the Finite Element beam theory. The stability of the process is investigated in frequency domain, as well as in time domain. In frequency domain, the Zero Order Method provides a very fast solution, although the directional terms are approximated by their average, and speed dependent process damping forces are neglected. The Nyquist Stability Method predicts stability when the process damping effect is included, but the average directional terms are used. Semi-Discretization investigates the stability in time domain by approximating the delay term at small time intervals. The time varying directional coefficients and process damping are accounted for in this method with an expense of increased computational time. The vibrations and cutting forces are predicted with Semi-Discretization method as well. Different insert, support, and angular orientation cases are compared extensively. The line boring model presented here represents the big picture of all boring types, but this model can be easily adapted to other types.

Chapter 5

Conclusions

The thesis presents an identification technique for the process damping coefficient and a comprehensive dynamic model of the line boring process, including process damping.

The need for stability prediction in machining operation leads to the modeling of the mechanics and dynamics of each process. Although the predictions are quite satisfactory for high speed machining, low speed stability remains difficult to estimate because of the tool flank-workpiece contact mechanism known as process damping. The relationship between the workpiece material and process damping is introduced to the system with a coefficient. Previous research used either a fast oscillator device designed for this purpose which is impractical, or indentation tests under static conditions which do not represent the real dynamic cutting. A simpler identification process is proposed in this thesis. The method is carried out by cutting a long cylindrical workpiece with a regular plunge turning (face turning) setup. Since process damping is dominant at low speeds, the transition from less damped speed to highly damped speed is possible if the vicinity of critical speed is scanned. The plunge turning process has the capability to scan a wide range of surface speed as the diameter of the workpiece is proportional to the surface speed. After the critical surface speed is detected using a microscope and force sensor during chatter tests, the process damping coefficient can be identified from the characteristic equation of the dynamic process around the chatter frequency observed in the tests. In the case of more than one candidate value, the critical stability must be checked using the Nyquist plot of the characteristic equation and then incorrect values can be eliminated. The influence of the process parameters and tool geometry on the chip flow direction is added to the dynamic system by describing an approximate chip model. The stability is solved by using the Nyquist stability criterion including the identified process damping coefficient, and experimental results agree with the predicted stability border at low speeds. Eventually, this model predicts the vertical chatter free speed limit, and in this range, the main limitation for machining hard materials becomes tool wear rather than instability.

The dynamic analysis of the line boring process has never been addressed in the past. The process differs from other boring operations because, unlike others, there are multiple cutters located along the long boring bar where the structural dynamic characteristics can be quite different, and cross talk between each bore location is significant. The transfer function at each bore location was estimated by using the finite element beam theory. The frequency and time domain stability prediction methods are proposed in this thesis. The Zero Order Solution, as one of the frequency domain methods, predicts the critical stability border very quickly, although average directional terms are used and the speed dependent process damping effect is neglected. This fast solution gives insight to the stability border and, because it is fast, different conditions can be compared easily. The Nyquist stability criterion is second frequency domain method where, in addition to the Zero Order Solution, the process damping effect and approximate chip model can be added. Semi Discretization solves the stability in the time domain where, instead of the transfer function, the dynamic parameters are used in the governing differential equation. The semi-discrete solution is able to capture the effect of time varying directional terms unlike the frequency domain methods presented, but it costs increased computational time. Different angular orientation of the inserts clearly showed that the time varying coefficients have a significant effect on chatter stability at low speeds. Besides stability, vibrations and linear dynamic cutting forces can be predicted by using the semi-discrete method as well. The proposed model can be configured to any insert configuration, support location, and different size of the boring bar easily, as it is presented in the results section. This gives the opportunity to investigate the stability of the system at the design stage.

For line boring stability, the chip flow angle is the key parameter because it determines the contribution of flexibilities in different directions on the chip regeneration mechanism. Since the line boring bar is very long, vibrations in the radial direction are severe. As the approach angle increases, so does the chip flow angle, and the influence of radial vibrations decreases. Thus, the approach angle of the insert should be 90° for the minimum radial vibration effect. As the nose radius increases, cutting forces are directed to the radial direction again. Thus, inserts having small nose radius should be selected.

As the number of radially spaced inserts at each bore station increases, the minimum critically stable width of cut value decreases. At this point, the designer has to make a compromise between stability and productivity while deciding the number of inserts. The insert configurations mentioned in the thesis have same number of inserts at each station. The proposed Nyquist Stability Method is able to predict the stability in the case of different number of inserts at each station although there is not any line boring tool with this configuration.

The angular orientation of inserts with respect to each other has a significant effect on stability at low speed. The best orientation should be determined considering the dominant bending modes of the structure which change with the support conditions.

Future work includes chatter tests that must be carried out for verification of the proposed stability methods used in the line boring process. The proposed model is only capable of predicting stability when inserts are evenly distributed around the circumference of the bar, i.e. uniform pitch angle. A further study can be done to solve the stability of non-uniform pitch angle cases. An algorithm to find the optimum bearing locations can be studied to maximize the stable cutting conditions.

Bibliography

[1] S. A. Tobias and W. Fishwick, “Theory of regenerative machine tool chatter,” *The Engineer*, vol. 205, pp. 16–23, 1958.

[2] J. Tlusty and M. Polacek, “The Stability of the Machine Tool Against Self-Excited Vibration in Machining,” *ASME Int. res. in production*, vol. 1, pp. 474, 465, 1963.

[3] H. E. Merritt, “Theory of self-excited machine-tool chatter,” *Journal of Engineering for Industry*, vol. 87, no. 4, pp. 447–454, 1965.

[4] O. B. Ozdoganlar and W. J. Endres, “An analytical representation of chip area for corner-radiused tools under both depth-of-cut and feed variations,” *Journal of Manufacturing Science and Engineering(USA)*, vol. 122, no. 4, pp. 660–665, 2000.

[5] O. B. Ozdoganlar and W. J. Endres, “An Analytical Stability Solution for the Turning Process with Depth-Direction Dynamics and Corner-Radiused Tooling,” in *Symp. on Advances in Modeling, Monitoring, and Control of Machining Systems*, vol. 64, pp. 511–518, 1998.

[6] R. G. Reddy, O. B. Ozdoganlar, S. G. Kapoor, R. E. DeVor, and X. Liu, “A Stability Solution for the Axial Contour-Turning Process,” *Journal of Manufacturing Science and Engineering*, vol. 124, no. 3, pp. 581-587, 2002.

[7] Y. Altintas, *Manufacturing automation : metal cutting mechanics, machine tool vibrations, and CNC design*. New York: Cambridge University Press, 2000.

[8] B. E. Clancy and Y. C. Shin, “A comprehensive chatter prediction model for face turning operation including tool wear effect,” *International Journal of Machine Tools and Manufacture*, vol. 42, no. 9, pp. 1035-1044, Jul. 2002.

[9] E. Ozlu and E. Budak, “Analytical Modeling of Chatter Stability in Turning and Boring Operations Part I: Model Development-Part II: Experimental Verification,” *Trans. ASME Journal of Manufacturing Science and Technology*, 2007.

[10] E. Budak and Y. Altintas, “Analytical Prediction of Chatter Stability in Milling---Part I: General Formulation,” *Journal of Dynamic Systems, Measurement, and Control*, vol. 120, no. 1, pp. 22-30, Mar. 1998.

[11] M. Eynian and Y. Altintas, “Chatter Stability of General Turning Operations With Process Damping,” *Journal of Manufacturing Science and Engineering*, vol. 131, no. 4, pp. 041005-10, 2009.

[12] J. R. Baker and K. E. Rouch, “Stability analysis of boring bars with asymmetry,” *Machining Science and Technology: An International Journal*, vol. 6, no. 1, p. 81, 2002.

[13] E. W. Parker, “Dynamic stability of a cantilever boring bar with machined flats under regenerative cutting conditions,” *Journal of Mechanical Engineering Science 1959-1982 (vols 1-23)*, vol. 12, no. 2, pp. 104–115, 1970.

[14] M. Iyer, “An analytical model for prediction of chatter stability in boring,” Michigan State University, 2000.

[15] F. Atabey, I. Lazoglu, and Y. Altintas, “Mechanics of boring processes--Part I,” *International Journal of Machine Tools and Manufacture*, vol. 43, no. 5, pp. 463-476, Apr. 2003.

[16] I. Lazoglu, F. Atabey, and Y. Altintas, “Dynamics of boring processes: Part III-time domain modeling,” *International Journal of Machine Tools and Manufacture*,

vol. 42, no. 14, pp. 1567-1576, Nov. 2002.

[17] N. Yussefian, B. Moetakef-Imani, and H. El-Mounayri, “The prediction of cutting force for boring process,” *International Journal of Machine Tools and Manufacture*, vol. 48, no. 12, pp. 1387-1394, Oct. 2008.

[18] B. Moetakef-Imani and N. Yussefian, “Dynamic simulation of boring process,” *International Journal of Machine Tools and Manufacture*, vol. 49, no. 14, pp. 1096-1103, Nov. 2009.

[19] K. F. Ehmann, S. G. Kapoor, R. E. DeVor, and I. Lazoglu, “Machining Process Modeling: A Review,” *Journal of Manufacturing Science and Engineering*, vol. 119, no. 4, pp. 655-663, Nov. 1997.

[20] Y. Altintas and M. Weck, “Chatter Stability of Metal Cutting and Grinding,” *CIRP Annals - Manufacturing Technology*, vol. 53, no. 2, pp. 619-642, 2004.

[21] S. Tobias, *Machine-Tool Vibration*, 1st ed. Blackie & Son Ltd., 1965.

[22] D. W. Wu and C. R. Liu, “An analytical model of cutting dynamics. Part 1: Model building.,” *J. ENG. IND.*, vol. 107, no. 2, pp. 107–111, 1985.

[23] D. W. Wu and C. R. Liu, “An analytical model of cutting dynamics. Part 2: Verification.,” *J. ENG. IND.*, vol. 107, no. 2, pp. 112–118, 1985.

[24] D. Wu, “A New Approach of Formulating the Transfer Function of Dynamic Cutting Processes,” *J. Eng. Ind.(Trans. ASME)*, vol. 111, no. 1, pp. 37-47, 1989.

[25] B. Y. Lee, Y. S. Tarng, and S. C. Ma, “Modeling of the process damping force in chatter vibration,” *International Journal of Machine Tools and Manufacture*, vol. 35, no. 7, pp. 951-962, Jul. 1995.

[26] R. Y. Chiou and S. Y. Liang, “Chatter stability of a slender cutting tool in turning with tool wear effect,” *International Journal of Machine Tools and Manufacture*, vol. 38, no. 4, pp. 315-327, Apr. 1998.

[27] Y. Altintas, M. Eynian, and H. Onozuka, “Identification of dynamic cutting force coefficients and chatter stability with process damping,” *CIRP Annals - Manufacturing Technology*, vol. 57, no. 1, pp. 371-374, 2008.

[28] K. Ahmadi and F. Ismail, “Experimental investigation of process damping nonlinearity in machining chatter,” *International Journal of Machine Tools and Manufacture*, 2010.

[29] E. Budak and L. T. Tunc, “A New Method for Identification and Modeling of Process Damping in Machining,” *Journal of Manufacturing Science and Engineering*, vol. 131, no. 5, pp. 051019-10, Oct. 2009.

[30] E. Budak and L. Tunc, “Identification and modeling of process damping in turning and milling using a new approach,” *CIRP Annals - Manufacturing Technology*, vol. 59, no. 1, pp. 403-408, 2010.

[31] F. A. Khasawneh, B. P. Mann, T. Insperger, and G. Stepan, “Increased Stability of Low-Speed Turning Through a Distributed Force and Continuous Delay Model,” *Journal of Computational and Nonlinear Dynamics*, vol. 4, no. 4, pp. 041003-12, Oct. 2009.

[32] D. Bachrathy and G. Stépán, “Time-periodic velocity-dependent process damping in milling processes,” *CIRP PMI 2nd Conference Proceedings, Vancouver*, 2010.

[33] T. Insperger and G. Stépán, “Updated semi-discretization method for periodic delay-differential equations with discrete delay,” *International Journal for Numerical Methods in Engineering*, vol. 61, no. 1, pp. 117-141, 2004.

[34] C. M. Taylor, S. Turner, and N. D. Sims, “Chatter, process damping, and chip segmentation in turning: A signal processing approach,” *Journal of Sound and Vibration*, vol. 329, no. 23, pp. 4922-4935, Nov. 2010.

[35] C. Li, A. G. Ulsoy, and W. J. Endres, “The Effect of Flexible-Tool Rotation on Regenerative Instability in Machining,” *Journal of Manufacturing Science and Engineering*, vol. 125, no. 1, pp. 39-47, Feb. 2003.

[36] F. Atabey, I. Lazoglu, and Y. Altintas, “Mechanics of boring processes--Part II--multi-insert boring heads,” *International Journal of Machine Tools and Manufacture*, vol. 43, no. 5, pp. 477-484, Apr. 2003.

[37] M. Suren, “Dynamic Modeling of Single and Multi Point Turning Operations,” University of British Columbia, 2004.

[38] F. Koenigsberger and J. Tlusty, *Machine Tool Structures*, vol. 1. Pergamon Press, Oxford, 1970.

[39] T. R. Sisson and R. L. Kegg, “An explanation of low speed chatter effects,” *Trans. ASME Journal of Engineering for Industry*, vol. 91, pp. 951–955, 1969.

[40] P. Wallace and C. Andrew, “Machining forces: some effects of tool vibration,” *Journal of mechanical engineering science*, vol. 7, pp. 152-162, 1965.

[41] Sandvik Coromant - Main Catalogue, 2009. [Online]. Available: http://www.sandvik.coromant.com/US. [Accessed: 26-Apr-2010].

[42] G. V. Stabler, “The chip flow law and its consequences,” *Advances in Machine Tool Design and Research*, pp. 243–251, 1964.

[43] L. V. Colwell, “Predicting the angle of chip flow for single point cutting tools,” *Trans. ASME*, vol. 76, no. 2, pp. 199–204, 1954.

[44] H. T. Young, P. Mathew, and P. L. B. Oxley, “Allowing for nose radius effects in predicting the chip flow direction and cutting forces in bar turning,” *Proc. Inst. Mech. Engrs*, vol. 201, pp. 213–226, 1987.

[45] J. Wang, “Development of a chip flow model for turning operations,” *International Journal of Machine Tools and Manufacture*, vol. 41, no. 9, pp. 1265-1274, Jul. 2001.

[46] E. J. A. Armarego and M. Uthaichaya, “A Mechanics of Cutting Approach for Force Prediction in Turning Operations,” *J. of Engineering Production*, vol. 1, pp. 1–18, 1977.

[47] P. Lee and Y. Altintas, “Prediction of ball-end milling forces from orthogonal cutting data,” *International Journal of Machine Tools and Manufacture*, vol. 36, no. 9, pp. 1059-1072, Sep. 1996.

[48] M. Eynian, “Chatter stability of turning and milling with process damping,” University of British Columbia, 2010.

[49] M. Kaymakci, “Generalized modeling of metal cutting mechanics,” University of British Columbia, 2009.

[50] S. A. Tobias, “Machine tool vibration,” *Shock and vibration handbook*, 1961.

[51] Y. Kurata, S. D. Merdol, Y. Altintas, N. Suzuki, and E. Shamoto, “Chatter Stability in Turning and Milling with In Process Identified Process Damping,” *Journal of Advanced Mechanical Design, Systems, and Manufacturing*, In Press. 2010.

[52] N. Olgac and G. Zhao, “A Relative Stability Study on the Dynamics of the Turning Mechanism,” *Journal of Dynamic Systems, Measurement, and Control*, vol. 109, no. 2, pp. 164-170, Jun. 1987.

[53] G. C. Goodwin, S. F. Graebe, and M. E. Salgado, *Control System Design*. Prentice Hall, Upper Saddle, River New Jersey, 2001.
[54] K. Ogata, *Modern Control Engineering Fourth Edition Prentice Hall, Upper Saddle River, NJ*. 2002.
[55] J. S. Przemieniecki, *Theory of matrix structural analysis*. McGraw-Hill, New York, 1968.
[56] T. Yokoyama, "Vibrations of a hanging Timoshenko beam under gravity," *Journal of Sound and Vibration*, vol. 141, no. 2, pp. 245-258, Sep. 1990.
[57] F. Koppka, "A Contribution to the Maximization of Productivity and Workpiece Quality of the Reaming Process by Analyzing its Static and Dynamic Behavior," Technical University of Darmstadt, 2008.
[58] R. D. Cook, D. S. Malkus, and M. E. Plesha, "Concepts and applications of the finite element method," *John Willey and Sons, New York*, 1989.
[59] D. J. Ewins, *Modal testing: theory, practice and application*. Research studies press England, 2000.
[60] J. H. Ko and Y. Altintas, "Dynamics and Stability of Plunge Milling Operations," *Journal of Manufacturing Science and Engineering*, vol. 129, no. 1, pp. 32-40, Feb. 2007.
[61] S. D. Merdol and Y. Altintas, "Multi Frequency Solution of Chatter Stability for Low Immersion Milling," *Journal of Manufacturing Science and Engineering*, vol. 126, no. 3, pp. 459-466, 2004.
[62] L. Meirovitch, *Fundamentals of Vibrations*. International Edition, McGraw-Hill, 2001.
[63] T. Insperger, G. Stépán, and J. Turi, "On the higher-order semi-discretizations for periodic delayed systems," *Journal of Sound and Vibration*, vol. 313, no. 1, pp. 334-341, Jun. 2008.
[64] G. R. Cowper, "The shear coefficient in Timoshenko's beam theory," *Transactions of ASME, Journal of Applied Mechanics*, vol. 33, no. 2, pp. 335–340, 1966.

Appendix A

Timoshenko Beam Element Formulations

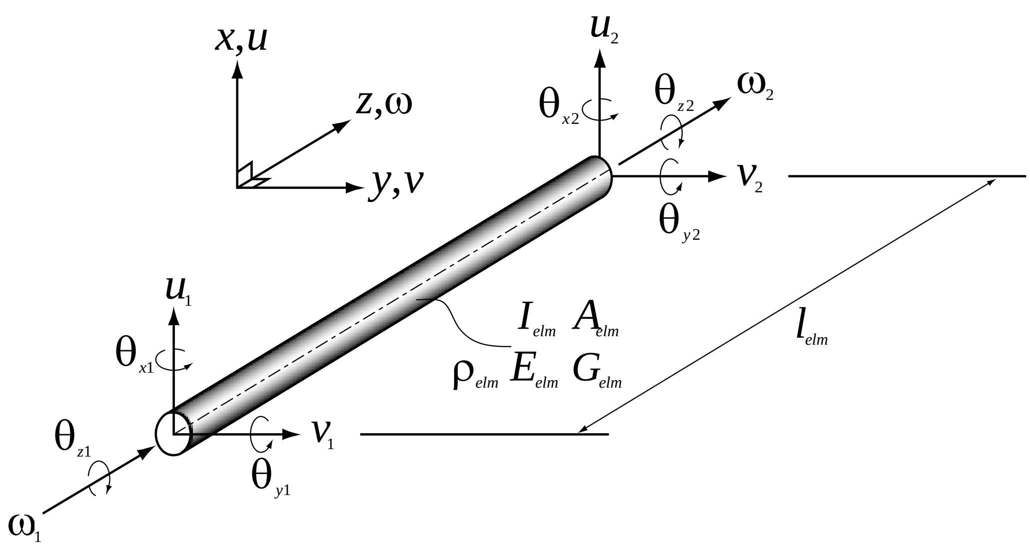

Figure A-1 : Timoshenko Beam Element

Figure A-1 shows a 6 dof/node beam element where geometric and material properties are listed as:

l_{elm} : length of the beam element

A_{elm} : area of the cross section

I_{elm} : second moment of area of element's cross section

ρ_{elm} : density of the material

E_{elm} : Young's modulus

G_{elm} : shear modulus

There are 3 translational degrees of freedom (u, v, ω) and 3 rotational degrees of freedom $(\theta_x, \theta_y, \theta_z)$ at each node. Stiffness ($\mathbf{K}_{elm}$) and mass ($\mathbf{M}_{elm}$) matrices of the Timoshenko beam element are given as [55], [56]:

$$
\mathbf{K}_{elm} = \begin{bmatrix}
k_1^y & & & & & & & & & & & \\
0 & k_1^x & & & & & S & & & & & \\
0 & 0 & k_2 & & & & & & & & & \\
0 & -k_3^x & 0 & k_5^x & & & & & Y & & & \\
k_3^y & 0 & 0 & 0 & k_5^y & & & & & & & \\
0 & 0 & 0 & 0 & 0 & k_4 & & & & M & & \\
-k_1^y & 0 & 0 & 0 & -k_3^y & 0 & k_1^y & & & & & \\
0 & -k_1^x & 0 & k_3^x & 0 & 0 & 0 & k_1^x & & & & \\
0 & 0 & -k_2 & 0 & 0 & 0 & 0 & 0 & k_2 & & & \\
0 & -k_3^x & 0 & k_6^x & 0 & 0 & 0 & k_3^x & 0 & k_5^x & & \\
k_3^y & 0 & 0 & 0 & k_6^y & 0 & -k_3^y & 0 & 0 & 0 & k_5^y & \\
0 & 0 & 0 & 0 & 0 & -k_4 & 0 & 0 & 0 & 0 & 0 & k_4
\end{bmatrix} \tag{A.1}
$$

$$
\mathbf{M}_{elm} = \rho_{elm} A_{elm} l_{elm} \begin{bmatrix}
m_1^y & & & & & & & & & & & \\
0 & m_1^x & & & & & S & & & & & \\
0 & 0 & m_2 & & & & & & & & & \\
0 & -m_3^x & 0 & m_5^x & & & & & Y & & & \\
m_3^y & 0 & 0 & 0 & m_5^y & & & & & & & \\
0 & 0 & 0 & 0 & 0 & m_4 & & & & M & & \\
m_9^y & 0 & 0 & 0 & m_{10}^y & 0 & m_1^y & & & & & \\
0 & m_9^x & 0 & -m_{10}^x & 0 & 0 & 0 & m_1^x & & & & \\
0 & 0 & m_7 & 0 & 0 & 0 & 0 & 0 & m_2 & & & \\
0 & m_{10}^x & 0 & m_6^x & 0 & 0 & 0 & m_3^x & 0 & m_5^x & & \\
-m_{10}^y & 0 & 0 & 0 & m_6^y & 0 & -m_3^y & 0 & 0 & 0 & m_5^y & \\
0 & 0 & 0 & 0 & 0 & m_8 & 0 & 0 & 0 & 0 & 0 & m_4
\end{bmatrix} \tag{A.2}
$$

where elements of stiffness matrix is given by:

$$
\begin{aligned}
k_1^i &= \frac{12E_{elm}I_{elm,ii}}{l_{elm}^3(1+\Phi_j)}, \quad k_2 = \frac{A_{elm}E_{elm}}{l_{elm}}, \qquad k_3^i = \frac{6E_{elm}I_{elm,ii}}{l_{elm}^2(1+\Phi_j)} \\
k_4 &= \frac{I_{elm,zz}G}{l_{elm}}, \qquad k_5^i = \frac{(4+\Phi_j)E_{elm}I_{elm,ii}}{l_{elm}(1+\Phi_j)}, k_6^i = \frac{(2-\Phi_j)E_{elm}I_{elm,ii}}{l_{elm}(1+\Phi_j)}
\end{aligned} \tag{A.3}
$$

where elements of mass matrix is given by:

$$
\begin{aligned}
m_1^i &= \frac{\frac{13}{35}+\frac{7}{10}\Phi_j+\frac{1}{3}\Phi_j^2+\frac{6}{5}\left(r_{elm,i}^G / l_{elm}\right)^2}{(1+\Phi_j)^2}, \quad m_2=\frac{1}{3}, \quad m_4=\frac{I_{elm,zz}}{3A_{elm}} \\
m_3^i &= \frac{\left(\frac{11}{210}+\frac{11}{120}\Phi_j+\frac{1}{24}\Phi_j^2+\left(\frac{1}{10}-\frac{1}{2}\Phi_j\right)\left(r_{elm,i}^G / l_{elm}\right)^2\right)l_{elm}}{(1+\Phi_j)^2} \\
m_5^i &= \frac{\left(\frac{1}{105}+\frac{1}{60}\Phi_j+\frac{1}{120}\Phi_j^2+\left(\frac{2}{15}+\frac{1}{6}\Phi_j+\frac{1}{3}\Phi_j^2\right)\left(r_{elm,i}^G / l_{elm}\right)^2\right)l_{elm}^2}{(1+\Phi_j)^2} \\
m_6^i &= \frac{\left(-\left(\frac{1}{140}+\frac{1}{60}\Phi_j+\frac{1}{120}\Phi_j^2\right)+\left(-\frac{1}{30}-\frac{1}{6}\Phi_j+\frac{1}{6}\Phi_j^2\right)\left(r_{elm,i}^G / l_{elm}\right)^2\right)l_{elm}^2}{(1+\Phi_j)^2} \\
m_7 &= \frac{1}{6}, \quad m_8=\frac{I_{elm,zz}}{6A_{elm}}, \qquad m_9^i=\frac{\frac{9}{70}+\frac{3}{10}\Phi_j+\frac{1}{6}\Phi_j^2-\frac{6}{5}\left(r_{elm,i}^G / l_{elm}\right)^2}{(1+\Phi_j)^2} \\
m_{10}^i &= \frac{\left(\frac{13}{420}+\frac{3}{40}\Phi_j+\frac{1}{24}\Phi_j^2-\left(\frac{1}{10}-\frac{1}{2}\Phi_j\right)\left(r_{elm,i}^G / l_{elm}\right)^2\right)l_{elm}}{(1+\Phi_j)^2}
\end{aligned}
\tag{A.4}
$$

The subscripts i and j denote x or y axis. If one indicates x, the other indicates y, and vice versa. Radius of gyration is calculated by $r_{elm,i}^G=\sqrt{I_{elm,ii} / A_{elm}}$ where $I_{elm,ii}$ is the second moment of area of the cross section. Φ_j is the shear deformation parameter given as:

$$
\Phi_j=\frac{12E_{elm}I_{elm,ii}}{k_i^s G_{elm}A_{elm}l_{elm}^2}
\tag{A.4}
$$

where k_i^s is the cross section factor [64]:

$$
k_i^s=\begin{cases} 0.9 & \text{if circular cross section} \\ \dfrac{6(1+v)(1+\beta^2)^2}{(7+6v)(1+\beta^2)^2+(20+12v)\beta^2} & \text{if hollow circular cross section} \end{cases}
\tag{A.5}
$$

β is the ratio of the inner diameter to the outer diameter and v is the Poisson's ratio.

Appendix B

Solution of ODE at each Semi-Discretization Interval

In this section, the exact solution of the inhomogeneous ordinary differential equation (ODE) with constant coefficients is presented (see Eq.(4.66)). Matrices ($\mathbf{L}_i, \mathbf{R}_i, \mathbf{S}_i$) in ODE are constant only in the time interval where they are defined. The solution is carried out by using the method of variations of parameters.

$$\dot{\mathbf{r}}(t) = \mathbf{L}_i \cdot \mathbf{r}(t) + \underbrace{\mathbf{R}_i \cdot \left(\frac{\mathbf{r}_{i-k} + \mathbf{r}_{i-k+1}}{2} \right) + \mathbf{S}_i}_{\tilde{R}_i \tilde{S}_i} \quad \text{(A)}$$

$$\text{if} \quad t \in [t_i, t_{i+1}] \quad \text{(B)}$$

$$\dot{\mathbf{r}}(t) = \mathbf{L}_i \cdot \mathbf{r}(t) + \tilde{R}_i \tilde{S}_i \tag{B.1}$$

The general solution of the above differential equation consists of homogeneous ($\mathbf{r}_h(t)$) and particular ($\mathbf{r}_p(t)$) solutions. For the homogeneous part, the ODE is reduced to below form and solution $\mathbf{r}_h(t)$ is given as:

$$\dot{\mathbf{r}}_h(t) = \mathbf{L}_i \cdot \mathbf{r}_h(t) \quad \rightarrow \quad \mathbf{r}_h(t) = e^{\mathbf{L}_i (t-t_i)} \cdot \mathbf{C}_0 \tag{B.2}$$

where $\mathbf{C}_0$ is a constant vector which is found after application of the initial conditions to the general solution. The inhomogeneous ODE and particular solution are given by:

$$\dot{\mathbf{r}}_p(t) = \mathbf{L}_i \cdot \mathbf{r}_p(t) + \tilde{R}_i \tilde{S}_i \tag{B.3}$$

$$\mathbf{r}_p(t) = e^{\mathbf{L}_i (t-t_i)} \cdot \mathbf{u}(t) \tag{B.4}$$

Substituting (B.4) into (B.3) yields to:

$$\begin{gathered} e^{\mathbf{L}_i (t-t_i)} \cdot \dot{\mathbf{u}}(t) + \mathbf{L}_i e^{\mathbf{L}_i (t-t_i)} \cdot \mathbf{u}(t) = \mathbf{L}_i e^{\mathbf{L}_i (t-t_i)} \cdot \mathbf{u}(t) + \tilde{R}_i \tilde{S}_i \\ \dot{\mathbf{u}}(t) = e^{-\mathbf{L}_i (t-t_i)} \cdot \tilde{R}_i \tilde{S}_i \end{gathered} \tag{B.5}$$

Integrating both sides of (B.5) results in:

$$\begin{gathered} \int_{t_i}^{t} d\mathbf{u}(t) = \int_{t_i}^{t} e^{-\mathbf{L}_i (t-t_i)} \cdot \tilde{R}_i \tilde{S}_i \, dt \qquad \text{at} \quad t_i < t < t_{i+1} \\ \mathbf{u}(t) = -\mathbf{L}_i^{-1} \cdot e^{-\mathbf{L}_i (t-t_i)} \cdot \tilde{R}_i \tilde{S}_i + \mathbf{L}_i^{-1} \cdot \tilde{R}_i \tilde{S}_i + \mathbf{u}(t_i) \end{gathered} \tag{B.6}$$

Thus, the particular solution (B.4) becomes as:

$$\begin{aligned}\mathbf{r}_p(t) &= e^{\mathbf{L}_i(t-t_i)}\cdot(-\mathbf{L}_i^{-1}\cdot e^{-\mathbf{L}_i(t-t_i)}\cdot\tilde{R}_i\tilde{S}_i + \underbrace{\mathbf{L}_i^{-1}\cdot\tilde{R}_i\tilde{S}_i + \mathbf{u}(t_i)}_{\tilde{D}_i}) \\ &= -e^{\mathbf{L}_i(t-t_i)}\cdot\mathbf{L}_i^{-1}\cdot e^{-\mathbf{L}_i(t-t_i)}\cdot\tilde{R}_i\tilde{S}_i + e^{\mathbf{L}_i(t-t_i)}\cdot\tilde{D}_i\end{aligned} \tag{B.7}$$

Pre-multiplying by $\mathbf{L}_i$ and using the exponential matrix property of $e^{YXY^{-1}} = Ye^XY^{-1}$:

$$\begin{aligned}\mathbf{L}_i\cdot\mathbf{r}_p(t) &= -\underbrace{\mathbf{L}_i\cdot e^{\mathbf{L}_i(t-t_i)}\cdot\mathbf{L}_i^{-1}}_{e^{\mathbf{L}_i\mathbf{L}_i\mathbf{L}_i^{-1}(t-t_i)}=e^{\mathbf{L}_i(t-t_i)}}\cdot e^{-\mathbf{L}_i(t-t_i)}\cdot\tilde{R}_i\tilde{S}_i + \mathbf{L}_i\cdot e^{\mathbf{L}_i(t-t_i)}\cdot\tilde{D}_i \\ &= -\underbrace{e^{\mathbf{L}_i(t-t_i)}\cdot e^{-\mathbf{L}_i(t-t_i)}}_{\mathbf{I}}\cdot\tilde{R}_i\tilde{S}_i + \mathbf{L}_i\cdot e^{\mathbf{L}_i(t-t_i)}\cdot\tilde{D}_i\end{aligned} \tag{B.8}$$

Thus, the particular solution is found as:

$$\mathbf{r}_p(t) = -\mathbf{L}_i^{-1}\cdot\tilde{R}_i\tilde{S}_i + e^{\mathbf{L}_i(t-t_i)}\cdot\left(\mathbf{L}_i^{-1}\cdot\tilde{R}_i\tilde{S}_i + \mathbf{u}(t_i)\right) \tag{B.9}$$

The general solution is obtained by adding the homogeneous and particular solutions:

$$\mathbf{r}(t) = e^{\mathbf{L}_i(t-t_i)}\cdot\mathbf{C}_0 - \mathbf{L}_i^{-1}\cdot\tilde{R}_i\tilde{S}_i + e^{\mathbf{L}_i(t-t_i)}\cdot\left(\mathbf{L}_i^{-1}\cdot\tilde{R}_i\tilde{S}_i + \mathbf{u}(t_i)\right) \tag{B.10}$$

Since ODE is valid at the defined time interval $t\in[t_i, t_{i+1}]$, an initial condition of $\mathbf{r}(t_i) = \mathbf{r}_i$ at $t = t_i$ is applied to the general solution to obtain unknown $\mathbf{C}_0$ vector.

$$\begin{aligned}\mathbf{r}_i &= \mathbf{I}\cdot\mathbf{C}_0 - \mathbf{L}_i^{-1}\cdot\tilde{R}_i\tilde{S}_i + \mathbf{I}\cdot\left(\mathbf{L}_i^{-1}\cdot\tilde{R}_i\tilde{S}_i + \mathbf{u}(t_i)\right) \\ \mathbf{C}_0 &= \mathbf{r}_i - \mathbf{u}(t_i)\end{aligned} \tag{B.11}$$

Substituting found $\mathbf{C}_0$ into (B.10) leads to the general solution as:

$$\begin{aligned}\mathbf{r}(t) &= e^{\mathbf{L}_i(t-t_i)}\cdot(\mathbf{r}_i - \mathbf{u}(t_i)) - \mathbf{L}_i^{-1}\cdot\tilde{R}_i\tilde{S}_i + e^{\mathbf{L}_i(t-t_i)}\cdot\left(\mathbf{L}_i^{-1}\cdot\tilde{R}_i\tilde{S}_i + \mathbf{u}(t_i)\right) \\ &= e^{\mathbf{L}_i(t-t_i)}\cdot\mathbf{r}_i + \left(e^{\mathbf{L}_i(t-t_i)} - \mathbf{I}\right)\cdot\mathbf{L}_i^{-1}\cdot\tilde{R}_i\tilde{S}_i \qquad \textit{where} \quad t\in[t_i, t_{i+1}]\end{aligned} \tag{B.12}$$

Since the Semi Discretization Method requires solution at $t = t_{i+1}$, a recursive equation is derived which allows one to calculate the next state vector ($\mathbf{r}_{i+1}$) in terms of the current state ($\mathbf{r}_i$) and one period (τ) earlier states ($\mathbf{r}_{i-k}$, $\mathbf{r}_{i-k+1}$) of the dynamic system.

$$\mathbf{r}_{i+1} = \mathbf{r}(t_{i+1}) = \mathbf{N}_{i,1}\cdot\mathbf{r}_i + \mathbf{N}_{i,2}\cdot\left(\mathbf{r}_{i-k} + \mathbf{r}_{i-k+1}\right) + \mathbf{N}_{i,3} \tag{B.13}$$

where time step is $\Delta t = t_{i+1} - t_i$ and coefficient matrices are

$$
\begin{aligned}
\mathbf{N}_{i,1} &= e^{\mathbf{L}_i \Delta t} \\
\mathbf{N}_{i,2} &= \frac{1}{2}\left(e^{\mathbf{L}_i \Delta t} - \mathbf{I}\right) \cdot \mathbf{L}_i^{-1} \cdot \mathbf{R}_i \\
\mathbf{N}_{i,3} &= \frac{1}{2}\left(e^{\mathbf{L}_i \Delta t} - \mathbf{I}\right) \cdot \mathbf{L}_i^{-1} \cdot \mathbf{S}_i
\end{aligned} \tag{B.14}
$$

Appendix C

Analytical Proof of Time-Invariant Directional Factors (if N>2)

The directional coefficient matrix ($\mathbf{A}_i(\phi)$) given in Eq.(4.18) includes time varying terms, i.e. the transformation matrix $\mathbf{T_2}$ and its transpose $\mathbf{T_2^T}$. However, when number of inserts at each station is greater 2 (i.e. N>2), the summation of each term ends up time-invariant terms. Here, the summations are evaluated analytically. By showing the constant terms under one matrix $\mathbf{B}$, Eq.(4.18) is rewritten as:

$$\mathbf{A}_i(\phi) = \sum_{\mathbf{j}=1}^{N}\left(\mathbf{T_2}\cdot\mathbf{T_1}\cdot\boldsymbol{K_c}\cdot\frac{1}{\sin(\kappa_r)}\cdot\mathbf{T_3}\cdot\mathbf{T_2^T}\right) \tag{C}$$

$$\mathbf{A}_i(\phi) = \sum_{\mathbf{j}=1}^{N}\left(\mathbf{T_2}\cdot\mathbf{B}\cdot\mathbf{T_2^T}\right) \tag{C.1}$$

where

$$\mathbf{B} = \mathbf{T_1}\cdot\boldsymbol{K_c}\cdot\frac{1}{\sin(\kappa_r)}\cdot\mathbf{T_3} = \begin{bmatrix} b_{11} & b_{12} & b_{13} & b_{14} \\ b_{21} & b_{22} & b_{23} & b_{24} \\ b_{31} & b_{32} & b_{33} & b_{34} \\ b_{41} & b_{42} & b_{43} & b_{44} \end{bmatrix} \tag{C.2}$$

and all of the terms in $\mathbf{B}$ matrix are time invariant. By substituting the $\mathbf{T_2}$ matrix from Eq.(4.8), the periodic terms of $\mathbf{A}_i(\phi)$ can be shown in a general format as:

$$\mathbf{A}_i(\phi) = \begin{bmatrix} a_{xx} & a_{xy} & a_{xz} & a_{x\phi} \\ a_{yx} & a_{yy} & a_{yz} & a_{y\phi} \\ a_{zx} & a_{zy} & a_{zz} & a_{z\phi} \\ a_{\phi x} & a_{\phi y} & a_{\phi z} & a_{\phi\phi} \end{bmatrix} \quad \textit{and}$$

$$a_{mn} = c_1 + c_2\cdot\sum_{\mathbf{j}=1}^{N}\sin\left(\phi_{\mathbf{j}}\right) + c_3\cdot\sum_{\mathbf{j}=1}^{N}\cos\left(\phi_{\mathbf{j}}\right) + c_4\cdot\sum_{\mathbf{j}=1}^{N}\sin\left(2\phi_{\mathbf{j}}\right) + c_5\cdot\sum_{\mathbf{j}=1}^{N}\cos\left(2\phi_{\mathbf{j}}\right) \tag{C.3}$$

where c_1, c_2, c_3, c_4, c_5 are time-invariant constants, $\phi_{\mathbf{j}}$ is the angular position of insert $\mathbf{j}$, and it is expressed in terms of the angular position of the first insert as:

$$\phi_{\mathbf{j}} = \phi + (\mathbf{j}-1)\cdot\frac{2\pi}{N} \quad where \quad j = 1, 2 \ldots N \tag{C.4}$$

From this point, the time dependent terms in Eq.(C.3) are evaluated separately. Below elementary trigonometric formulae, summation property, and Euler's equation are used for the derivation.

$$\begin{aligned}
&\sin(\alpha \pm \beta) = \sin\alpha\cdot\cos\beta \pm \cos\alpha\cdot\sin\beta \\
&\cos(\alpha \pm \beta) = \cos\alpha\cdot\cos\beta \mp \sin\alpha\cdot\sin\beta \\
&\sum_{n=0}^{N-1} r^n = \frac{r^N - 1}{r-1} \qquad if \quad r \neq 1 \\
&e^{i\theta} = \cos(\theta) + i\sin(\theta)
\end{aligned} \tag{C.5}$$

Summation of $\sin\left(\phi_{\mathbf{j}}\right)$ **terms:**

$$\begin{aligned}
\sum_{\mathbf{j}=1}^{N}\sin(\phi_{\mathbf{j}}) &= \sum_{\mathbf{j}=1}^{N}\sin(\phi + (\mathbf{j}-1)\frac{2\pi}{N}) \\
&= \sum_{\mathbf{j}=1}^{N}\sin(\phi)\cdot\cos\left((\mathbf{j}-1)\frac{2\pi}{N}\right) + \cos(\phi)\cdot\sin\left((\mathbf{j}-1)\frac{2\pi}{N}\right) \\
&= \sin(\phi)\cdot\underbrace{\left(\sum_{\mathbf{j}=1}^{N}\cos\left((\mathbf{j}-1)\frac{2\pi}{N}\right)\right)}_{C} + \cos(\phi)\cdot\underbrace{\left(\sum_{\mathbf{j}=1}^{N}\sin\left((\mathbf{j}-1)\frac{2\pi}{N}\right)\right)}_{D}
\end{aligned} \tag{C.6}$$

In Eq.(C.6), C and D terms can be written using the exponential function as:

$$\begin{aligned}
C &= \sum_{\mathbf{j}=1}^{N}\cos\left((\mathbf{j}-1)\frac{2\pi}{N}\right) \\
&= \mathrm{Re}\left(\sum_{n=0}^{N-1} e^{\left(i.n\frac{2\pi}{N}\right)}\right) = \mathrm{Re}\left(\frac{e^{(i\frac{2\pi}{N})N} - 1}{e^{(i\frac{2\pi}{N})} - 1}\right) \qquad if \quad N \neq 1 \\
&= \mathrm{Re}\left(\frac{e^{i\pi}}{e^{i\pi/N}}\cdot\frac{(e^{i\pi} - e^{-i\pi})}{(e^{i\pi/N} - e^{-i\pi/N})}\right) \\
&= \mathrm{Re}\left(\frac{\cos\pi + i\sin\pi}{\cos(\pi/N) + i\sin(\pi/N)}\cdot\frac{\sin\pi}{\sin(\pi/N)}\right) = 0 \\
&= \begin{cases} 1 & if \quad N = 1 \\ 0 & if \quad N \neq 1 \end{cases}
\end{aligned} \tag{C.7}$$

For calculation of D term in Eq.(C.6), the imaginary component of exponential function can be used, as shown in Eq.(C.7). Result is the same as C term. Thus, summation of $\sin\left(\phi_{\mathrm{j}}\right)$ becomes:

$$\sum_{\mathbf{j}=1}^{N}\sin(\phi_{\mathrm{j}}) = \begin{cases} \sin(\phi) & if \quad N=1 \\ 0 & if \quad N>1 \end{cases} \tag{C.8}$$

Similar derivation can be done for summation of $\cos\left(\phi_{\mathrm{j}}\right)$ in Eq.(C.3) and result is:

$$\sum_{\mathbf{j}=1}^{N}\cos(\phi_{\mathrm{j}}) = \begin{cases} \cos(\phi) & if \quad N=1 \\ 0 & if \quad N>1 \end{cases} \tag{C.9}$$

There are other time dependent terms in Eq.(C.3), such as the summation of $\sin\left(2\phi_{\mathrm{j}}\right)$ and the summation of $\cos\left(2\phi_{\mathrm{j}}\right)$. Only the former is shown below but similar procedure can be applied to the latter as well.

Summation of $\sin\left(2\phi_{\mathrm{j}}\right)$ terms:

$$\begin{aligned} \sum_{\mathbf{j}=1}^{N}\sin(2\phi_{\mathrm{j}}) &= \sum_{\mathbf{j}=1}^{N}\sin(2\phi + 2(\mathbf{j}-1)\frac{2\pi}{N}) \\ &= \sum_{\mathbf{j}=1}^{N}\sin(2\phi)\cdot\cos\left(2(\mathbf{j}-1)\frac{2\pi}{N}\right) + \cos(2\phi)\cdot\sin\left(2(\mathbf{j}-1)\frac{2\pi}{N}\right) \\ &= \sin(2\phi)\cdot\underbrace{\left(\sum_{\mathbf{j}=1}^{N}\cos\left(2(\mathbf{j}-1)\frac{2\pi}{N}\right)\right)}_{C} + \cos(\phi)\cdot\underbrace{\left(\sum_{\mathbf{j}=1}^{N}\sin\left(2(\mathbf{j}-1)\frac{2\pi}{N}\right)\right)}_{D} \end{aligned} \tag{C.10}$$

In Eq.(C.10), C and D terms can be written using the exponential function as:

$$
\begin{aligned}
C &= \sum_{\mathbf{j}=1}^{N} \cos\left(2(\mathbf{j}-1)\frac{2\pi}{N} \right) \\
&= \mathrm{Re}\left(\sum_{n=0}^{N-1} e^{\left(i.2n\frac{2\pi}{N}\right)} \right) = \mathrm{Re}\left(\frac{e^{(i2\frac{2\pi}{N})N} - 1}{e^{(i2\frac{2\pi}{N})} - 1} \right) \quad if \quad N \neq 1, N \neq 2 \\
&= \mathrm{Re}\left(\frac{e^{i2\pi}}{e^{i2\pi/N}} \cdot \frac{(e^{i2\pi} - e^{-i2\pi})}{(e^{i2\pi/N} - e^{-i2\pi/N})} \right) \\
&= \mathrm{Re}\left(\frac{\cos 2\pi + i \sin 2\pi}{\cos(2\pi/N) + i\sin(2\pi/N)} \cdot \frac{\sin 2\pi}{\sin(2\pi/N)} \right) = 0 \\
&= \begin{cases} 1 & if \quad N = 1 \\ 2 & if \quad N = 2 \\ 0 & if \quad N > 2 \end{cases}
\end{aligned}
\tag{C.11}
$$

For calculation of D term in Eq.(C.10), the imaginary component of exponential function can be used, as shown in Eq.(C.11). Result is the same as C term. Thus, summation of $\sin\left(2\phi_{\mathbf{j}}\right)$ becomes:

$$
\sum_{\mathbf{j}=1}^{N} \sin(2\phi_{\mathbf{j}}) = \begin{cases} \sin(2\phi) & if \quad N = 1 \\ 2\sin(2\phi) & if \quad N = 2 \\ 0 & if \quad N > 2 \end{cases}
\tag{C.12}
$$

With the same approach, summation of $\cos\left(2\phi_{\mathbf{j}}\right)$ can be evaluated as:

$$
\sum_{\mathbf{j}=1}^{N} \cos(2\phi_{\mathbf{j}}) = \begin{cases} \cos(2\phi) & if \quad N = 1 \\ 2\cos(2\phi) & if \quad N = 2 \\ 0 & if \quad N > 2 \end{cases}
\tag{C.13}
$$

As a result, elements of directional coefficient matrix $\mathbf{A}_i(\phi)$ are time invariant when the number of inserts is greater than two.